2013

# Direct Numerical Simulations and Analytical Modeling of Granular Filtration

Ravi Kolakaluri
*Iowa State University*

## Recommended Citation

Kolakaluri, Ravi, "Direct Numerical Simulations and Analytical Modeling of Granular Filtration" (2013). *Graduate Theses and Dissertations*. 13621.
http://lib.dr.iastate.edu/etd/13621

# Direct numerical simulations and analytical modeling of granular filtration

by

Ravi Kolakaluri

A dissertation submitted to the graduate faculty
in partial fulfillment of the requirements for the degree of
DOCTOR OF PHILOSOPHY

Major: Mechanical Engineering

Program of Study Committee:

Shankar Subramaniam, Major Professor
Rodney O. Fox
Robert C. Brown
Terry Meyer
Alberto Passalacqua

Iowa State University
Ames, Iowa
2013

# TABLE OF CONTENTS

# LIST OF TABLES

# LIST OF FIGURES

# ACKNOWLEDGEMENTS

I thank God for providing this opportunity of pursuing PhD at Iowa State University and helping me all through these years to finish my PhD.

I would like to take this opportunity to express my sincere thanks and deep appreciations to those who helped me with various aspects of conducting research and the writing of this thesis. First and foremost, I would like to thank Dr. Shankar Subramaniam for his constant guidance, encouragement, patience and support throughout this research and the writing of this thesis. His towering presence instilled in me the carving to work harder and complete the task timely with sufficient degree of independent study. In addition, he is always accessible and willing to help his students. I feel fortunate enough to be a graduate student in his laboratory.

I would also like to thank my POS committee members for all the constructive comments given during my preliminary and final oral exam.

My special thanks to all my fellow lab mates for their kind support, they made my life comfortable and enjoyable. Thank you for your friendship and essential support.

Finally, I would like to extend love and thanks to my mom for her patience and enduring support during my graduate studies at ISU.

# ABSTRACT

Granular filters are traditionally used for water filtration and recently they are being extensively used in several chemical engineering applications. Computational fluid dynamics (CFD) simulations are a cost-effective tool for the design and development of granular filters in applications such as fast pyrolysis of biomass for bio-oil production. The predictive capability of CFD simulations of granular filtration strongly depends on the equations governing the concentration of particulates and the model for the filtration rate. The primary objective of this work is to understand and investigate the filtration of inertial particulates in a granular filter, and develop high fidelity models using direct numerical simulations. Particle–resolved direct numerical simulation (PR-DNS) is a first-principles approach to develop accurate models for interphase momentum, energy, heat transfer in gas-solid flow and can be developed to study granular filtration. Another objective is to test these developed models in the CFD code ANSYS-FLUENT to simulate a full-scale moving bed granular filter.

A direct numerical simulation–Lagrangian particle tracking (DNS–LPT) approach has been developed to simulate moving-bed granular filtration. It is established that DNS–LPT simulations give numerically converged results. The penetration and single–collector efficiency obtained from DNS–LPT gives good match with published results. The DNS–LPT results show that for inertial particles in a granular filter there is a significant nonzero mean slip between particles and fluid. A modified effective Stokes number that gives a good collapse of single-collector efficiency is obtained from DNS–LPT data. Using DNS–LPT simulations we developed a model for filter coefficient in terms of the modified effective Stokes number that can be used in CFD simulations. An analytical framework for calculating filter efficiency of polydisperse particles in a granular bed is developed for cases where inertial impaction and interception are the principal filtration mechanisms. The developed framework can be used for both the Stokes flow and moderate Reynolds number. The results obtained from the analytical framework give a good match with the DNS–LPT results.

The DNS–LPT approach has been used to study bouncing of particles from granule surface by implementing hard-sphere collision between particles and granules. The DNS–LPT results of filter efficiency is compared with the results obtained using laser-based experiments performed by collaborators. The DNS–LPT simulations for bouncing particles are used to develop a model for adhesion probability of inertial particles in a granular filter. In addition to the model development, the developed models are implemented and tested in the CFD code ANSYS-FLUENT to simulate a full-scale moving-bed granular filter.

# CHAPTER 1. Introduction

## 1.1 Background

The term 'filtration' refers to the process of separating solid particles in suspension from a carrier fluid by passing the fluid through a filtering medium which retains part or all of the injected particles. One of the most popular filtration process is granular filtration, a separation process whereby micron and sub-micron sized particles are removed from fluid streams by the presence of fixed (D'Ottavio and Goren, 1983) or moving (El-Hedok et al., 2011) granular beds. In fixed beds, fine particles accumulate on the granules and this affects the filtration efficiency. Eventually the filtration efficiency becomes so low that the process has to be shutdown and the granular bed replenished in order to restore efficient filtration. The advantage of moving granular beds is that the operation can be carried out continuously. Both liquid and gas streams can be treated using granular filtration. Granular filtration finds applications in bio-oil production, which requires filtration of fly ash from hot gases that are generated by fast pyrolysis of biomass (El-Hedok et al., 2011; Ritzert et al., 2004). This is because the stability of bio-oils is adversely affected by the presence of particulates that are formed as a consequence of thermal pyrolysis, so removal of particulates is very important for bio-oil production. It is also used in water and waste-water treatment (Davis, 2010; O'Melia, 1985). It is especially useful in filtration of hot and corrosive exhaust gases in thermal power plants, where other filters cannot be used.

The success of the above mentioned applications depend on the ability of the designer to choose from a wide range of design options and operating parameters such as, granule size, flow rate of moving granules, and pressure drop across the bed. For this purpose high fidelity computational fluid dynamics (CFD) simulations can be very useful. Improving CFD simulations of fixed and moving bed granular filters (MBGF) is useful for improving the design of MBGF for bio-oil production. However, these CFD calculations cannot resolve the flow past individual granules and they represent the filtration rate of particles approximately using models. Existing models for particle filtration rate are obtained from flow models that are formulated on the assumption that a simple geometry (isolated sphere, sphere-in-cell, capillary) can be used to represent randomly packed granular media. These simple geometric models at best only approximate actual granular bed. The flow fields through these simple models are obtained by neglecting the convective term in Navier-Stokes equations which are valid for Stokes flow.

The current work is focused on developing a direct numerical simulation–Lagrangian particle tracking (DNS–LPT) approach that accurately represent, the flow field in a granular bed and tracks particles through the flow field. The DNS–LPT approach developed here can be used for both low and moderate Reynolds number. We use DNS–LPT data to develop improved models for granular filtration that can be used in CFD simulations of MBGF.

## 1.2 Basics of granular filtration

The basic principle of granular filtration is to pass the fluid-particle suspension through a medium composed of granular substances called a granular bed. As the suspension flows through the granular bed, particles get deposited on the surface of the granules. The deposition of suspended particles on the granule consists of two steps: transport and attachment or bouncing. In the first step, particles present in the suspension move towards the vicinity of granules and the rate of particle transport is determined primarily by inertial impaction, interception, gravitation and Brownian diffusion (Tien and Ramarao, 2007). In the attachment or bouncing step the particle can either stick or bounce from the surface of the granules depending on the size, shape and material properties of the particles and granules. Diffusional and gravitational effects in granular beds are significant only for very small particles ($d_p$ <1.0 $\mu$m) at low velocities (Gutfinger and Tardos, 1979). The particles found in applications considered in this study fall in the category of inertial impaction and interception and the fluid streams are at low and moderate Reynolds numbers (10 to 100).

Inertial impaction and interception are significant granular filtration mechanisms for particles with diameters greater than 1 $\mu$m. Granular filtration in the inertial impaction and interception regimes is a strong function of particle inertia that is characterized by the Stokes number $St = \langle W \rangle d_p^2 \rho_p / 18 D_g \mu$ (D'Ottavio and Goren, 1983; Tien and Ramarao, 2007; Araújo et al., 2006). The Stokes number is the ratio of the particle momentum response time to a characteristic fluid time scale. For filtration in a homogeneous granular bed with a constant slip velocity between fluid and granules $\langle W \rangle$, the characteristic fluid time scale is taken to be $D_g / \langle W \rangle$, where $D_g$ is the granule diameter. Note that it is the mean slip velocity between fluid and *granules* (not particles) that determines the scale of fluid motions. The particle momentum response time is $\tau_p = d_p^2 \rho_p / 18\mu$, where $d_p$ is the diameter of the particle, $\rho_p$ is the density of the particle, and $\mu$ is the dynamic viscosity of the fluid. For the case of Stokes or low Reynolds number flow granular filtration is a function of Stokes number $St$ and granule volume fraction $\epsilon_s$. For moderate Reynolds number $Re_m = (1 - \epsilon_s) \langle W \rangle D_g \rho_f / \mu$, granular filtration is a function of Stokes number, granule volume fraction and Reynolds number, where $\rho_f$ is the fluid density. This additional dependence on Reynolds number at moderate Reynolds number is because the fluid time scale in Stokes number is defined based on the mean slip velocity between fluid and granules. The change in flow patterns with Reynolds number also effects the filtration of particles in a granular bed.

## 1.3 Modeling approaches

Filtration theories that describe the capture of particles in a granular bed can be classified into two types: macroscopic and microscopic. The macroscopic approach consists of the relationship based on the conservation of the particles in a granular bed:

$$\frac{\partial C}{\partial t} + U^s \frac{\partial C}{\partial x} = S, \tag{1.1}$$

with a model for the sink term $S = -\lambda U^s C$, where $C$ is the concentration of particles, $\lambda$ is the filter coefficient, and $U^s$ is the superficial velocity of the fluid. Equation 1.1 assumes that the particles convect with $U^s$ and do not have any relative velocity (later in Chapter 2 it will be shown that this relative velocity is not negligible for finite inertia particles). The present study is focused on clean-bed removal, where it is assumed that the effect of particle deposition on granules does not affect the fluid flow, or further deposition of particles on granules. The clean-bed removal assumption will give a constant filter coefficient $\lambda$ in a granular bed. The macroscopic approach is a semi-empirical approach, where the filter coefficient is obtained from experiments. The macroscopic approach is mainly used to find the change in the concentration of particles flowing through the granular bed and describe the overall behavior of the granular filter. The macroscopic approach do not provide any information about, or understanding of, the nature or mechanism of the filtration process.

The microscopic approach is a more fundamental approach to predict the granular filtration performance. This approach rests on the understanding of the nature and mechanisms of the transport and subsequent deposition of particles from the suspension to the granules of which the media is comprised. In this approach, the filter is modeled as an assemblage of single or unit collectors which have a certain known geometry. The fluid flow field around or through this geometry has to be described analytically based on the theories of low Reynolds number. Such model collectors include the isolated sphere or cylinder (Tien and Ramarao, 2007), the sphere in-cell model (Happel, 1958) and the constricted tube model (Tien and Ramarao, 2007). In the microscopic approach, the removal of particles is represented by a single-collector, or unit-collector, efficiency $\eta_s$. The single-collector efficiency is defined as the ratio of the overall particle deposition rate onto the collector to the convective transport of upstream particles towards the projected area of the collector. The single-collector efficiency is :

$$\eta_s = -\ln\left(\frac{C_e}{C_0}\right)\frac{2D_g}{3L\epsilon_s}, \tag{1.2}$$

where $C_0$ and $C_e$ are the inlet and outlet concentrations respectively, $L$ is the length of the granular bed, $D_g$ is the granule diameter, and $\epsilon_s$ is the granule volume fraction. The overall granular filter efficiency is :

$$\eta = 1 - \frac{C_e}{C_0}. \tag{1.3}$$

A primary reason for employing this single-collector efficiency is to obtain a basis for interpreting and correlating experimental data. Correlations can be found for single-collector efficiency by solving trajectory equations of particles in the porous media models (isolated sphere model, sphere in-cell model, and constricted tube model). These single-collector correlations can also be used to find the overall performance of a granular filter using Eqns. 1.2-1.3.

The drawbacks in using these porous media models is that these simple geometry models crudely approximate the chaotic and complex structure of a three dimensional (3D) granular bed (Tien and Ramarao, 2007). The flow fields in these porous media models are not representative of the flow field in a 3D granular bed (Gal et al., 1985; Tien and Ramarao, 2007). The prediction of correct filtration rate in a granular bed is highly dependent on the flow fields in a granular bed, since the particles convect in these flow fields. In order to accurately predict trajectories of particles in packed beds, flow models with random spheres in a packed bed are needed (Gal et al., 1985; Long and Hilpert, 2009; Pendse and Tien, 1982). Experiments can be used to obtain correlations for single-collector efficiency or filter-coefficient, however the experimental data from which these empirical correlations are deduced vary by an order of magnitude as can be seen in Figs. 1.1(a) and 1.1(b). Furthermore, experimental measurement of particle filtration rate along the granular bed is challenging because of limited optical access inside a granular bed. This motivates the development of a DNS–LPT approach with randomly distributed spheres that represent flow fields accurately and is valid in both low and moderate Reynolds number.

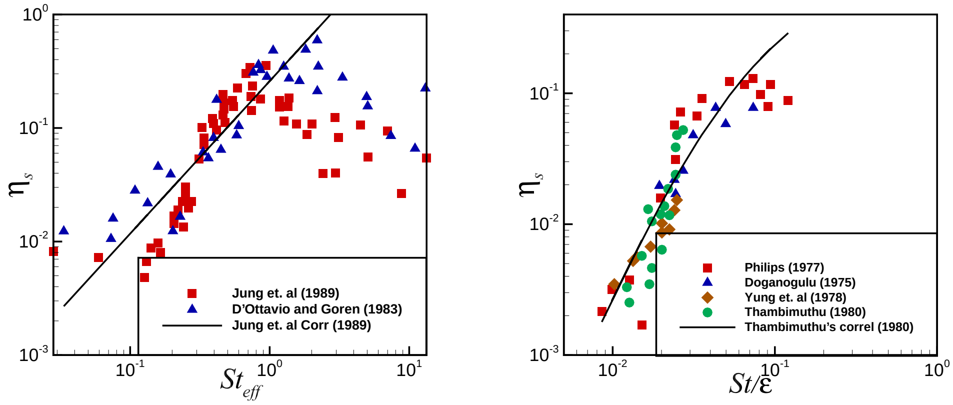

(a) (b)

Figure 1.1 (a) Comparison of Jung et al. (1989) data with his correlation and with the data of D'Ottavio and Goren (1983). (b) Comparison of Thambimuthu (1980)'s data with his correlation and other experimental data.

## 1.4 Challenges in developing models for granular filtration

The Stokes number of the particles considered in this study are typically in the range of 0.05 to 1.5 and the Reynolds number of the fluid flow range ($Re_m$) from 1 to 200. In this wide range of Stokes number and Reynolds number particle inertia is considered one of the most important and often the dominant factor for particle filtration in a granular bed. It is therefore necessary to have a fundamental understanding of filtration due to inertial effects in order to develop models for the CFD simulations that are valid over this wide range of particle Stokes number and fluid Reynolds number.

In the applications mentioned earlier in this chapter the particles treated are generally polydisperse. Polydispersity implies a range of particle Stokes numbers because of the $d_p^2$ dependence of the particle response time $\tau_p$. Particles with different Stokes number filter at different rates through a granular bed. At finite mean slip Reynolds number $Re_m = (1 - \epsilon_s) \langle W \rangle D_g \rho_f / \mu$, where $\epsilon_s$ is the granule volume fraction, and $\rho_f$ is the fluid density, the mean slip velocity affects the particle Stokes number because the fluid time scale in Stokes number is defined based on the mean slip velocity between fluid and granules.

Exhaust gases in thermal power plants and hot gases in bio-oil production flow at high velocities that fall in moderate and high Reynolds number range. At these high velocities usually particles bounce form the surface of the granules since the kinetic energy of the particles are able to overcome the adhesion energy on the surface of the granules. This bouncing phenomena reduces the granular filtration efficiency and this effect needs to be considered in the models developed for CFD simulations.

DNS is a very promising first-principles approach for developing accurate models. It has been extensively used for developing models for interphase momentum and heat transfer in gas-solid flows (Tenneti et al., 2011, 2013b; Hill et al., 2001a,b; Van der Hoef et al., 2005; Beetstra et al., 2007). We propose to use the DNS-LPT approach to investigate and develop the following:

1. The effects of particle inertia on granular filtration at both low and moderate Reynolds numbers.

2. Develop a model for filter coefficient $\lambda$ as a function of Stokes number, granular volume fraction and Reynolds number.

3. The effect of polydispersity on filtration or penetration of particles in a granular

bed.

4. Develop a model for adhesion probability $\gamma$ which can be used in CFD simulations

Finally, the models for the filtration of particles in a granular bed developed using Direct Numerical Simulation–Lagrangian Particle Tracking (DNS–LPT) approach are implemented and tested in CFD code ANSYS-FLUENT. The validation of CFD model is done with the experimental data of El-Hedok et al. (2011).

## 1.5 Research objectives

Based on the background presented in the preceding development, it is clear that a fundamental understanding of filtration of inertial particles, especially at moderate Reynolds number, is still lacking. It is also clear that for practical applications the extension of monodisperse filtration models to polydisperse models is essential. These research needs motivate the following research objectives:

1. Develop a fundamental understanding of filtration connecting averaged macroscale description to microscopic information from a single realization

2. Development of DNS–LPT approach to study particle filtration in a granular bed and quantify filtration in a single realization

3. Develop a model for filtration of monodisperse particulates in a granular bed using DNS–LPT simulations

4. Development of analytical models to predict the filtration of polydisperse particles at low and moderate Reynolds numbers

5. Investigate the effect of bouncing on filtration of particles for moderate Reynolds number

6. Develop a model for adhesion probability $\gamma$ for particles in a granular bed using DNS–LPT simulations
7. Implement and test the developed model from DNS–LPT approach into a CFD code ANSYS-FLUENT and simulate granular filtration

## 1.6 Accomplishments

- Developed a DNS–LPT approach to simulate granular filtration with sticking of particles on granule surface and bouncing of particles from granule surface
- Developed a model for filter coefficient as a function of modified effective Stokes number
- Developed an analytical framework to predict filtration of polydisperse particles
- Developed a model for adhesion probability as a function of modified effective Stokes number and normalized adhesion energy
- Developed a CFD model to simulate full scale moving-bed granular filter

## 1.7 Outline

The development of a monodisperse model for the filter coefficient using the DNS–LPT approach is described in chapter 2. Chapter 3 describes the filtration model for polydisperse particulates in gas-solid flow using DNS–LPT. In chapter 4, we investigate the bouncing of particles in a granular bed and develop a model for adhesion probability $\gamma$. The implementation and testing of the developed in a CFD code is done in chapter 5. Chapter. 6 is on modeling and simulation of sprays (which is a review paper the author is co-authoring with Dr. Shankar Subramaniam). Some conclusions and possible future works from this study are mentioned in chapter 7.

# CHAPTER 2. Improved modeling of granular filtration using direct numerical simulation

This chapter is a manuscript in preparation for journal publication : Improved modeling of granular filtration using direct numerical simulation authored by R. Kolakaluri, and S. Subramaniam.

## Abstract

The filtration of inertial particulates in steady flow through a granular bed is studied using a direct numerical simulation–Lagrangian particle tracking (DNS–LPT) approach (Kolakaluri et al., 2013). We use DNS–LPT results of penetration and single-collector efficiency to quantify the performance of a granular filter. We show that the penetration of inertial particulates in a granular filter is the outlet particle flux normalized by its inlet value, which reduces to normalized concentration (or number density) for inertialess particles. The dependence of single-collector efficiency on granule volume fraction, mean slip Reynolds number, and particle Stokes number is analyzed using DNS–LPT data. The effective Stokes number proposed by D'Ottavio and Goren (1983) is modified to reflect the dependence of single-collector efficiency on mean slip Reynolds number for different granule volume fractions, and the modified effective Stokes number gives a better collapse of single-collector efficiency over the range of granule volume fraction and mean slip Reynolds number considered. A model for the filter coefficient $\lambda$ is proposed in terms of the modified effective Stokes number that can be used in two–fluid

computational fluid dynamics (CFD) simulations of full-scale granular filter devices to model the filtration rate of particles.

## 2.1 Introduction

Granular filtration is a separation process whereby micron and sub-micron sized particles are removed from fluid streams by the presence of fixed (D'Ottavio and Goren, 1983) or moving (El-Hedok et al., 2011) granular beds. Both liquid and gas streams can be treated using granular filtration. Granular filtration finds applications in bio-oil production for filtration of fly ash from hot gases that are generated by fast pyrolysis of biomass (El-Hedok et al., 2011; Ritzert et al., 2004). It is also used in water and wastewater treatment (Davis, 2010; O'Melia, 1985). The basic principle of granular filtration is to pass the fluid-particle suspension through a granular bed. As the suspension flows through the granular bed, some of the particles present in the suspension move towards the granule and get deposited on their surface. The particles deposit on granule surfaces because of different filtration mechanisms.

The principal mechanisms for particle filtration are inertial impaction, interception, gravitation, and Brownian diffusion (Tien and Ramarao, 2007). Diffusional and gravitational effects in granular beds are significant only for very small particles ($d_p$ <1.0$\mu$m) at low velocities (Gutfinger and Tardos, 1979). This study is aimed towards applications that fall in the inertial regime where the particle diameter is greater than 1.0$\mu$m and fluid streams flow at higher velocity. A study of inertial effects in granular filtration is one of the principal contributions of this work. In the inertial regime, granular filtration is a function of Stokes number $St = \langle W \rangle d_p^2 \rho_p / 9 D_g \mu$ (D'Ottavio and Goren, 1983; Tien and Ramarao, 2007; Araújo et al., 2006), granule volume fraction $\epsilon_s$ and mean slip Reynolds number $Re_m = (1 - \epsilon_s) \langle W \rangle D_g \rho_f / \mu$, where $\langle W \rangle$ is the mean slip velocity between fluid and granules, $d_p$ is the particle diameter, $\rho_p$ is the particle density, $D_g$ is the granule diameter, $\rho_f$ is the fluid density and $\mu$ is the dynamic viscosity. A fundamental understanding of granular filtration for inertial particles ($d_p$ >1.0$\mu$m) over a wide range of particle Stokes number and mean slip Reynolds number is essential for design and development of granular filters.

Computational fluid dynamics (CFD) simulation of a granular filter is an efficient approach for design optimization because experiments are costly and time-consuming. In a two-fluid CFD simulation of a granular filter, the averaged equations governing mass, momentum are solved for both gas and granular phase and usually an advective scalar equation is solved for the particle phase (Bensaid et al., 2010; Wang et al., 2008):

$$\frac{\partial \phi}{\partial t} + \nabla \cdot (\langle \mathbf{V} \rangle \phi) = S_\phi, \tag{2.1}$$

where $\phi$ is the concentration of particles, $\langle \mathbf{V} \rangle$ is the mean particle velocity, and $S_\phi$ is the unclosed sink term due to particle filtration. Equation 2.1 can be closed by modeling the sink term as $S_\phi = -\lambda \langle \mathbf{V} \rangle \phi$, where $\lambda$ is the filter coefficient, that for moderate Reynolds number is given by a correlation that depends on the granule volume fraction $\epsilon_s$, mean slip Reynolds number $Re_m$, and particle Stokes number $St$.

Correlations for filter coefficient are usually obtained from macroscopic or microscopic approaches. The macroscopic approach is an empirical approach based on conservation of particles in a granular filter. The performance of a granular filter can be quantified by using the penetration $P = \dot{m}_{out}/\dot{m}_{in}$, where $\dot{m}_{in}$ is the mass of particles injected at the inlet and $\dot{m}_{out}$ is the mass of particles exited at the outlet of the granular bed. The penetration $P$ is related to the filter efficiency by $\eta = 1 - P$. If we assume that the filtration rate is constant along the length of the granular bed, then the penetration can be used to define a filter coefficient for granular bed

$$\lambda = -\frac{1}{L} \ln(P), \tag{2.2}$$

where $L$ is the length of the granular bed. However, the experimental data (D'Ottavio and Goren, 1983; Jung et al., 1989; Thambimuthu, 1980) found in literature from which empirical correlations are deduced vary by an order of magnitude, and have validity only under specific experimental conditions (Tien and Ramarao, 2007).

The microscopic approach is a more basic approach to describe the removal of particles in a granular bed based on fundamental understanding of the nature and mechanism of the transport and deposition of particles on granules. In this approach, the granular bed is modelled as an assembly of single or unit collectors of known geometry. The flow in a granular filter is usually modelled as an internal flow through a pore, or as an external flow around a granule. The flow field around this geometry (or through the pore) has to be described based on theories of low Reynolds number hydrodynamics. These geometries are used to mimic the flow inside a granular bed and are usually classified as either internal or external flow models. In internal flow models, the pore is usually taken as a cylindrical capillary or a constricted tube, and the walls of the pores act as a collector for particles. Jackson and Calvert (1966) used the capillary model for particle collection in a packed bed of spheres. Inertial particles deposit on the surface due to inertial impaction and interception filtration mechanisms mentioned earlier. Constricted-tube model, where the walls are not straight were developed by Petersen (1958); Payatakes et al. (1973); Niera and Payatakes (1978) to study granular filtration. The wall of a constricted-tube can be assumed to be parabolic (Payatakes et al., 1973), sinusoidal (Fedkiew and Newman, 1977) or hyperbolic (Petersen, 1958).

In the external flow models the granular bed is assumed to be a combination of homogeneously distributed spherical granules of uniform size. This model is based on two concentric spheres with the inner sphere being the granule located at the centre of the unit cell and the outer sphere consists of the fluid envelope with a free surface (Happel, 1958). The unit cells that represent the granular bed are identical and have the same granule volume fraction $\epsilon_s$ as the granular bed. To obtain the velocity profiles in the unit cell, sphere-in-cell models proposed by Lamb (1932); Happel (1958); Kuwabara (1959) are used.

The removal of particles by these internal or external flow models is represented by single-collector efficiency $\eta_s$. The single-collector efficiency is defined as the ratio of the overall particle deposition rate onto the collector to the transport of upstream particles towards the projected area of the collector. In the case of sphere-in-cell or spherical collector, the single collector efficiency is

$$\eta_s = \frac{4N}{U^s C_0 \pi D_g^2}, \tag{2.3}$$

where $N$ is the deposition rate on the collector, $C_0$ is the inlet concentration of particles, $U^s$ is the superficial velocity of the fluid and $D_g$ is the collector diameter. The single-collector efficiency can be related to the entire granular bed efficiency $\eta$ through a mass balance (see A) for a packed bed filter composed of spherical collectors, this relation is

$$\eta_s = \frac{-2D_g \ln(1-\eta)}{3\epsilon_s L}. \tag{2.4}$$

The goal of the microscopic approach is to predict $\eta_s$ using the flow models mentioned above, and to then use Eq. 2.4 to find the overall filter efficiency of the granular bed. Then the filter coefficient can be obtained from Eq. 2.2.

However, these flow models are far from representative of a practical granular bed (Tien and Ramarao, 2007). The pressure drop predicted by these simple flow models agree well with experimental data, but the velocity profiles differ significantly from the actual profiles in a granular bed (Gal et al., 1985). In order to accurately predict trajectories of particles in packed beds, flow models with random spheres in a packed bed are needed (Gal et al., 1985; Long and Hilpert, 2009). Hence, flow past a homogeneous random assembly of granules is a better representation of the complex flow structure in a granular bed. In Fig. 2.1(a), we show a simulation result obtained from particle–resolved direct numerical simulation, which gives a qualitative picture of the complex fluid streamlines inside a granular bed. Furthermore, in PR-DNS the instantaneous three-dimensional velocity and pressure fields are available, which provides a complete quantitative description of the flow. Figure 2.1(b) shows the probability density function (PDF) of tortuosity $\tau = c/L$ computed using PR-DNS for a simple cubic arrangement of particles, and for a random assembly of granules. Here $c$ is the path length of a fluid streamline and $L$ is the axial distance between the ends of the fluid streamline. It can be clearly seen in Fig. 2.1(b) that flow past a SC arrangement underpredicts the tortuosity compared to the random assembly of granules. Higher tortuosity of fluid streamlines aids in the filtration of particles because it is easier for inertial particles to deviate from fluid streamlines with increased tortuosity. This complicated flow structure of fluid streamlines is missing in the simple internal and external flow models mentioned above. The approximations made in simple flow models motivate us to develop a DNS–LPT approach to study granular filtration.

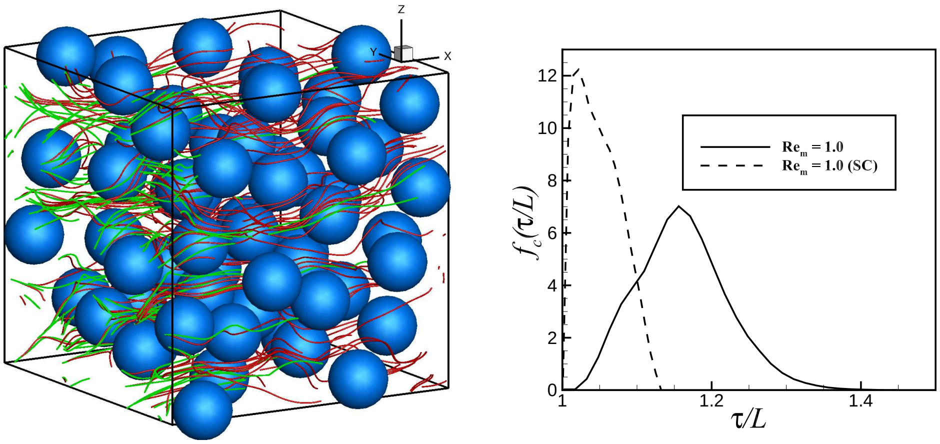

(a)

(b)

Figure 2.1 (a)Simulation result using particle–resolved DNS for a granule volume fraction of 0.5, mean slip Reynolds number of 1.0. The red lines are fluid streamlines and green lines are particle pathlines for a Stokes number of 0.25.(b)PDF of tortuosity of fluid streamlines obtained from DNS–LPT simulations for a granule volume fraction of 0.5, mean slip Reynolds number of 1.0 (dashed line is for a simple cubic arrangement and solid line is for a random granule arrangement).

In this study, we use a DNS–LPT approach (Kolakaluri et al., 2013) developed for granular filtration to understand inertial effects on the filtration of particles in a granular bed, and to develop a model for the filter coefficient $\lambda$ that can be used in two-fluid CFD simulations. The DNS–LPT approach used in this study was validated with the experimental data of D'Ottavio and Goren (1983) in Kolakaluri et al. (2013). The particle–resolved DNS used here to generate flow fields through a random assembly of granules is a first-principles approach that solves the governing Navier–Stokes (NS) equations with exact no-slip and no-penetration boundary conditions on granule surface and has been extensively validated in a comprehensive suite of test cases (Tenneti et al., 2011). It has been used to develop accurate models for interphase momentum and heat transfer in gas-solids flows (Tenneti et al., 2011, 2013b).

The chapter is organized as follows. In Section 2.2 we derive an expression for penetration from the evolution equation of number density of particles in a granular bed and using DNS–LPT results study the importance of mean slip flux for inertial particles. The DNS–LPT simulation methodology and the effect of numerical and physical parameters on DNS–LPT are discussed in Section 2.3. Finally, in Section 2.4 we discuss the dependence of single-collector efficiency on granule volume fraction, mean slip Reynolds number and particle Stokes number, and propose a model for the filter coefficient using DNS–LPT data.

## 2.2 Governing equations

### 2.2.1 Averaged equation for particles in a granular bed

The performance of a granular filter is usually quantified by granular filter efficiency or penetration. An expression for penetration of a granular filter can be derived from the evolution equation of the number density of particles. The evolution of number density

$n(\mathbf{x}, t)$ of particles in a granular bed is governed by

$$\frac{\partial n(\mathbf{x}, t)}{\partial t} + \frac{\partial \langle V_k \rangle \, n(\mathbf{x}, t)}{\partial x_k} = S, \tag{2.5}$$

where $\langle V_k \rangle$ is the mean particle velocity, and $S$ is the sink term due to the filtration of the particles. The number density and the mean particle velocity are obtained as

$$n(\mathbf{x}, t) = \int_{[\mathbf{v}]} f(\mathbf{x}, \mathbf{v}, t) d\mathbf{v}, \tag{2.6}$$

$$\langle V_k \rangle = \frac{\int_{[\mathbf{v}]} v_k f(\mathbf{x}, \mathbf{v}, t) d\mathbf{v}}{\int_{[\mathbf{v}]} f(\mathbf{x}, \mathbf{v}, t) d\mathbf{v}}, \tag{2.7}$$

where $f(\mathbf{x}, \mathbf{v}, t)$ is the one particle distribution function (Kolakaluri et al., 2013) (or droplet distribution function in the case of sprays (Subramaniam, 2001a, 2000a)).

Since the granular filtration problem is statistically homogeneous in $y$ and $z$ directions, the number density equation simplifies to

$$\frac{\partial n(x, t)}{\partial t} + \frac{\partial \langle V_x \rangle \, n(x, t)}{\partial x} = S, \tag{2.8}$$

where $\langle V_x \rangle$ is the mean particle velocity and $S$ is the sink term. In order to compare this number density equation to the scalar advection equation for the concentration of inertialess particles, we add a fluid flux term $\langle u_x^f \rangle n(x, t)$ to rearrange Eq. 2.8 as

$$\frac{\partial n(x, t)}{\partial t} + \frac{\partial \langle u_x^f \rangle n(x, t)}{\partial x} = \frac{\partial (\langle u_x^f \rangle - \langle V_x \rangle) n(x, t)}{\partial x} + S, \tag{2.9}$$

where $\langle u_x^f \rangle$ (Tenneti et al., 2011) is the averaged fluid velocity defined as

$$\langle u_x^f \rangle = \frac{\langle I_f u_x^f \rangle}{\langle I_f \rangle}, \tag{2.10}$$

and $I_f$ is the indicator function which is unity if the point lies in the fluid phase and zero in the granular phase. The mean slip flux term which is the first term on the right-hand side of Eq. 2.9 is non-zero for finite inertia particles and varies along the length of the granular bed and is negligible for particles with very low Stokes number, since the slip velocity between the particles and fluid is very small for low Stokes number. Low Stokes number ($St < 0.05$) particles usually follow the fluid stream lines very closely, which is not the case for finite inertia particles as they tend to deviate from fluid streamlines due to their inertia.

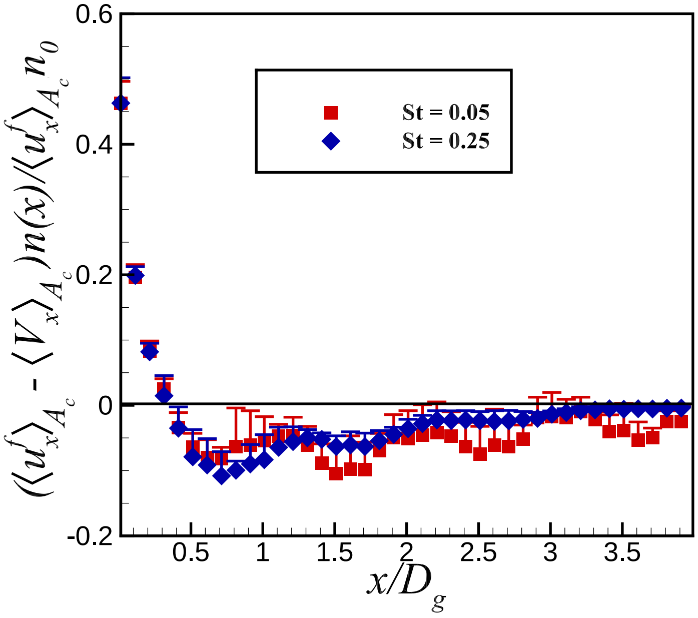

Figure 2.2 Steady state normalized mean slip flux $(\langle u_f\rangle_{A_c} - \langle V\rangle_{A_c})n/\langle u_f\rangle_{A_c} n_0$ along the flow domain for two particle Stokes number for a volume fraction 0.5 and mean slip Reynolds number 10.

Figure 2.2 generated from DNS–LPT data show that the mean slip flux is not zero and varies along the granular bed, and hence should not be neglected for finite inertia particles (The DNS–LPT simulation methodology is discussed in Section 2.3 and details about the calculation of number density from DNS–LPT simulations can be found in B). The velocities reported in Fig 2.2 are cross-sectional averaged velocities over the $y-z$ plane. The non zero mean slip flux shows that for finite inertia particles it is appropriate to use the number density equation (*cf*. Eq. 5.14) instead of the concentration equation:

$$\frac{\partial C}{\partial t} + U^s \frac{\partial C}{\partial x} = S_c, \tag{2.11}$$

where $C$ is the concentration of the particles in the fluid stream, $U^s$ is the superficial velocity of the fluid stream through the granular bed, and $S_c$ is the concentration sink term corresponding to particle filtration. The assumption made in Eq. 2.11 is that particles are flowing with superficial velocity $U^s$ and there is zero slip velocity between particles and fluid. This assumption is not applicable for finite inertia particles where there is a slip velocity between particles and fluid, as can also be seen in Fig. 2.4. The velocities reported in Fig. 2.4 are for a mean slip Reynolds number $Re_m = 10$, with fluid density and viscosity being $\rho_f = 1.0$ and $\mu = 0.012$, respectively. An important point worth noting is that the DNS equations are for a single realization, but the DNS–LPT results reported in this study are averaged over different granule configurations with the same granule volume fraction $\epsilon_s$ and radial distribution function $g(r)$. Since in this study we are focused on particles with finite inertia, we will be using Eq. 2.9 as the governing equation for particles flowing in the granular bed. An expression for penetration from the number density equation is presented in next section.

### 2.2.2 Expression for penetration

The granular filter considered in this study is a clean-bed filter, where the filtration rate reaches steady state due to fresh granules continuously being fed into the bed. At steady state, Eq. 2.8 can be written as

$$\frac{\partial \langle V_x \rangle n(x)}{\partial x} = S_x. \tag{2.12}$$

If we define the particle flux $J_x = \langle V_x \rangle n(x)$ and model the sink term as $S_x = -\lambda J_x$, the number density equation in terms of particle flux can be written as

$$\frac{\partial J_x}{\partial x} = -\lambda J_x, \tag{2.13}$$

where $\lambda$ is the filter coefficient. Integrating Eq. 2.13 along the granular bed from $x = 0$ to $x = L$, we obtain

$$\frac{J_x(x = L)}{J_x(x = 0)} = \exp\left(-\lambda L\right), \tag{2.14}$$

where $L$ is the length of the granular bed. The expression for penetration $P$ is defined as

$$P = \frac{J_x(x = L)}{J_x(x = 0)}. \tag{2.15}$$

In the case of inertialess particles $\langle V_x \rangle(x = 0) = \langle V_x \rangle(x = L)$ (since the particles will be advecting with the fluid velocity), and the penetration equation simplifies

$$P = \frac{n(x = L)}{n(x = 0)}. \tag{2.16}$$

Equation 2.16 is similar to $P = C(x = L)/C(x = 0)$ that is obtained from Eq. 2.11. In Fig. 5.5(a) the symbols show the decay of particle flux along the $x$ direction due to filtration (details regarding the calculations of particle flux and mass flow rate from DNS–LPT simulations can be found in B). The lines in Fig. 5.5(a) are the steady state mass flow rate of particles along the granular bed. The particle flux profiles predict the decay of particles due to filtration accurately, but this is not the case for the number density profiles shown in Fig. 5.5(b).

For particles with finite inertia, the penetration $P$ must be calculated from the particle flux $J$, because using the number density $n$ or concentration $c$ (Eq. 2.16) results in errors (cf. results in Fig. 5.5(b)). In the next section we will also show that Eq. 2.15 can also be derived from a simple mass balance.

### 2.2.3 Penetration calculation from mass balance

In the case of granular filtration experiments a simple mass balance of particles flowing through a granular bed (Ritzert et al., 2004) can be used to find the granular

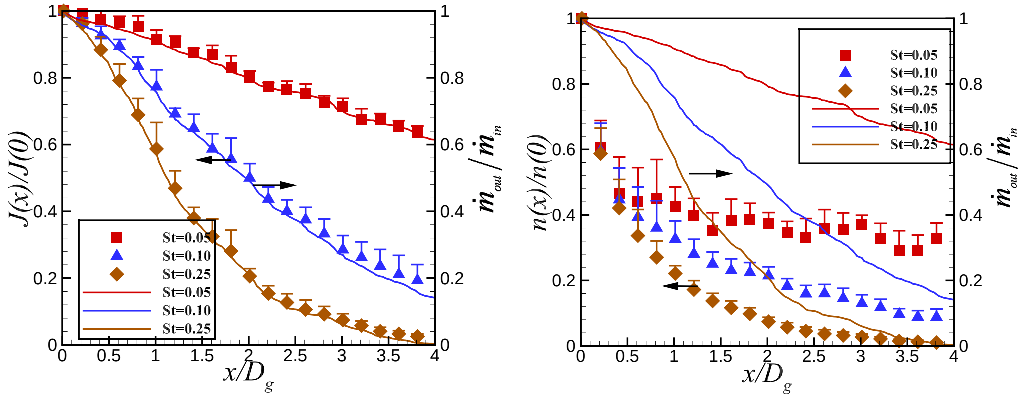

(a)

(b)

Figure 2.3 (a)Steady state normalized particle flux $J(x)/J(0)$ along the flow domain for three particle Stokes number for a volume fraction 0.5 and Reynolds number 10 and lines are mass flow rate of particles along the granular bed.(b)Steady state normalized number density $n(x)/n(0)$ along the flow domain for three particle Stokes number for a volume fraction 0.5 and mean slip Reynolds number 10 and lines are mass flow rate of particles along the granular bed.

filter efficiency $\eta$:

$$\eta = \frac{m_{in} - m_{out}}{m_{in}} = 1 - P, \tag{2.17}$$

where $m_{in}(T)$ and $m_{out}(T)$ are the mass of dust particles entering and exiting the granular filter over some time interval $T = t_{stop} - t_{ss}$ after reaching steady state. The mass of particles entering the granular filter $m_{in}(T)$ and mass of dust particles exiting the granular filter $m_{out}(T)$ can be written as

$$m_{in} = \int_{t_{ss}}^{t_{stop}} \int_{A_{in}} J_{in} dAdt = \int_{t_{ss}}^{t_{stop}} \int_{A_{in}} n_{in} \langle V \rangle_{in} dAdt, \tag{2.18}$$

$$m_{out} = \int_{t_{ss}}^{t_{stop}} \int_{A_{out}} J_{out} dAdt = \int_{t_{ss}}^{t_{stop}} \int_{A_{out}} n_{out} \left\langle V \right\rangle_{out} dAdt, \tag{2.19}$$

where $t_{ss}$ is the time required for the granular bed to reach steady state, $t_{stop}$ is the time the granular bed is allowed to run, $A_{in}$ is the inlet area of the granular bed and $A_{out}$ is the outlet area of the granular bed. Assuming uniform inflow and outflow particle fluxes, Eqs. 2.18 and 2.19 can be simplified to

$$m_{in} = J_{in} \int_{t_{ss}}^{t_{stop}} \int_{A_{in}} dAdt = J_{in}(t_{stop} - t_{ss}) A_{in}, \tag{2.20}$$

$$m_{out} = J_{out} \int_{t_{ss}}^{t_{stop}} \int_{A_{out}} dAdt = J_{out}(t_{stop} - t_{ss}) A_{out}. \tag{2.21}$$

Since $A_{in}$ and $A_{out}$ are equal, from Eq. 2.17 the penetration is simply

$$P = \frac{J_{out}}{J_{in}}. \tag{2.22}$$

The penetration equation obtained from mass balance is consistent with Eq. 2.15. In the next section, we briefly describe the simulation methodology and establish the numerical convergence and accuracy present parametric study of the DNS–LPT approach (Kolakaluri et al., 2013).

## 2.3 DNS-LPT : Simulation approach

### 2.3.1 Governing equations in DNS–LPT

In the DNS–LPT approach, we use a particle-resolved DNS methodology called Particle–resolved Uncontaminated–fluid Reconcilable Immersed Boundary Method (PUReIBM) approach to obtain three-dimensional fluid phase flow fields around the granules. PUReIBM solves the governing Navier–Stokes(NS) equations with exact boundary conditions on granule surface. The governing equations solved in PUReIBM are

$$\frac{\partial u_i}{\partial x_i} = 0, \tag{2.23}$$

and

$$\rho_f \frac{\partial u_i}{\partial t} + \rho_f S_i = -g_{IBM,i} + \mu \frac{\partial^2 u_i}{\partial x_j \partial x_j} + f_{u,i}, \tag{2.24}$$

where $g_{IBM,i}$ is the pressure gradient, $S_i$ is the convective term, $f_{u,i}$ is the additional immersed boundary force term that accounts for the presence of solid particles in the fluid-phase by ensuring zero slip and zero penetration boundary conditions at the granule-fluid surface. The complete details of the PUReIBM solver are discussed in Tenneti et al. (2011); Garg et al. (2010b).

The other solid phase consists of fine particles that are suspended in the fluid phase and these are tracked as point particles in a Lagrangian frame as they are carried through the granular bed. In the LPT approach the dispersed phase consisting of $N_p$ particles is represented in a Lagrangian frame at time $t$ by $\{\mathbf{X}^{(i)}(t), \mathbf{V}^{(i)}(t), i = 1, ......, N_p(t)\}$, where $\mathbf{V}^{(i)}(t)$ denotes the $i$th particle's velocity and $\mathbf{X}^{(i)}(t)$ represents its position. Note that in this LPT implementation each particle represents a physical particle, and this is not a parcel method (Subramaniam, 2013). The position and velocity of the particles evolve by

$$\frac{d\mathbf{X}^{(i)}(t)}{dt} = \mathbf{V}^{(i)}, \tag{2.25}$$

and

$$\frac{d\mathbf{V}^{(i)}(t)}{dt} = \frac{\mathbf{f}^{(i)}}{m_p^{(i)}} = \mathbf{A}^{(i)}, \tag{2.26}$$

where $m_p^{(i)}$ is the mass and $\mathbf{f}^{(i)}$ and $\mathbf{A}^{(i)}$ are the instantaneous force and acceleration experienced by the $i$th particle respectively. Only the quasi-steady drag contribution to the instantaneous force is considered and it is modeled using the drag correlation by Schiller and Naumann (1933) as

$$\mathbf{f}^{(i)}(t) = 3\pi\mu \left|\mathbf{u}_f(\mathbf{X}_p^{(i)}) - \mathbf{V}_p^{(i)}\right| d_p(1 + 0.15Re_p^{0.687}), \tag{2.27}$$

where $Re_p$ is the particle Reynolds number based on slip velocity between the particle and fluid (not granule) and $\left|\mathbf{u}_f(\mathbf{X}_p^{(i)}) - \mathbf{V}_p^{(i)}\right|$ is the magnitude of the instantaneous slip velocity between particle and fluid at the particle location. In the present study, the mass loading $[\rho_p N_p \pi d_p^3 / 6\epsilon_f \rho_f \approx 1 \times 10^{-5}]$ of the dispersed phase is assumed to be negligible, and so the fluid momentum balance is assumed to be unaffected by particle-fluid momentum transfer. (The total particle drag is around $\approx 2 \times 10^{-4}$ that of the total granules drag for mean slip Reynolds number $Re_m = 10$ and granule volume fraction $\epsilon_s = 0.5$.) Therefore, only one-way coupling is considered in the DNS–LPT simulations.

### 2.3.2 Simulation methodology

The DNS-LPT simulation of granular filtration is performed for steady fluid flow that is established by maintaining a constant mean pressure gradient through a homogeneous fixed assembly of granules. Granules are initialized in a lattice arrangement corresponding to a specified granule volume fraction $\epsilon_s$. The granules are initialized with a Maxwellian velocity distribution and allowed to collide elastically to obtain an equilibrium configuration that is taken as a fixed particle assembly for the flow calculation. The mean pressure gradient that corresponds to a specified mean slip Reynolds number is imposed and the flow is allowed to evolve in pseudo-time until it attains the desired flow rate.

Since particles are being filtered, the particle number density and flux vary along the streamwise direction, but they are homogeneous in the cross-stream direction. Lagrangian tracking of particles is done in steady flow fields past fixed granule assembly obtained from PUReIBM. The particles are continuously injected at a specified injection rate $\dot{m}_{in}$ into the computational domain. The boundary conditions for both the cases are inflow at $x = 0$ and outflow at $x = L$, where $L$ is the length of the computational domain. In the $y$ and $z$ directions periodic boundary conditions are imposed on the particles. A particle is assumed to be trapped by the granular assembly when the distance between the centers of the granule and the particle is less than $(r_p + D_g/2)$ , where $r_p$ is the radius of the particle and $D_g$ is the diameter of the granule. This trapping criterion accounts for both inertial impaction and interception. The particles are removed from the simulation at the outlet plane $x = L$.

### 2.3.3 Effect of particle initial conditions

When particle at the inlet plane are initialized with the fluid velocity at the particle location we find that the mean velocity of the particles is less that the mean fluid velocity in the intial part of the bed (see Fig. 2.4).(The velocities reported in Fig 2.4 and later in this study are cross-sectional averaged velocities along $x$ direction. The procedure to calculate these averaged velocities is given in B.) This is because particles being initialized at a constant rate at the inlet plane in a inhomogeneous velocity field. The errors bars shown in all the DNS-LPT simulations reported in this study represent 95% confidence intervals obtained from averaging over 5 independent simulations corresponding to different granule configurations with the same volume fraction $\epsilon_s$ and $g(r)$ (radial distribution function).

When particles are initialized with zero particle velocity (see Fig. 2.5), the same trend of the mean velocity of the particles was observed as seen when particles are initialized with fluid velocity (see Fig. 2.4). The velocities reported in Figs 2.4 - 2.5 are

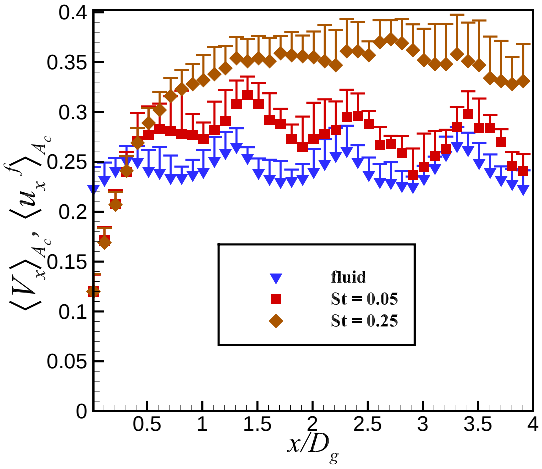

Figure 2.4 Variation of mean particle velocity $\langle V \rangle_{A_c}$ for two particle Stokes number along the granular bed for a volume fraction 0.5 and mean slip Reynolds number 10 with particles initialized with fluid velocity and the mean fluid velocity $\langle u_f \rangle_{A_c}$ is shown for reference.

for a mean slip Reynolds number $Re_m = 10$, with fluid density and dynamic viscosity being $\rho_f = 1.0$ and $\mu = 0.012$, respectively. An important conclusion from both the initial conditions is that the effect of initial conditions on mean particle velocity $\langle V \rangle$ is not seen beyond $x/D_g > 0.5D_g$. Figure 2.6 shows that the effect of particle initial conditions is not seen in the particle flux plots, which further motivates us to use particle flux for calculating penetration. The numerical and physical parameters used in the DNS–LPT simulations are discussed in the next section.

### 2.3.4 Numerical and physical parameters

The computational domain is a cube with sides of length $L$. Each side is discretized using $M$ grid cells. The spatial resolution is represented by the number of grid cells across the diameter of a granule, which is $D_m = D_g/\Delta x$, where the grid spacing $\Delta x = L/M$. All length scales are normalized by the granule diameter $D_g$ and for a given granule volume

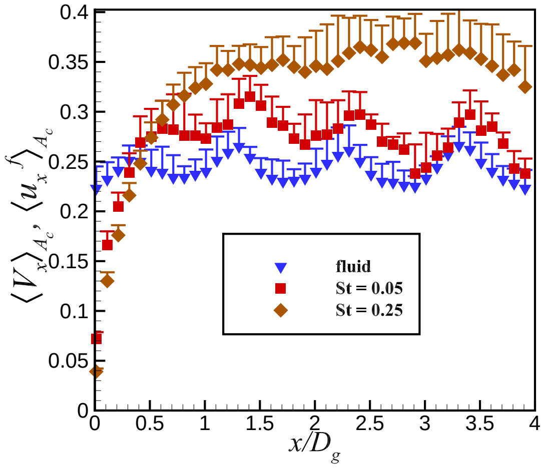

Figure 2.5 Variation of mean particle velocity $\langle V \rangle_{A_c}$ for two particle Stokes number along the granular bed for a volume fraction 0.5 and mean slip Reynolds number 10 with zero initial particle velocity and the mean fluid velocity $\langle u_f \rangle_{A_c}$ is shown for reference.

fraction $\epsilon_s$ the number of granules $N_g$ in the computational domain is determined based on $L/D_g$ by

$$N_g = \frac{6\epsilon_s}{\pi}\left(\frac{L}{D_g}\right)^3. \tag{2.28}$$

The physical parameters that define the granular filter are granule volume fraction $\epsilon_s$, mean slip Reynolds number $Re_m$. The particle Stokes number $St$ conjunction with these parameters determines the filtration efficiency and the length of the bed $L/D_g$. For a fixed length of bed $L/D_g$, $D_m$ is the only numerical parameter. The calculation of steady state penetration from DNS–LPT simulations and the effect of numerical and physical parameters on DNS–LPT results are discussed in next section.

#### 2.3.4.1 Calculation of penetration from DNS–LPT simulations

The DNS–LPT simulations are considered to reach steady state once $\dot{m}_{out}$ reaches a steady value in time. An important point to be noted that the particle mass flux $\dot{m}_{in}$ or

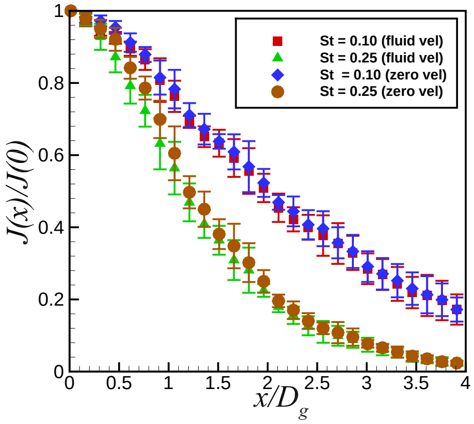

Figure 2.6 Steady state normalized particle flux $J(x)/J_0$ along the flow domain for particle Stokes number 0.10 and 0.25 for a volume fraction 0.5 and mean slip Reynolds number 10 with zero initial particle velocity and particles initialized with fluid velocity.

$\dot{m}_{out}$ is the particle mass flux through the crossectional area of the fluid along the flow direction. It can be seen in Fig. 2.9 that the penetration reaches steady state after time $T_{ss}$, when $T_{ss}$ is a function of particle Stokes number. The penetration is calculated as

$$P = \frac{\int_{T_{ss}}^{T_{stop}} \dot{m}_{out} dt}{\int_{T_{ss}}^{T_{stop}} \dot{m}_{in} dt} = \frac{m_{out}}{m_{in}} = \frac{J_{out}}{J_{in}}. \tag{2.29}$$

#### 2.3.4.2 Numerical convergence study

The convergence of DNS–LPT simulations is established by studying the influence of grid resolution $D_m$ on penetration $m_{out}/m_{in}$. Figure 2.7 shows that the penetration is converged for $D_m \geq 30$. The DNS–LPT simulation results reported in this study are all performed with $D_m = 40$.

#### 2.3.4.3 Effect of physical parameters on penetration

The physical problem changes with change in the length $L$ of the granular bed. The variation of penetration with the length of the bed is shown in Fig. 2.8. Increase in

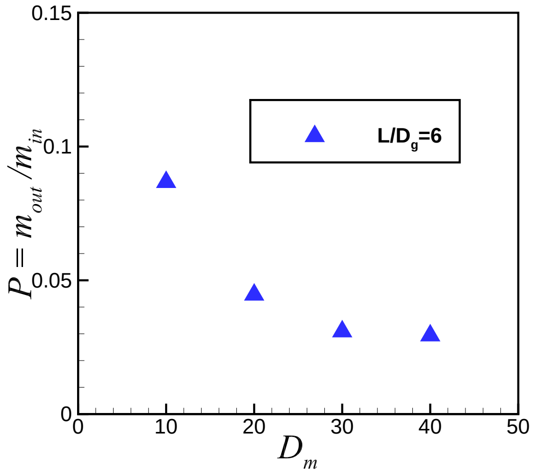

Figure 2.7 Variation of penetration for a particle Stokes number of $St = 0.25$, granule volume fraction $\epsilon_s = 0.4$, and mean slip Reynolds number $Re_m = 20$ with grid resolution $D_m$.

length of the bed reduces the penetration of particles due to increased probability of particle filtration in longer beds.

As Fig. 2.9 shows, the particle flux reaches a steady value after time $T_{ss}$. Figure 2.9 shows an increase in the penetration with Stokes number and it also shows that time $T_{ss}$ increases with decrease in Stokes number as high Stokes number particles reach steady state early because of increase in slip velocity between fluid and particle with Stokes number. For $St = 0.10$ the particle mass flux reaches a steady value for $T_{ss} > 2000/\tau_f$(or 500 flow through times). Therefore, if $T_{ss} > 2000/\tau_f$ in Eq.23, the penetration P (which is the ratio of the total outlet particulate mass to that at the inlet) can also be expressed as the ratio of steady outlet mass flux to its inlet value.

The number of particles $N_p$ injected at the inlet is a physical parameter. The choice of the optimal value represents a trade off between minimizing statistical error (that decreases with increasing $N_p$) and keeping the volume fraction and mass loading low enough that, interparticle interaction and particle-fluid interaction can be neglected.

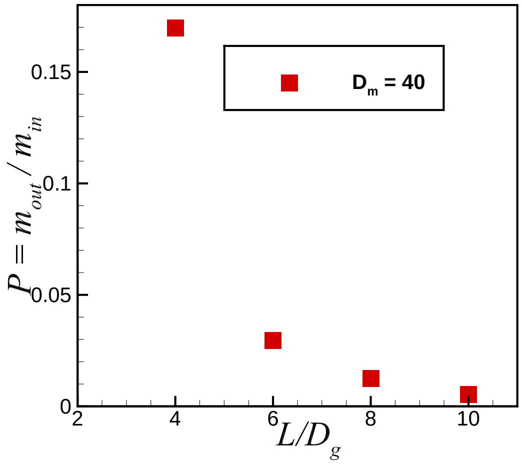

Figure 2.8 Variation of penetration for a particle Stokes number of $St = 0.25$, granule volume fraction $\epsilon_s = 0.4$, mean slip Reynolds number $Re_m = 20$ with the length of bed $L/D_g$.

The effect of the number of particles injected at the inlet of computational domain on penetration is reported in Figure 2.10. The mass flow rate of particles $\dot{m}_{in}$ at the inlet is calculated from the number of real particles $N_P$ injected at the inlet. The error bars in Fig. 2.10 are the standard deviation obtained from averaging the penetration over time. A value of $N_p = 500$ is chosen such that particle–fluid interaction can be neglected and good statistics are obtained. All the simulations reported in this study are performed with $N_p = 500$. In the next section we study the effect of particle Stokes number, granule volume fraction and mean slip Reynolds number on the single-collector efficiency and propose a model for filter coefficient using DNS–LPT data.

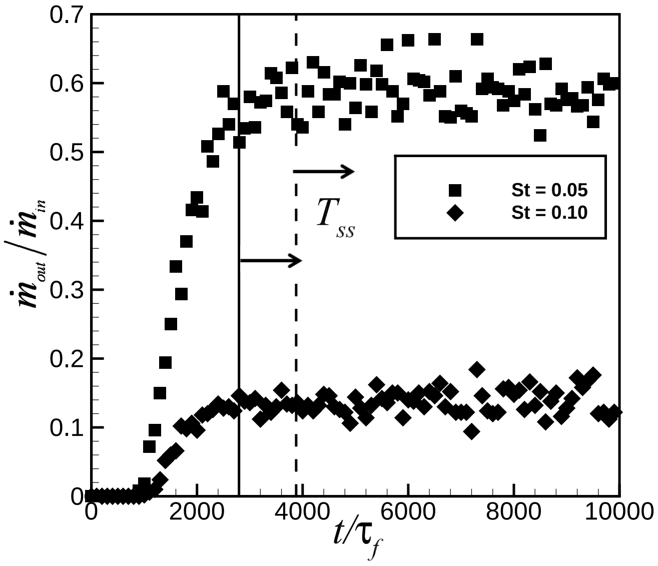

Figure 2.9 Variation of particle mass flux for a particle Stokes number of $St = 0.05$ and $St = 0.10$ for a granule volume fraction $\epsilon_s = 0.5$, mean slip Reynolds number $Re_m = 10$ with time $t$ normalized by the fluid time scale $\tau_f$.

## 2.4 Results

### 2.4.1 Single–collector efficiency of a granular filter

The single-collector efficiency defines the rate of particle collection as the fraction of particles flowing through an area equal to the projected area of the collector in a plane normal to the direction of the flow. The single-collector efficiency of a granular filter is a function of granule volume fraction, mean slip Reynolds number and particle Stokes number. The single-collector efficiency is mainly used to compare the performance of granular filters with different granule volume fraction and bed length. In DNS–LPT the granular filter efficiency is calculated using Eq. 2.17 and then Eq. 2.4 is used to find the single-collector efficiency.

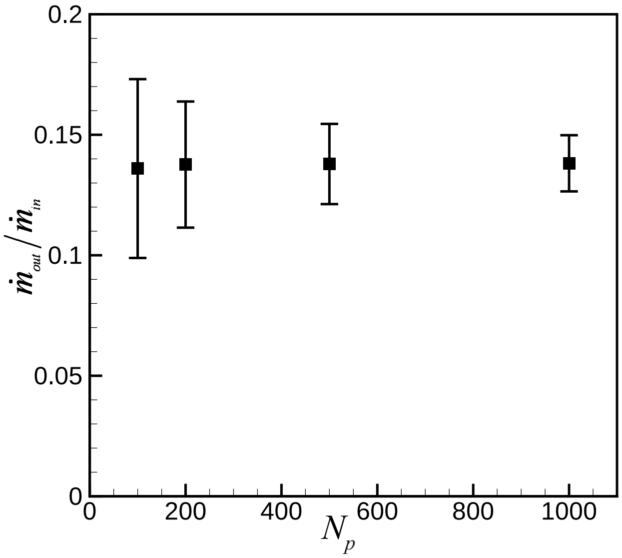

Figure 2.10 Variation of penetration for a particle Stokes number of $St = 0.10$, granule volume fraction $\epsilon_s = 0.5$, mean slip Reynolds number $Re_m = 10$ with the $N_p$ (particles initialized at the inlet).

#### 2.4.1.1 Dependence on granule volume fraction

We found from DNS–LPT data that the single-collector efficiency has a strong dependence on granule volume fraction as shown in Fig. 2.11. The increase in single-collector efficiency with granule volume fraction is due to a combination of two factors: (i) increase in projected area of granules, and (ii) increase in the tortuosity of fluid streamlines that makes it difficult for inertial particles to follow fluid streamlines, thereby resulting in their filtration by granules. It can be seen in Figs. 2.11(a)-2.11(d) that for medium Stokes number($0.05 < St \leq 0.10$) the increase in single-collector with granule volume fraction is quadratic, and for high Stokes number ($St > 0.10$) the increase in single-collector efficiency with granule volume fraction is linear for all $Re_m$. The change in trend with granule volume fraction for medium and high Stokes number is due to the increase in tortuosity with volume fraction. Tortuosity makes medium Stokes number particles deviate from fluid streamlines, but this effect in not significant for high Stokes number particles because they deviate from fluid streamlines even at small tortuosity due to their higher inertia. A point worth noting is that in Figs. 2.11(b)-2.11(d) the single-collector efficiency at high particles Stokes number is greater than 1. The unphysical value of single-collector efficiency is due to Eq. 2.4, where the calculated single-collector efficiency exceeds unity for penetration close to zero. This is one of the reasons for developing a model for the filter coefficient $\lambda$ instead of $\eta_s$, as described in Sec. 2.5.

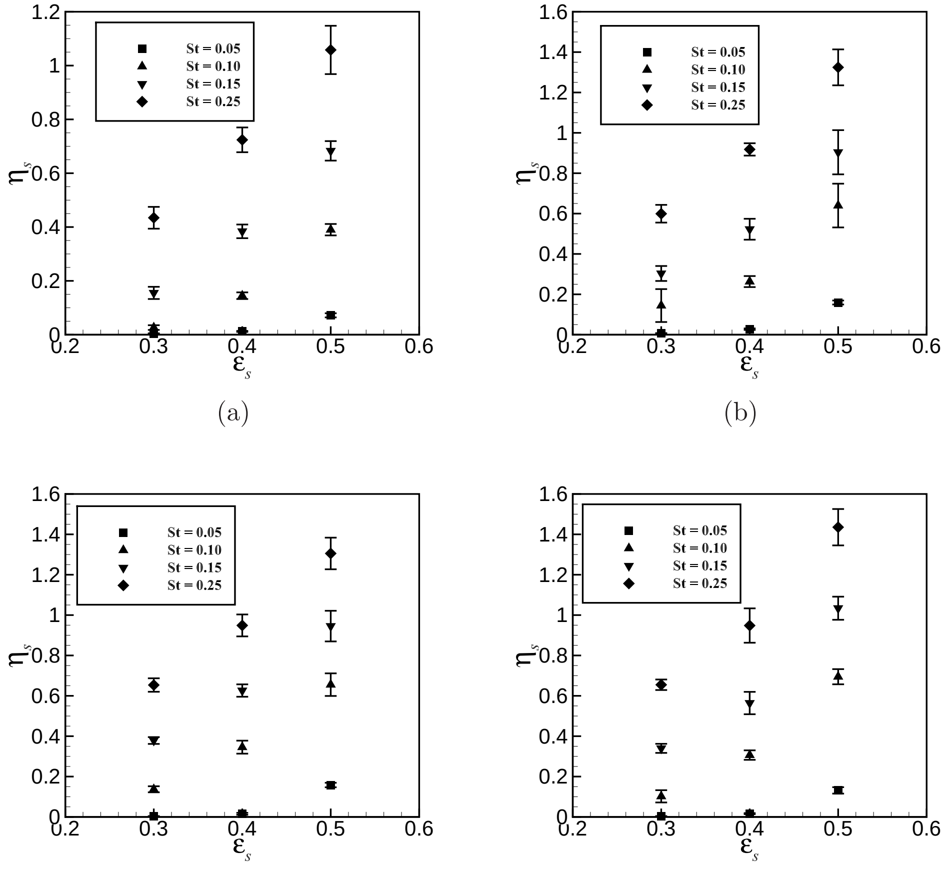

(a) (b)

(c) (d)

Figure 2.11 Variation of single-collector efficiency with granule volume fraction for different particle Stokes number: (a)$Re_m = 1$. (b)$Re_m = 10$. (c)$Re_m = 50$. (d)$Re_m = 100$.

#### 2.4.1.2 Dependence on mean slip Reynolds number

The single-collector efficiency increases with mean slip Reynolds number for $Re_m \leq 10$ (see Fig. 2.12). For $Re_m > 10$, the single-collector efficiency tends to asymptote to a limiting high $Re_m$ value. This asymptotic high $Re_m$ limit of the single-collector efficiency with mean slip Reynolds number is predominant at high granule volume fractions (Figs. 2.12(b)-2.12(c)).

The reason for this asymptotic dependence of single-collector efficiency on mean flow Reynolds number for $Re_m > 10$ can be better understood by looking at the tortuosity of fluid streamlines. The tortuosity $\tau = c/L$ gives us an idea of the departure of fluid streamlines from straight line trajectories in a porous media, where $c$ is the length of a fluid streamline and $L$ is the linear distance between the ends of that fluid streamline. The tortuosity of fluid streamlines is an important factor that aids in the filtration of the particles because the more tortuous a fluid streamline the easier it is for finite inertia particles to deviate from the streamline and get filtered by the granules. It can be seen in Figs. 2.13(a)-2.13(b) that with increase in mean slip Reynolds number the tortuosity of fluid streamlines increases. The probability of finding highly tortuous fluid streamlines increases with $Re_m$(see Fig. 2.13(a)). The presence of highly tortuous streamlines increases the single-collector efficiency for $Re_m \leq 10$. For $Re_m > 10$, the presence of high tortuous fluid streamlines is less effective in increasing the single-collector efficiency because with increase in mean slip Reynolds number the residence time of particles in the granular bed decreases. Therefore, the particles have less time to deviate from tortuous streamlines and get deposited on the granules. This asymptotic behavior of single-collector efficiency is found at all particle Stokes number.

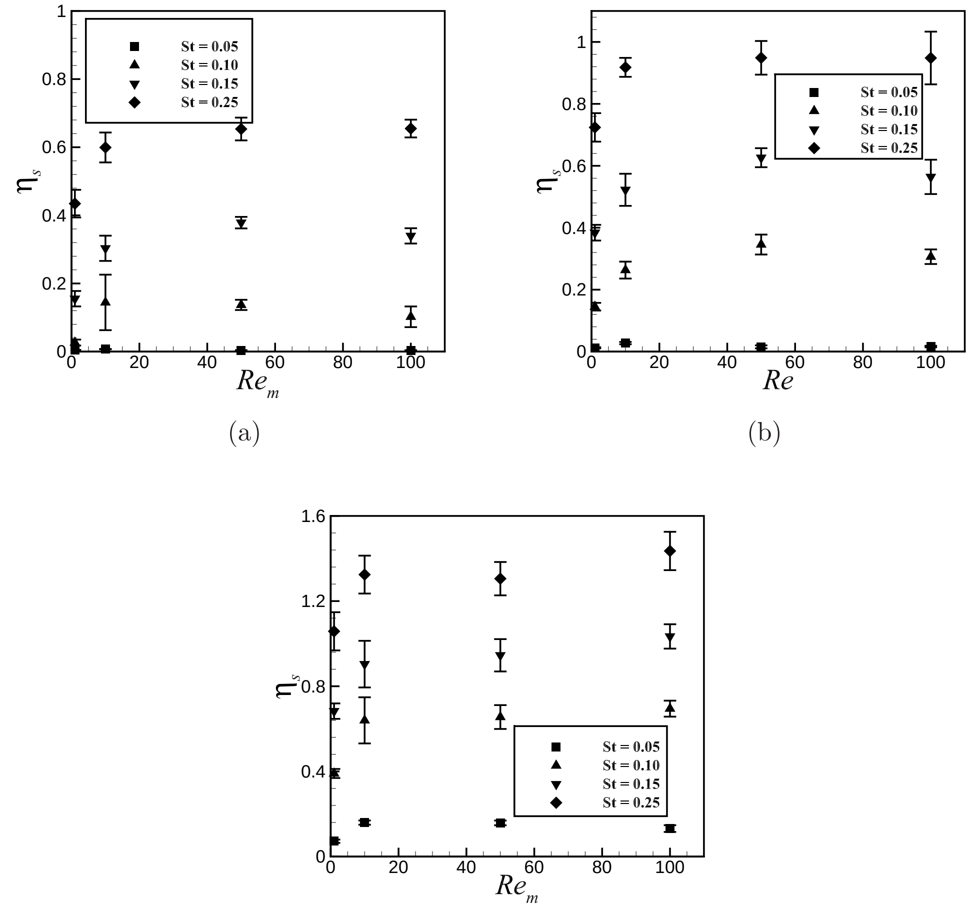

(a)

(b)

(c)

Figure 2.12 (a)Variation of single-collector efficiency with mean slip Reynolds number at a granule volume fraction of 0.3 for different particle Stokes number (b)Variation of single-collector efficiency with mean slip Reynolds number at a granule volume fraction of 0.4 for different particle Stokes number. (c)Variation of single-collector efficiency with mean slip Reynolds number at a granule volume fraction of 0.5 for different particle Stokes number.

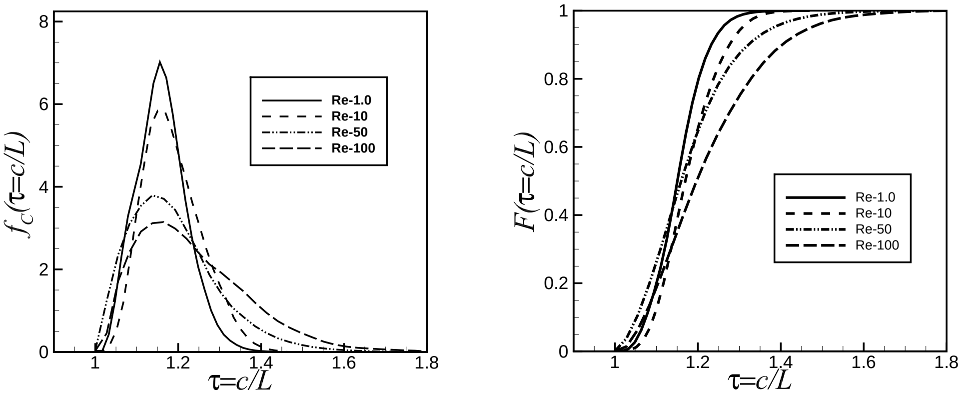

(a) (b)

Figure 2.13 (a)The probability density function of tortuosity $\tau = c/L$ of the fluid streamlines in a granular bed for different mean flow Reynolds number at a volume fraction of 0.5. (b)The cumulative density function of tortuosity $\tau = c/L$ of the fluid streamlines in a granular bed for different mean flow Reynolds number at a volume fraction of 0.5.

#### 2.4.1.3 Dependence on particle Stokes number

In the case of inertial particles, filtration is a strong function of the particle Stokes number. Particles with higher Stokes number deviate more from fluid streamlines and this increases the deposition of particles on granules. Figs. 2.12(a)-2.12(c) show that the single-collector efficiency increases with particle Stokes number for mean slip Reynolds number in the range $Re_m : 1-100$. We investigate the effect of particle Stokes number on granule surface coverage due to particle deposition as shown in Fig 2.14. This simulation result gives a qualitative picture of particle deposition on granule surfaces for a particle Stokes number of $St = 0.25$. Particle deposition is observed mainly on the portion of the granule surface facing the flow, and leading particles shield those behind them from particle deposition.

The PDF of particle deposition on granules gives a quantitative picture of the same phenomenon. Figure 2.15(a) indicates that most of low Stokes number particles ($St =$

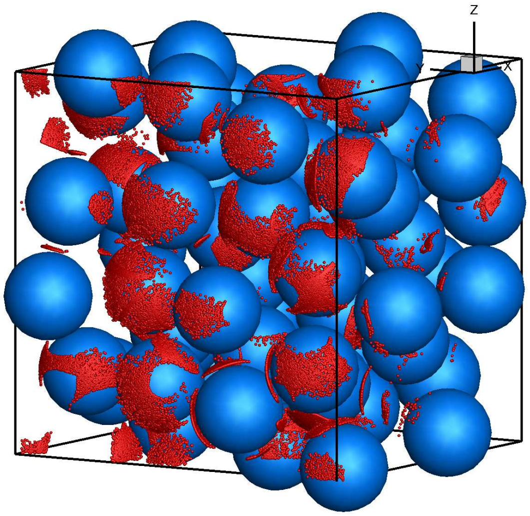

Figure 2.14 Deposition of particles in a random assembly of granules using DNS–LPT for a granule volume fraction of 0.5, mean slip Reynolds number of 1.0 and particle Stokes number 0.25. The red spheres are the particles and blue spheres are granules.

0.05) deposit within polar angle $\theta \leq 50$ degrees and the probability of particles depositing for $\theta > 50$ degrees increases with increase in particle Stokes number. As mentioned before, inertial particles tend to deviate from fluid streamlines and get deposited on the granule surface, and their deviation from the fluid streamlines increases with increase in particle Stokes number. The particle deviate from fluid streamline due to two reasons: one is due to high fluid velocity gradients close to the granule surface, and the other is due to high curvature of streamlines. The region close to the granule surface has high velocity gradients and the streamlines are highly curved, and hence it is easier for the particles to deviate from the fluid streamline. The deviation from fluid streamline increases with particle Stokes number for a specified velocity gradient and curvature of the streamlines. For particles slightly away from the granule surface the particle deviation from fluid streamline is mainly due to the curvature of the fluid streamlines, where the particles with high Stokes number are able to deviate from the fluid streamlines.

Figure 2.15(b) shows that for small particle Stokes number ($St = 0.05$), 95% of particles deposit within $\theta \leq 50$ degrees and only 5% of particles deposit over $\theta > 50$ degrees, but with increase in particle Stokes number more particles deposit at polar angle $\theta > 50$ degrees and also some of high Stokes number particles ($St = 0.10$ & $0.25$) on granule surface at polar angles $\theta > 50$ degrees is attributed to the high curvature of the streamlines as the velocity gradients are very small away from the granule surface. As expected there is no deposition of particles for $\theta > 95$ degrees because once the particles pass the front portion of the granule then the probability of deposition of particles on the aft portion of the granule is very less. This analysis of particle deposition on granule surface give us information on the area coverage of granule surface due to particle deposition for different particle Stokes number.

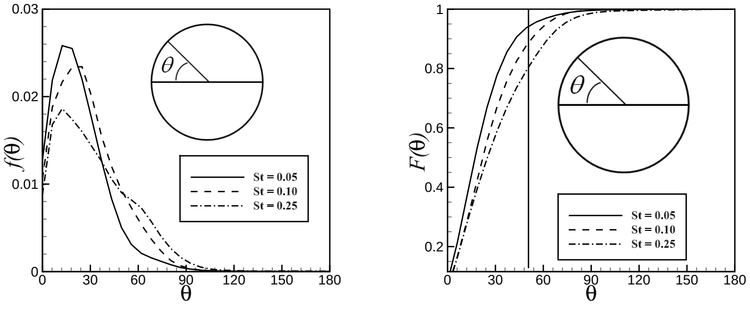

(a) (b)

Figure 2.15 (a)Probability density function of particle deposition with polar angle in a random assembly of granules for a granule volume fraction of 0.5, mean slip Reynolds number of 1.0 and particle Stokes numbers 0.05, 0.10 and 0.25, and (b)the corresponding cumulative distribution function.

## 2.5 Model for the filter coefficient

For moderate Reynolds numbers the filter coefficient $\lambda$ or single-collector efficiency $\eta_s$ is a function of Stokes number, granule volume fraction and mean slip Reynolds number. D'Ottavio and Goren (1983) proposed a correlation for single-collector efficiency in terms of effective Stokes number $St_{eff}$, where the effective Stokes number was proposed by D'Ottavio and Goren (1983) to collapse single-collector efficiency data for moderate Reynolds number by combining the three independent dimensionless groups $Re_m$, $St$ and $\epsilon_s$ as given by Eqs. 4.12 and 4.13.

The expression for effective Stokes number was obtained from two different theories: low Reynolds number hydrodynamics and boundary layer theory. The fluid velocity field for low Reynolds number flow through a granular bed is a strong function of granule volume fraction $\epsilon_s$. For moderate and high Reynolds number it is a function of both granule volume fraction and Reynolds number. For low Reynolds number the Happel (1958) model results in an expression (Eq. 4.13) where velocity field is a function of granule volume fraction $\epsilon_s$. Since there is no available theory for velocity fields at high Reynolds number flow through packed beds, D'Ottavio and Goren (1983) used the result of boundary layer theory (Schlichting, 1968) for flow past an isolated sphere with a modification to include the effect of granule volume fraction and proposed an expression ($1.14 Re_m^{1/2}(1-\epsilon_s)^{-3/2}$) to represent the change in velocity field in a granular bed with granule volume fraction and mean slip Reynolds number. D'Ottavio and Goren (1983) pointed that the boundary layer theory based expression is mostly valid at high mean flow Reynolds number. Based on these two theories D'Ottavio and Goren (1983) proposed an approximate expression (Eq. 4.12) for the effective Stokes number by combining both Eq. 4.13 and $1.14 Re_m^{1/2}(1-\epsilon_s)^{-3/2}$ to obtain an expression that is assumed to be valid over the entire Reynolds number range.

$$St_{\text{eff}} = \left[ A(\epsilon_s) + 1.14 Re_m^{1/2} \left(1-\epsilon_s\right)^{-3/2} \right] \frac{St}{2}, \tag{2.30}$$

$$A(\epsilon_s) = \frac{(6 - 6{\epsilon_s}^{5/3})}{(6 - 9{\epsilon_s}^{1/3} + 9{\epsilon_s}^{5/3} - 6{\epsilon_s}^{2})}. \tag{2.31}$$

We used Eq. 4.12 to plot the single-collector efficiency at different mean flow Reynolds number and granule volume fraction. It can be seen in Fig. 2.16 that the single-collector

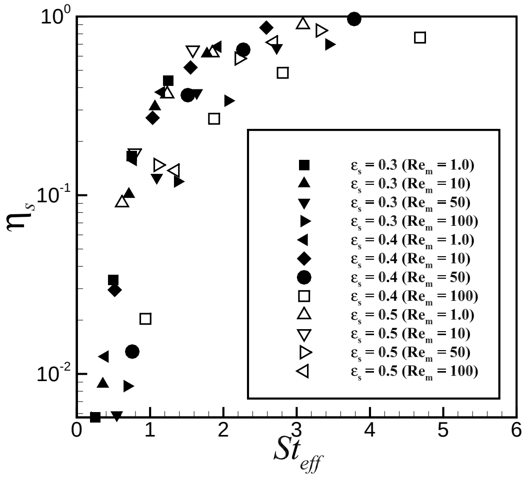

Figure 2.16 Single-collector efficiency as a function of effective Stokes number obtained from DNS-LPT simulations for a range of mean slip Reynolds number and volume fractions.

efficiency data does not collapse well with the effective Stokes number. This is because the effective Stokes number does not capture the dependence of single-collector efficiency on mean flow Reynolds for different granule volume fraction. By modifying the power of the $Re_m$ in effective Stokes number from $1/2$ to $1/5$, the modified effective Stokes number gave a good collapse of DNS-LPT data as can be seen in Fig. 2.17. We reduced the power of $Re_m$ in effective Stokes number because in Section 2.4.1 we have seen that for $Re_m > 10$ the single-collector efficiency tends to asymptote to a limiting high $Re_m$ value. The reduced power of $Re_m$ in effective Stokes number capture this single-collector dependence on $Re_m$.

$$St^*_{\text{eff}} = \left[ A(\epsilon_s) + 1.14 Re_m^{1/5} \left(1 - \epsilon_s\right)^{-3/2} \right] \frac{St}{2}, \tag{2.32}$$

The particles that do not get filtered by the granules penetrate through the bed and

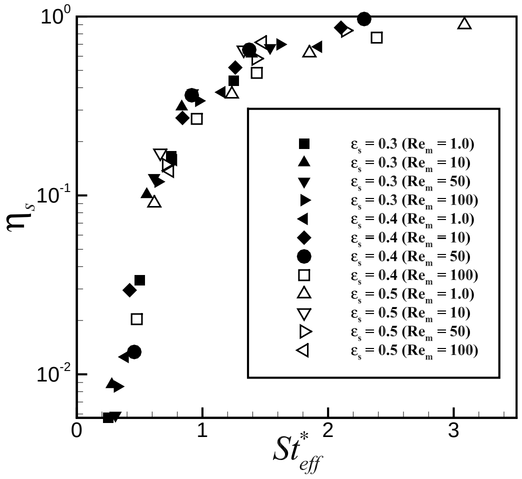

Figure 2.17 Single-collector efficiency as a function of modified effective Stokes number obtained from DNS–LPT simulations for a range of mean slip Reynolds number and volume fractions with modified effective Stokes number.

the penetration of a granular bed is defined as

$$P = 1 - \eta, \tag{2.33}$$

where $\eta$ is the filtration efficiency of a granular bed. In a granular bed, the filtration of a particles is a strong function of Stokes number $St$, and for a particular granule volume fraction $\epsilon_s$ and mean slip Reynolds number $Re_m$. Fig. 2.18 shows that for a given particle Stokes number, the penetration decreases with increase in the length of granular bed ($P = f(L; St = St^*)$). This is due to the increase in probability of particles being filtered by the granules with increase in the length of the granular bed. The data in Fig. 2.18 suggests an exponential dependence for the penetration of the particles in a bed with bed length :

$$\lambda = -\frac{1}{L}\ln P. \tag{2.34}$$

Hence a new correlation model can be proposed for the filter coefficient $\lambda$ using DNS–

LPT data, where $\lambda = f(Re_m, St, \epsilon_s) = f(St^*_{\text{eff}})$. The new correlation for filter coefficient is proposed from DNS–LPT data reads as

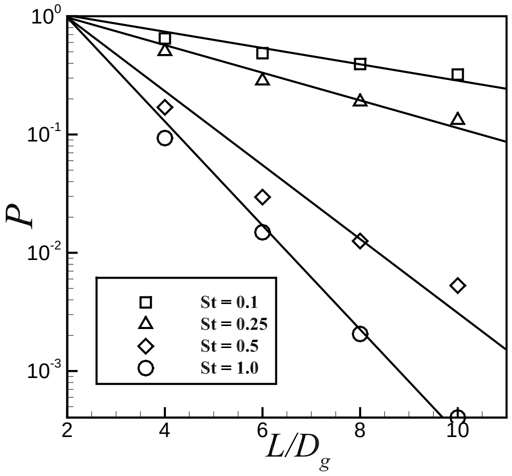

Figure 2.18 Penetration obtained from DNS-LPT simulations with the length of granular bed, at different particle Stokes number for a granule volume fraction $\epsilon_s = 0.4$ and a mean slip Reynolds number $Re_m = 20$.

$$\lambda = \frac{{St^*_{\text{eff}}}^{3.2}}{4.3 + {St^*_{\text{eff}}}^{3.2}}. \tag{2.35}$$

Figure 2.19 shows the new correlation for filter coefficient that is a best fit to the DNS–LPT data which can be used in CFD simulations and a summary of the simulation conditions used to obtain the DNS–LPT data points in Fig. 2.19 are shown in Table 5.1.

## 2.6 Conclusions

We use DNS–LPT to quantify the performance of a granular filter and to investigate the dependence of global filtration quantities such as penetration and single-collector efficiency on granule volume fraction $\epsilon_s$, mean slip Reynolds number $Re_m$, and particle

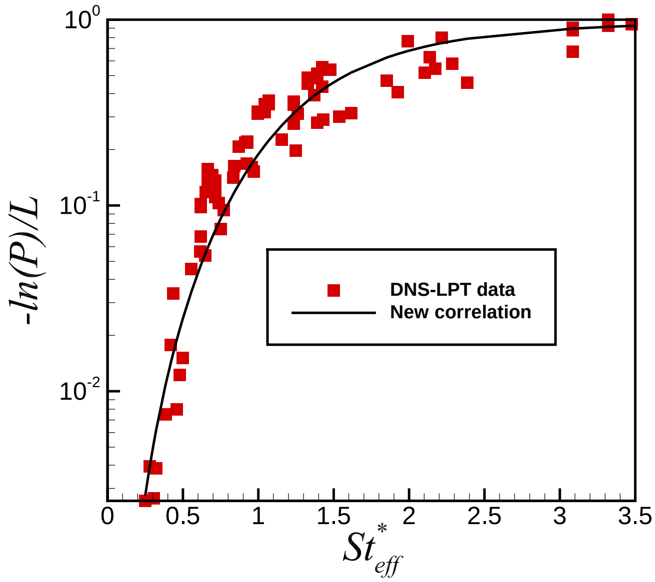

Figure 2.19 The DNS-LPT data for filter coefficient $\lambda$ for different bed lengths and the solid line is the best fit correlation to DNS-LPT data.

Stokes number $St$ for filtration of inertial particles. The penetration of fine particles in a granular filter is usually defined as the outlet particle concentration (or number density) normalized by its inlet value on the basis of the concentration equation for particles with negligible inertia. For inertial particles we show that the penetration in a granular filter is the outlet particle flux normalized by its inlet value, which reduces to the normalized concentration (or number density) for particles of negligible inertia. This definition of penetration is consistent with the mass balance of particles in a granular filter at steady state. For particles with finite inertia, the DNS–LPT results show that there is significant nonzero mean slip between particles and fluid, which explains the difference between particle flux and concentration profiles.

The DNS–LPT results show that the single-collector efficiency depends on $\epsilon_s$, $St$, and mean slip Reynolds number for $Re_m \leq 10$, but, for $Re_m > 10$ the single–collector

Table 2.1 Granular filtration parameters for DNS-LPT filter coefficient.

| **Parameters** | **Values simulated** |
|---|---|
| $\epsilon_s$ | 0.3, 0.4, 0.5 |
| $Re_m$ | 1, 10, 20, 30, 50, 100 |
| $St$ | 0.05, 0.10, 0.15, 0.25 |
| ${}^{L}\!/_{D_g}$ | 4, 5, 6, 8, 10 |

efficiency is practically independent of mean slip Reynolds number. This dependence of single-collector efficiency on mean slip Reynolds number is explained on the basis of tortuosity of fluid streamlines and the residence time of particles in the granular bed. Although tortuosity of fluid streamlines increases with $Re_m$ which aids in filtration of particles, the decrease in residence time of particles in granular filter with $Re_m$ offsets the effect of tortuosity for $Re_m > 10$.

The effective Stokes number proposed by D'Ottavio and Goren (1983) to collapse single-collector efficiency data for moderate mean slip Reynolds number is modified to reflect the weak dependence of single-collector efficiency on mean flow Reynolds number for $Re_m > 10$ by changing the $Re_m^{1/2}$ dependence to $Re_m^{1/5}$. The single-collector efficiency obtained from DNS–LPT when plotted against the modified effective Stokes number gives a very good collapse over the range of granule volume fraction, mean slip Reynolds number and particle Stokes number simulated.

We also found from DNS–LPT data that the penetration decays exponentially with the length of the granular bed. Based on this observation a model is proposed for the filter coefficient $\lambda$ in terms of the modified effective Stokes number. The model for filter coefficient proposed in this study can be used in two–fluid CFD simulations of a full-scale granular bed to model the filtration of particle by the granular bed.

# CHAPTER 3. Filtration model for polydisperse particulates in gas-solid flow using particle-resolved direct numerical simulation

This chapter is a manuscript in preparation for Aerosol science and technology titled : Filtration model for polydisperse particulates in gas-solid flow using particle-resolved direct numerical simulation authored by R. Kolakaluri,E. Murphy, R. C. Brown, R. O. Fox and S. Subramaniam.

## Abstract

An analytical framework for calculating the filtration efficiency of polydisperse particles in a granular bed is developed for cases where inertial impaction and interception are the principal filtration mechanisms. This framework is used to develop a model for the polydisperse single-collector efficiency from monodisperse single-collector efficiency correlations. Conceptually, the polydisperse model is developed by transforming the probability density of particle radius into a probability density of particle Stokes number that is then used to weight the monodisperse single-collector efficiency at a given Stokes number. In Stokes flow, the polydisperse model uses a monodisperse (single-collector efficiency) correlation (Araújo et al., 2006) obtained from unit cell numerical simulations. For moderate Reynolds number, the polydisperse model uses an empirical monodisperse correlation obtained from experimental data of D'Ottavio and Goren (1983). An extension of this polydisperse filtration concept results in an analytical so-

lution for the axial variation of polydisperse particle flux in a random three-dimensional (3D) granule configuration. In order to verify the analytical results for polydisperse particle filtration over a range of mean slip Reynolds number, a particle–resolved Direct Numerical Simulation (DNS) approach is coupled with Lagrangian Particle Tracking (LPT) to simulate filtration of polydisperse particles in a granular bed. The DNS–LPT approach is validated with results for penetration and single-collector efficiency in the literature (D'Ottavio and Goren, 1983). The DNS–LPT results are then used to verify analytical predictions of the cumulative distribution function (CDF) of particle radius and the polydisperse particle flux. The particle size distributions used in this study are similar to those typically encountered in granular filtration applications. Therefore, the analytical models for polydisperse filtration that are developed in this study can directly be applied to practical granular filtration applications in chemical looping combustion, thermal power plants and water filtration.

## 3.1 Introduction

Granular filtration is a process commonly used to remove particles from fluid streams. It finds applications in filtration of fly ash from hot gases produced during fast pyrolysis of biomass for bio-oil production (El-Hedok et al., 2011; Ritzert et al., 2004), water and wastewater treatment (Davis, 2010), and exhaust gas treatment in thermal power plants. Filtration of particles in these applications is receiving increased attention that is driven by various factors, such as the need for clean coal combustion, treating water pollution, and efforts to reduce risks to human health from exposure to aerosols.

The principal mechanisms for particle filtration from fluid streams flowing through a granular bed are inertial impaction, interception, gravitation, and Brownian diffusion (Tien and Ramarao, 2007). Inertial impaction and interception are significant mechanisms for particle collection in granular filtration for particles with diameters greater than $1\mu$m and the particles considered in this study fall in this category. Granular filtration in the inertial impaction and interception regimes is a strong function of particle inertia that is characterized by the Stokes number $St = \langle W \rangle d_p^2 \rho_p / 9 D_g \mu$ (D'Ottavio and Goren, 1983; Tien and Ramarao, 2007; Araújo et al., 2006). The Stokes number is the ratio of the particle momentum response time to a characteristic fluid time scale. The characteristic fluid time scale is taken to be $D_g/2 \langle W \rangle$, where $\langle W \rangle$ is the mean slip velocity between fluid and granules, and $D_g$ is the granule diameter. Note that it is the mean slip velocity between fluid and *granules* (not particles) that determines the scale of fluid motions. The particle momentum response time is $\tau_p = d_p^2 \rho_p / 18\mu$, where $d_p$ is the diameter of the particle, $\rho_p$ is the density of the particle, and $\mu$ is the dynamic viscosity of the fluid.

The particles or aerosols found in the applications mentioned above are generally polydisperse. Furthermore, the process of filtration changes the local size distribution of particles at different spatial locations within the granular bed. Polydispersity implies a range of particle Stokes numbers because of the $d_p^2$ dependence of the particle response time $\tau_p$ on diameter. Particles with different Stokes number filter at different rates through a granular bed. In this study, we develop analytical models for polydisperse particle filtration that are valid in both Stokes flow and at moderate mean slip Reynolds number. The mean slip Reynolds number is defined as $Re_m = (1 - \epsilon_s) \langle W \rangle D_g \rho_f / \mu$, where $\epsilon_s$ is the granule volume fraction, and $\rho_f$ is the fluid density. Note that the mean slip Reynolds number affects the particle Stokes number, which can be written as

$$St = \frac{Re_m}{(1 - \epsilon_s)} \left( \frac{d_p}{D_g} \right)^2 \frac{1}{9} \frac{\rho_p}{\rho_f}. \tag{3.1}$$

The development of analytical polydisperse filtration models for moderate mean slip Reynolds number is one of the principal contributions of this work.

Due to the complex geometry of a granular bed, simple models have been developed to explain filtration. The assumption made in these models is that a granular bed can be represented as a sequence of single collectors, and the filter efficiency of each single collector is called the single-collector efficiency $\eta_s$. In this approach (Tien and Ramarao, 2007), the single-collector efficiency describes the rate of particle collection as the fraction of particles flowing through an area equal to the projected area of the collector in a plane normal to the direction of the flow. The single-collector efficiency $\eta_s$ for a granular bed is related to the penetration $P = \dot{m}_{out}/\dot{m}_{in}$ by the relation:

$$\eta_s = \frac{-2 D_G \ln P}{3 \epsilon_s L}, \tag{3.2}$$

where $\dot{m}_{in}$ is the mass of particles injected at the inlet and $\dot{m}_{out}$ is mass of particles exited from the outlet of the granular bed, $D_g$ is the granule diameter, and $L$ denotes the length of the granular bed. Over the past few decades many researchers have proposed empirical correlations (Thambimuthu, 1980; D'Ottavio and Goren, 1983; Gal et al., 1985; Jung et al., 1989) for single-collector efficiency of monodisperse particles based on experimental data. Yoshida and Tien (1985); Pendse and Tien (1982) also developed correlations for the single-collector efficiency, but unlike others, their correlations are obtained using both numerical and experimental results.

For filtration of monodisperse particles in Stokes flow ($Re_m = 0$) through a monodisperse granular bed, the single-collector efficiency $\eta_s$ depends only on granule volume fraction $\epsilon_s$ and particle Stokes number $St$ (Araújo et al., 2006). For finite mean-slip Reynolds number, the filtration of particles $\eta_s$ is a function of Stokes number $St$, granule volume fraction $\epsilon_s$, and the mean slip Reynolds number $Re_m$. In an attempt to collapse single-collector efficiency data for moderate Reynolds number, D'Ottavio and Goren (1983) combined the three independent dimensionless groups $Re_m$, $St$ and $\epsilon_s$ into a single effective Stokes number $St_{\text{eff}}$ as given in Eqs. 4.12 and 4.13. Most of the correlations for single-collector efficiency found in the granular filtration literature are given as a function of Stokes number $St$, or a combination of both Stokes number $St$ and mean slip Reynolds number $Re_m$, or as a function of effective Stokes number $St_{\text{eff}}$.

These correlations are for monodisperse particles.

There are few experimental studies on granular filtration of polydisperse particles due to difficulties in tracking the filtration rate of each particle size class through the granular bed, and also due to the lack of optical access inside the granular bed. Jung and Tien (1992); Wu and Tien (1995) were able to experimentally study the granular filtration of polydispersed particles. However, they did not look at different size distributions of particles. Kim et al. (2000) and Kwon et al. (2002) analytically calculated the filtration efficiency of a log-normal size distribution of particles where Brownian diffusion was considered as the deposition mechanism. Their study does not discuss other size distributions and also the model is limited to Stokes flow. An analytical solution was derived by Song and Park (2006) for filtration efficiency of polydisperse aerosols, where both diffusional and inertial impaction are considered as deposition mechanisms for a log-normal size distribution. Their study is also limited to Stokes flow. All the analytical studies mentioned above are restricted to a log-normal distribution of particle diameter. Hence, there is a need for an analytical framework in the inertial impaction regime that is not restricted to a particular size distribution of particles, and which is valid in both Stokes flow and at moderate Reynolds number.

The objectives of this work are to develop an analytical framework for polydisperse particle filtration due to inertial impaction and interception that is valid for any size distribution of particles. Another objective is to develop models that are valid in both Stokes flow as well as in moderate Reynolds number flows. In order to verify the analytical model's predictions of polydisperse filtration, a DNS–LPT approach is developed to study the filtration of polydisperse particles in a granular bed.

The chapter is organized as follows. The analytical model development for Stokes flow and moderate Reynolds number flow and the closure models are discussed in Section 3.2. In Section 3.3 the DNS–LPT computational approach that is used to simulate the filtration of particles in a granular bed is described. In Section 3.4 we demonstrate convergence of the DNS–LPT approach and validate the simulation results by comparing with experimental data. Finally, in Section 3.5 the analytical predictions for Stokes flow and moderate Reynolds number flow are compared with the DNS–LPT results.

## 3.2 Analytical model development

We have seen from various experimental (D'Ottavio and Goren, 1983; Gal et al., 1985; Tien and Ramarao, 2007) and numerical studies (Araújo et al., 2006) that the single-collector efficiency for monodisperse particles $\eta_{s,mono}$ is a function of $\epsilon_s$, $Re_m$ and $St$, such that $\eta_{s,mono}(\epsilon_s, Re_m, St)$. Therefore, the challenge in developing a model for polydisperse particle filtration is to come up with an expression for $\eta_{s,poly}(\epsilon_s, Re_m, f(r_p))$. The analytical model is first developed for Stokes flow and then extended to moderate Reynolds number flows. It is applied to Stokes flow in a 2D ordered array and then to flows at finite Reynolds number in a 3D assembly of randomly distributed granules that represents a granular bed.

### 3.2.1 Polydisperse single-collector efficiency in Stokes flow

The principal effect of polydispersity on granular filtration is that the polydisperse single-collector efficiency $\eta_{s,poly}(\epsilon_s, Re_m, f(r_p))$ must account for a range of Stokes number, because the particle size distribution implies a distribution of Stokes number. For the case of Stokes flow ($Re_m \approx 0$), this dependence can be accounted for by transforming the probability distribution function (PDF) for the particle radius $f\left(r_p\right)$ into a PDF for the particle Stokes number $f\left(St\right)$ by a simple change of variable:

$$f\left(St\right) = f\left(r_p\right)\frac{dr_p}{dSt}. \tag{3.3}$$

The PDF of particle Stokes number is used to find the polydisperse single-collector efficiency $\eta_{s,poly}$, which is now expressed as $\eta_{s,poly}(\epsilon_s, f(St))$, where the dependence on

$Re_m$ can be omitted for Stokes flow. The functional dependence of the monodisperse single-collector efficiency $\eta_{s,mono}$ on Stokes number can be interpreted as the expected polydisperse single-collector efficiency conditional on a particular Stokes number :

$$\eta_{s,mono}(\epsilon_s, St) = \langle \eta_{s,poly} | \epsilon_s, St \rangle \, . \tag{3.4}$$

Therefore, the cumulative polydisperse single-collector efficiency is simply

$$\eta^{cum}_{s,poly}(\epsilon_s, St) = \int_{St_c(\epsilon_s)}^{St} \left\langle \eta_{s,poly} \mid \epsilon_s, St^{'} \right\rangle f(St^{'}) dSt^{'}, \tag{3.5}$$

where $St_c$ is the critical Stokes number above which the filtration of particles starts to take place in the absence of gravity (Araújo et al., 2006). The effect of interception parameter is not considered in the Araújo et al. (2006) study, hence the critical Stokes number $St_c$ is only a function of granule volume fraction $\epsilon_s$. The cumulative polydisperse single-collector efficiency $\eta^{cum}_{s,poly}(\epsilon_s, St)$ represents the filtration efficiency of all particles with $St^{'} < St$. The expected polydisperse single-collector efficiency is $\langle \eta_{s,poly} \rangle = \eta^{cum}_{s,poly}(\infty)$, and is referred to as the total polydisperse efficiency for simplicity. The integral in Eq. 3.5 is evaluated using fourth-order Runge-Kutta integration.

### 3.2.2 Results for Stokes flow

Particle filtration in an infinite ordered filter composed of a periodic arrangement of circular obstacles is a classical problem. This approach has been used to describe the porous geometry of fibrous filters (Marshall et al., 1994) and also a homogeneous randomly packed medium (Tien and Ramarao, 2007). Araújo et al. (2006) used Marshall et al. (1994) solution of flow past a circular obstacle in a square unit cell for periodic boundary conditions imposed on the fluid in both $x$ and $y$ direction to simulate filtration of monodisperse particles. Araújo et al. (2006) expressed the single-collector efficiency as a function of particle Stokes number $St$ by

$$\eta_{s,mono} \propto (St - St_c)^{0.5}. \tag{3.6}$$

The critical Stokes number $St_c$ is shown to vary with granule volume fraction $\epsilon_s$, where $1 - \epsilon_s$ is the unit cell porosity. The correlation given by Araújo et al. (2006) exceeds unity for Stokes number greater than 1.2, which is unphysical. In order to remedy this behavior we propose a modified correlation to Araujo's data for $\eta_{s,mono}$ for a granule volume fraction $\epsilon_s$ of 0.1:

$$\eta_{s,mono} = \frac{(St - St_c)}{(St - St_c) + a}, \tag{3.7}$$

where $a = 0.31$ and $St_c = 0.21(\epsilon_s = 0.1)$. Figure 3.1 shows both the modified correlation and original correlation along with the numerical data from Araújo et al. (2006). It is observed that the modified correlation fits the data more closely and obeys the correct limiting behavior($\eta_s \to 1$).

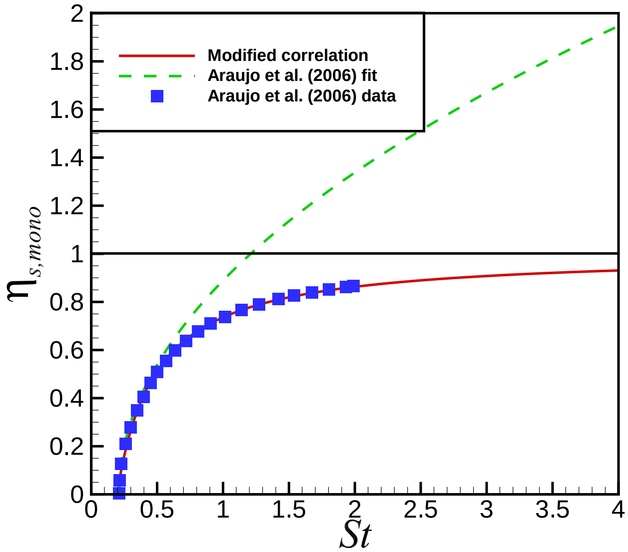

Figure 3.1 The Araújo et al. (2006) correlation and the modified correlation compared with simulation data from Araújo et al. (2006) ($\epsilon_s = 0.1$).

The analytical model prediction (Eqs. 3.5 and 3.7) are tested for different size distributions, and compared with Lagrangian particle tracking (LPT) results in Section 3.5.1.

The mean particle radius in this test case is chosen in such a way as to maintain the mean Stokes number ($St(\langle r_p \rangle) = 0.5$) and particle density ($\rho_p = 1000$) close to values found in experiments (El-Hedok et al., 2011). The parameters that define the test case are given in Tables 3.1(a) and 3.1(b).

Table 3.1 Parameters corresponding to the test case for polydisperse filtration in Stokes flow.

(a) Physical

| **Parameter** | **Value** |
|---|---|
| $\langle r_p \rangle$ | $7.6 \times 10^{-2}$m |
| $D_g(\epsilon_s = 0.1)$ | 0.357m |
| stdev$(r_p)/0.5D_g$ | $1.52 \times 10^{-2}$m |

(b) Nondimensional

| **Parameter** | **Value** |
|---|---|
| $Re_m$ | 0.1 |
| $\epsilon_s$ | 0.1 |
| $St(\langle r_p \rangle)$ | 0.5 |

The PDFs of particle radius $r_p$ for three size distributions — normal, log-normal, and gamma — that are used to test the cumulative polydisperse single-collector efficiency are shown in Fig. 3.2(a). The corresponding PDF of particle Stokes number obtained using Eq. 3.3 is shown in Fig. 3.2(b). The shape of these distributions affect the cumulative polydispere single-collector efficiency computed using Eq. 3.5. Note that the particles in these distributions with $St < St_c$ do not filter and the critical Stokes number is marked in Fig. 3.2(b).

The cumulative polydisperse single-collector efficiency is computed using Eqs. 3.4–3.5 and the expression for $\eta_{s,mono}$ (Eq. 3.7). The cumulative polydisperse single-collector efficiency for the three size distributions is shown in Fig. 3.3. For comparison the monodisperse single-collector efficiency at the mean particle radius is also shown. The monodisperse single-collector efficiency at the mean particle size is higher than the polydisperse single-collector efficiencies because particles with $St < St_c$ do not filter out (cf. Eqs. 3.6 - 3.7) in all three distributions. The polydisperse single-collector efficiency for the normal distribution is slightly less than the single-collector efficiency of the other two distributions because the peak of the normal distribution is less than that of the

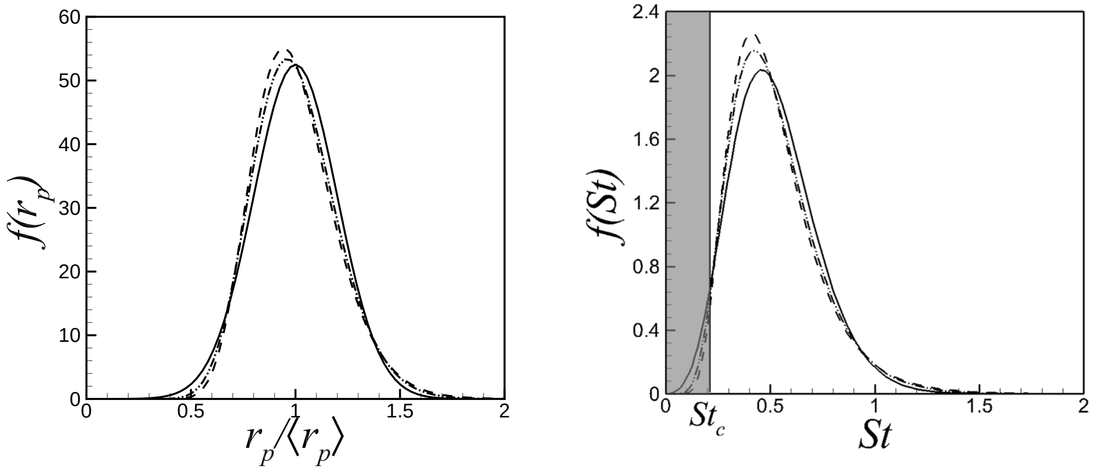

(a)

(b)

Figure 3.2 (a) PDF of particle radius for three different distributions with a normalized mean particle radius of 0.22 and normalized standard deviation of $1.52 \times 10^{-2}$, both lengths are normalized by $D_g/2$. (b) Corresponding PDF's of particle Stokes number for the same distributions with a mean Stokes number of 0.50 based on mean particle radius.(normal — ; log-normal - - - ; gamma — ·· — ··).

log-normal and gamma distributions, whereas the standard deviation is the same for all three distributions (see Fig. 3.2(a)). In Section 3.5.1, the results from this analytical model are compared with 2D LPT results.

### 3.2.3 Polydisperse single-collector efficiency in moderate Reynolds number flow

We now extend the analytical model for polydisperse single-collector efficiency to moderate mean slip Reynolds number. Recall that the experimental data (D'Ottavio and Goren, 1983) on single-collector efficiency in moderate Reynolds number flow collapses when plotted as a function of the effective Stokes number. The empirical correlation for single-collector efficiency from the experimental data of D'Ottavio and Goren (1983) is

$$\eta_{s,mono}(\epsilon_s, Re_m) = \left( \frac{St_{\text{eff}}^{3.55}}{St_{\text{eff}}^{3.55} + 1.67} \right). \tag{3.8}$$

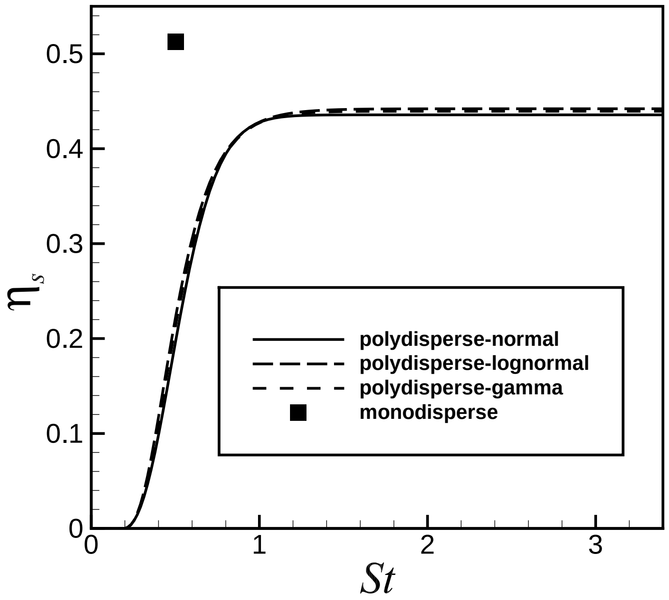

Figure 3.3 The single-collector efficiency obtained from three different distributions for a normalized standard deviation of $1.52 \times 10^{-2}$ and a normalized mean particle radius of 0.22 compared with monodisperse single-collector efficiency for the same mean (mean Stokes number = 0.50), both lengths are normalized by $D_g/2$

This motivates the development of a polydisperse single-collector efficiency of the form $\eta_{s,poly}(\epsilon_s, Re_m, f(St_{\text{eff}}))$. Therefore, the PDF of particle radius is transformed into the PDF of effective Stokes number as

$$f\left(St_{\text{eff}}\right) = f\left(r_p\right) \frac{dr_p}{dSt_{\text{eff}}}. \tag{3.9}$$

The expression for monodisperse single-collector efficiency in moderate Reynolds number flow (given by Eq. 3.8) is used to obtain the polydisperse filtration efficiency. The cumulative polydisperse single-collector efficiency is

$$\eta^{cum}_{s,poly}(\epsilon_s, Re_m, St_{\text{eff}}) = \int_0^{St_{\text{eff}}} \left\langle \eta_{s,poly} | St'_{\text{eff}} \right\rangle f(St'_{\text{eff}}) dSt'_{\text{eff}}. \tag{3.10}$$

### 3.2.4 Results for moderate Reynolds number flow

The PDFs of particle radius $r_p$ and particle effective Stokes number $St_{\text{eff}}$ for three size distributions — normal, log-normal, and gamma — that are used to test the cumulative polydisperse single-collector efficiency are shown in Figs. 3.4(a) and 3.4(b). The trends are similar to that observed in the Stokes flow case. The shape of the distributions affect the polydisperse single-collector efficiency. The parameters of the size distributions for the moderate Reynolds number test case are given in Table 3.2(a). The two test cases chosen are based on the experimental data of D'Ottavio and Goren (1983). Test case A with an effective Stokes number $St_{\text{eff}} = 0.72$ falls in the lower efficiency region (Fig. 3.9) and test case B with an effective Stokes number $St_{\text{eff}} = 1.12$ falls in the high efficiency region (Fig. 3.9). We also maintained the other parameters like particle density, mean Reynolds number, and granule volume fraction close to experiments (D'Ottavio and Goren, 1983). The cumulative polydisperse single-collector efficiency obtained from all the three distributions are shown in Fig. 3.5. For comparison the monodisperse single-collector efficiency at the mean particle radius is also plotted in Fig. 3.5. In this moderate Reynolds number case with $Re_m = 10$, the total polydisperse single-collector efficiency is higher than the monodisperse value at the mean particle radius because the

Table 3.2 Parameters corresponding to the experiments and the test cases for polydisperse filtration in moderate Reynolds number.

(a) Experiments

| **Parameter** | **Value** |
|---|---|
| $D_g$ | $2 \times 10^{-3}$m; $4 \times 10^{-3}$m |
| $\langle r_p \rangle$ | $3.0 \times 10^{-7}$m to $2.25 \times 10^{-6}$m |
| $N_R = 2r_p/D_g$ | $1.5 \times 10^{-4}$ to $2.3 \times 10^{-3}$ |

(b) Test cases

| **Parameter** | **Test case A** | **Test case B** |
|---|---|---|
| $\langle r_p \rangle / D_g$ | $3.0 \times 10^{-3}$ | $3.75 \times 10^{-3}$ |
| $N_R = 2r_p/D_g$ | $6.0 \times 10^{-3}$ | $7.5 \times 10^{-3}$ |
| $\text{stdev}(r_p)/D_g$ | $6.0 \times 10^{-4}$ | $7.5 \times 10^{-4}$ |

Table 3.3 Nondimensional parameters corresponding to experiments and the test cases for polydisperse filtration in moderate Reynolds number flow.

| | **Experiments** | **Test case A** | **Test case B** |
|---|---|---|---|
| $Re_m$ | 10 to 1000 | 10 | 10 |
| $\epsilon_s$ | 0.63 | 0.5 | 0.5 |
| $St$ | $8.6 \times 10^{-4}$ to 0.18 | 0.05 | 0.078 |
| $St_{\text{eff}}$ | 0.15 to 2.0 | 0.72 | 1.12 |

particles with $St_{\text{eff}} > \langle St_{\text{eff}} \rangle$ contribute to this increase. Since the shapes of $f(St_{\text{eff}})$ for $St_{\text{eff}} > \langle St_{\text{eff}} \rangle$ are very similar for all three distributions (see Fig. 3.4(b)), this increase is very similar for all the three distributions considered.

In this section, we have developed an analytical model for calculating the polydisperse single-collector efficiency for different size distributions of particles in both Stokes and moderate Reynolds number flow. We find that the monodisperse single-collector efficiency at the mean particle radius is not a good estimate of total filtration efficiency since it can over or underpredict the total polydisperse single-collector efficiency depending on the flow conditions. However, the analytical models developed in this section do not provide information regarding the axial variation of particle flux along the granular bed. To find the axial variation of polydisperse particles along the granular bed, we derive an analytical expression for the axial variation of particle flux.

### 3.2.5 Transport equation for the particle flux

The evolution of number density $n(\mathbf{x}, r, t)$ of particles through the granular bed is governed by

$$\frac{\partial n(\mathbf{x}, r, t)}{\partial t} + \frac{\partial}{\partial x_k}(\langle V_k | r \rangle \, n(\mathbf{x}, r, t)) = S(\mathbf{x}, r, t). \tag{3.11}$$

Details of the derivation of the evolution of number density of particles can be found in C. If the sink term due to granular filtration is proportional to the local particle flux at that

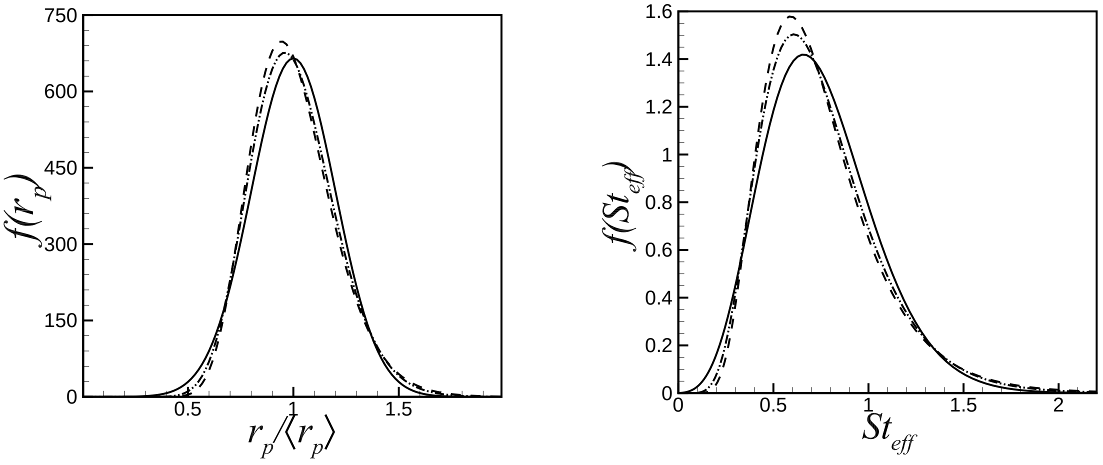

(a)

(b)

Figure 3.4 (a) PDF of particle radius for three different distributions with a normalized mean particle radius of $3 \times 10^{-3}$ and a normalized standard deviation of $6 \times 10^{-4}$, both lengths are normalized by $D_g$. (b)Corresponding PDF's of particle effective Stokes number for the same distributions with a mean effective Stokes number of $St_{\text{eff}} = 0.72$ based on normalized mean particle radius, granule volume fraction $\epsilon_s = 0.5$ and mean slip Reynolds number $Re_m = 10$ (normal — ; log-normal - - - ; gamma — ·· — ··).

location, then the axial variation of particle flux in a granular bed can be analytically obtained by solving Eq. 3.12 with a model for the sink term $S = -\lambda(St_{\text{eff}})\langle V_k|r\rangle n(\mathbf{x}, r, t)$. The resulting number density equation is

$$\frac{\partial n(\mathbf{x}, r, t)}{\partial t} + \frac{\partial}{\partial x_k}\left(\langle V_k|r\rangle n(\mathbf{x}, r, t)\right) = -\lambda(St_{\text{eff}})\,\langle V_k|r\rangle\, n(\mathbf{x}, r, t), \qquad (3.12)$$

where $\lambda$ is the filter coefficient. D'Ottavio and Goren (1983) proposed the following correlation for the filter coefficient:

$$\lambda(St_{\text{eff}}) = 3\eta_{s,mono}(St_{\text{eff}})\,(1 - \varepsilon_s)\,/2D_g, \qquad (3.13)$$

where $\eta_{s,mono}$ is the monodisperse single-collector efficiency, whose dependence on $St_{\text{eff}}$ is given by Eq. 3.8 that correlates a wide range of experimental data. At steady state,

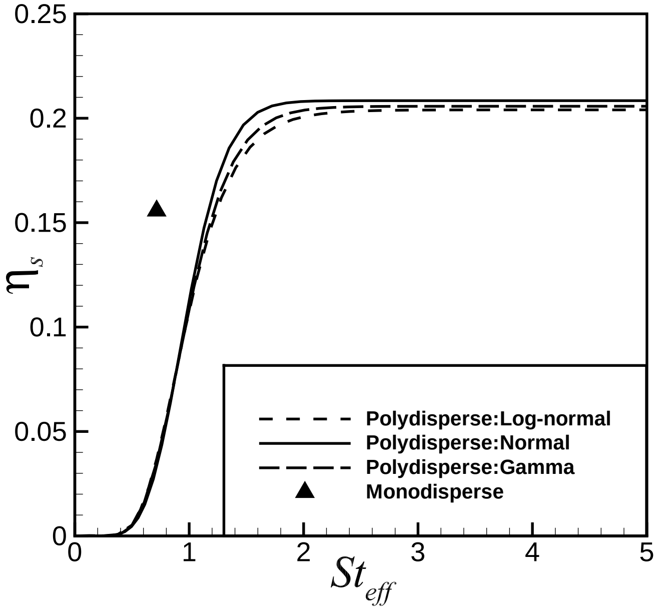

Figure 3.5 The single-collector efficiency obtained from three different distributions for a normalized standard deviation of $6.0 \times 10^{-4}$ and a normalized mean particle radius of $3.0 \times 10^{-3}$ compared with monodisperse single-collector efficiency for the same mean particle radius (mean effective Stokes number $St_{\text{eff}} = 0.72$ based on mean particle radius, granule volume fraction $\epsilon_s = 0.5$ and mean slip Reynolds number $Re_m = 10$), both lengths are normalized by $D_g$.

Eq. 3.12 simplifies to read

$$\frac{\partial}{\partial x_k} \left( \langle V_k | r \rangle \, n(\mathbf{x}, r) \right) = -\lambda \left( St_{\text{eff}} \right) \langle V_k | r \rangle \, n(\mathbf{x}, r). \tag{3.14}$$

Rewriting Eq. 3.14 in terms of the particle flux in the granular bed $J_k(\mathbf{x}, r) = \langle V_k | r \rangle \, n(\mathbf{x}, r)$, results in

$$\frac{\partial}{\partial x_k} \left( J_k(\mathbf{x}, r) \right) = -\lambda \left( St_{\text{eff}} \right) J_k(\mathbf{x}, r). \tag{3.15}$$

Noting that in granular filtration the particle flux varies only in the axial coordinate ($J(\mathbf{x}, r) = J(x, r)$) because the problem is statistically homogeneous in $y$ and $z$ directions, and integrating Eq. 3.15 along the length of the granular bed result in:

$$\frac{J(x,r)}{J(0,r)} = \exp\left[-\lambda\left(St_{\text{eff}}\right)x\right] \tag{3.16}$$

The axial variation of particle flux $J(x,r)$ can be written in terms of the particle size distribution conditional on axial location $x$, as $J(x,r) = J(x)f(r|x)$, where $J(x)$ is the total particle flux and $f(r|x)$ is the PDF of particle radius conditional on axial location. The total particle flux $J(x)$ at a given axial location $x$ is obtained by integrating over all particle size values

$$J(x) = \int_0^\infty J(x,r)dr = \int_0^\infty J(x)f(r|x)dr. \tag{3.17}$$

The PDF of particle radius is not assumed to be the same at all axial locations, but it changes with $x$ as particles filter through the bed. The particle flux equation (Eq. 3.16) can be deduced using Eq. 3.17:

$$J(x) = \int_0^\infty J(0,r)\exp\left[-\lambda\left(St_{\text{eff}}\right)x\right]dr \tag{3.18}$$

Equation 3.18 can be further simplified, additionally, a change of variables is made from $r$ to $St_{\text{eff}}$ to obtain the normalized particle flux :

$$\frac{J(x)}{J(0)} = \int_0^\infty f(St_{\text{eff}}|x=0)\exp\left[-\lambda\left(St_{\text{eff}}\right)x\right]dSt_{\text{eff}} \tag{3.19}$$

The results of the normalized particle flux obtained from Eq 3.19 are compared with DNS-LPT results in Sec. 3.5. We now briefly describe the DNS-LPT simulations.

## 3.3 Direct numerical simulation of granular filtration

In granular filtration there are two solid phases: one comprises the granules through which the fluid flows, and the other solid phase consists of particles that are suspended in the fluid phase. The three-dimensional fluid phase flow fields around the granules are obtained using a particle-resolved DNS methodology called Particle-resolved Uncontaminated-fluid Reconcilable Immersed Boundary Method (PUReIBM)(see Fig. 3.6).

In PUReIBM, exact no-slip and no-penetration boundary conditions are imposed at the granule-fluid interface. The governing equations solved in PUReIBM are

$$\frac{\partial u_i}{\partial x_i} = 0, \tag{3.20}$$

and

$$\rho_f \frac{\partial u_i}{\partial t} + \rho_f S_i = -g_{IBM,i} + \mu \frac{\partial^2 u_i}{\partial x_j \partial x_j} + f_{u,i}, \tag{3.21}$$

where $g_{IBM,i}$ is the pressure gradient, $S_i$ is the convective term, $f_{u,i}$ is the immersed boundary force term that accounts for the granules in the fluid phase. Further details on the PUReIBM solution approach are given in D. PUReIBM is a numerically convergent and accurate particle-resolved DNS method for fluid-solid flows, and it has been extensively validated in a comprehensive suite of test cases (Tenneti et al., 2011). In the DNS-LPT approach developed here, the particles to be filtered are tracked as point particles in a Lagrangian frame as they are carried by the fluid phase through the granular bed.

The dispersed phase consisting of particles is represented in a Lagrangian frame at time $t$ by $\{\mathbf{X}^{(i)}(t), \mathbf{V}^{(i)}(t), i = 1, ......, N_p(t)\}$, where $\mathbf{V}^{(i)}(t)$ denotes the $i$th particle velocity and $\mathbf{X}^{(i)}(t)$ represents its position. The position and velocity of the particles evolve by

$$\frac{d\mathbf{X}^{(i)}(t)}{dt} = \mathbf{V}^{(i)}, \tag{3.22}$$

and

$$\frac{d\mathbf{V}^{(i)}(t)}{dt} = \frac{\mathbf{f}^{(i)}}{m_p^{(i)}} = \mathbf{A}^{(i)}, \tag{3.23}$$

where $m_p^{(i)}$ is the mass and $\mathbf{f}^{(i)}$, and $\mathbf{A}^{(i)}$ are the instantaneous force and acceleration experienced by the $i$th particle. The instantaneous force is modeled using the drag correlation by Schiller and Naumann (1933) :

$$\mathbf{f}^{(i)}(t) = 3\pi\mu \left|\mathbf{u}(\mathbf{X}^{(i)}(t), t) - \mathbf{V}^{(i)}\right| d_p(1 + 0.15 Re_p^{0.687}), \tag{3.24}$$

where $Re_p$ is the particle Reynolds number based on slip velocity between the fluid and particle (not granule), $\rho_f$, $\mu_f$ and $\mathbf{u}(\mathbf{X}^{(i)}(t), t)$ are the fluid phase density, kinematic viscosity and the velocity of the fluid at the particle location, respectively. Inter-particle interactions are neglected consistent with our assumption in the analytical model for particle flux evolution. In the present study, the mass loading ($\approx 3 \times 10^{-2}$) of the dispersed phase is assumed to be negligible, and so momentum exchange between the particles and fluid is neglected (The total particle drag is around $\approx 5 \times 10^{-2}$ that of the total granule drag for mean slip Reynolds number $Re_m = 10$ and granule volume fraction $\epsilon_s = 0.5$).

The fluid velocity at the particle location $\mathbf{u}(\mathbf{X}^{(i)}(t), t)$ is obtained from the fluid velocity at grid nodes. The numerical value of the fluid velocity field $\mathbf{u}(\mathbf{x}, t)$ at the particle location $\mathbf{X}^{(i)}(t)$ is denoted $(\mathbf{u}(\mathbf{X}^{(i)}(t), t))_M$, and is obtained from the representation of $\mathbf{u}$ at $M$ grid nodes through interpolation (Garg et al., 2009)

$$(\mathbf{u}(\mathbf{X}^{(i)}(t), t))_M = \Im(\mathbf{u}_m, m = 1, ..., M; \mathbf{X}^{(i)}(t)), \tag{3.25}$$

where $\mathbf{u}_m$ is the fluid velocity at the $m^{th}$ fluid grid node and $\Im$ is a generic interpolation operation. In this study we use second order Lagrange polynomial interpolation.

### 3.3.1 Simulation approach

Here we describe how the steady flow field past granules is obtained using the PUReIBM approach. Then the Lagrangian tracking of particles is described. In PUReIBM, the granules are first initialized in a lattice arrangement with a Maxwellian velocity distribution corresponding to a volume fraction of the granules $\epsilon_s$. The granules are then allowed to collide elastically to obtain an equilibrium configuration without the presence of the ambient fluid. A steady flow is established past the equilibrium particle configuration by imposing a pressure gradient that corresponds to a specified mean slip Reynolds number $Re_m$. The mean pressure gradient evolves in time until it attains a steady value required to drive the desired flow rate. The steady flow fields obtained from PUReIBM are used for Lagrangian tracking of particles. In this work, we simulate steady filtration in flow past fixed granule assemblies, but PUReIBM has been used to simulate moving granules also (Tenneti et al., 2010).

The particles are continuously injected into the computational domain at a specified mass injection rate $\dot{m}_{in}$. The particles are assigned the fluid velocity at the initial particle location. The boundary conditions for particles are inflow at $x = 0$, outflow at $x = L$, and periodic in the $y$ and $z$ directions. A particle is assumed to be trapped by the granular assembly when the distance between the centres of the granule and the particle is less than $(r_p + D_g/2)$ , where $r_p$ is the radius of the particle and $D_g$ is the diameter of the granule. This trapping criterion accounts for both inertial impaction and interception. The particles are removed from the simulation at the outlet plane $x = L$, where $L$ is the length of the computational domain. Figure 3.6 shows the result of a DNS-LPT simulation. The red spheres are the particles being filtered and the blue spheres are the granules.

## 3.4 DNS-LPT: Numerical convergence and validation

### 3.4.1 Numerical convergence study

Here we establish that the DNS-LPT simulations give numerically converged solutions. We examine the influence of grid resolution $D_m = D_g/\Delta x$ on penetration $P$, where $D_g$ is the granule diameter, and $\Delta x$ is the size of each grid cell. The penetration is calculated after the DNS-LPT simulations reach steady state. Figure 3.7 shows the variation of penetration $P = \dot{m}_{out}/\dot{m}_{in}$ with time, where $\dot{m}_{in}$ is the mass of the particles injected at the inlet and $\dot{m}_{out}$ is the mass of the particles exited from the outlet. The

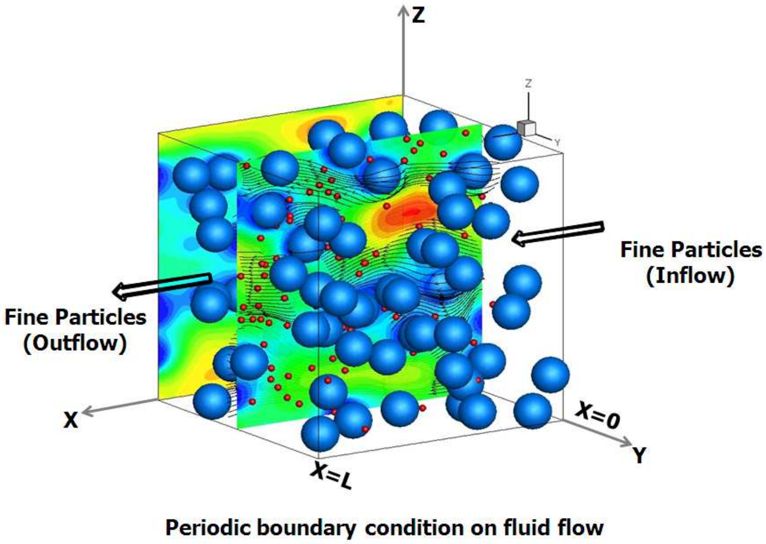

Figure 3.6 Trapping of particles in a random assembly of granules using DNS-LPT. Contours of the streamwise component of velocity are shown for a granule volume fraction of 0.1 and mean slip Reynolds number of 0.01. The Stokes number of the particles in this simulation is $4 \times 10^{-3}$.

penetration reported in this study is calculated from simulations as

$$P = \frac{\int_{t_{steady}}^{t_{stop}} \dot{m}_{out} dt}{\int_{t_{steady}}^{t_{stop}} \dot{m}_{in} dt} = \frac{m_{out}}{m_{in}}, \tag{3.26}$$

where $t_{steady}$ is the time when the simulation reaches steady state and $t_{stop}$ is the total simulation time. Numerical convergence is shown for a test case with particle Stokes number of 0.25, granule volume fraction 0.4, and a mean slip Reynolds number of 20. Note that $L/D_g$ is a physical parameter in these inflow/outflow simulations, and $P$ decreases with increasing $L/D_g$. In the test case shown $L/D_g = 4$, but the same convergence hold for $L/D_g = 6, 8, 10$ (results not shown here). Fig. 3.8 shows that the penetration $P$ converges with $D_m$ for $D_m > 30$.

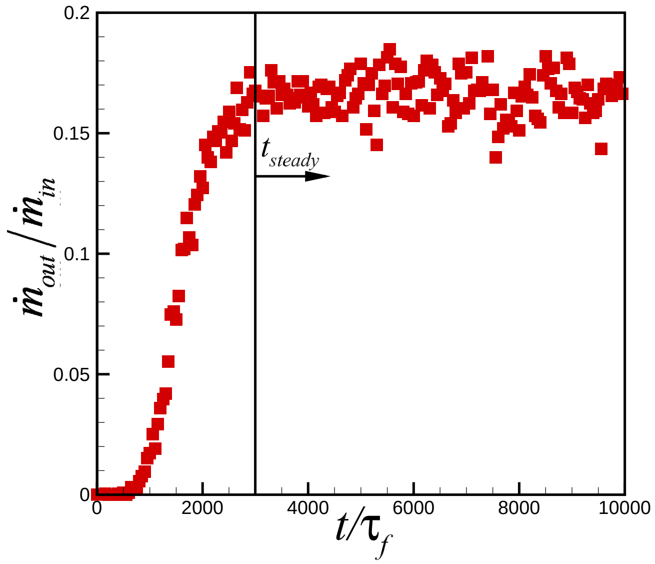

Figure 3.7 Variation of penetration for a particle Stokes number of $St = 0.10$, granule volume fraction $\epsilon_s = 0.5$, mean-slip Reynolds number $Re_m = 10$ with time $t$ normalized by fluid time scale $\tau_f$.

### 3.4.2 Validation

The DNS-LPT computational approach developed to model granular filtration is validated by comparing the penetration $P$ and single-collector efficiency $\eta_s$ obtained from DNS-LPT with the experimental data of D'Ottavio and Goren (1983). A summary of the simulation conditions used to obtain the DNS-LPT data points in Fig. 3.9 are shown in Table 5.1.

In order to meaningfully compare data from filtration experiments performed with different bed lengths $L$, it is common practice to compare the single-collector efficiency ($\eta_s = -2D_g \ln P/3\epsilon_s L$). In Fig 3.9, we show the variation of single-collector efficiency with effective Stokes number $St_{\text{eff}}$, obtained from both the DNS-LPT and experimental

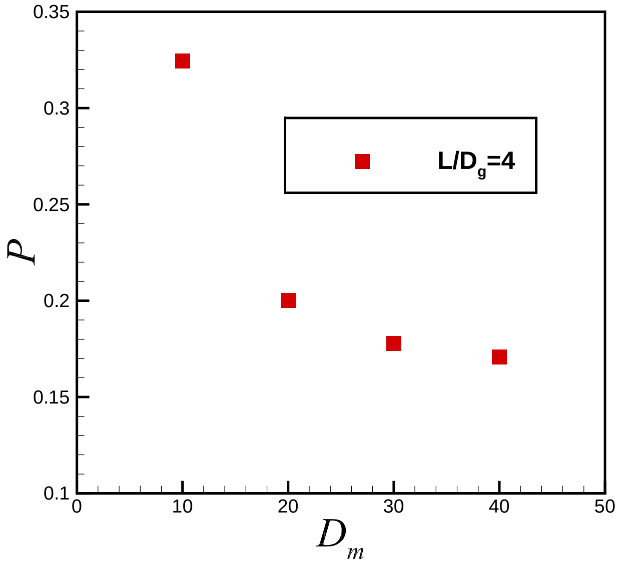

Figure 3.8 Convergence characteristics of penetration for a particle Stokes number of $St = 0.25$, granule volume fraction $\epsilon_s = 0.4$, mean-slip Reynolds number $Re_m = 20$ with grid resolution $D_m$ for $L/D_g = 4$.

data. The effective Stokes number $St_{\text{eff}}$ is defined as

$$St_{\text{eff}} = \left[ A(\epsilon_s) + 1.14 Re_m^{1/2} \left(1 - \epsilon_s\right)^{-3/2} \right] \frac{St}{2}, \tag{3.27}$$

$$A(\epsilon_s) = \frac{(6 - 6{\epsilon_s}^{5/3})}{(6 - 9{\epsilon_s}^{1/3} + 9{\epsilon_s}^{5/3} - 6{\epsilon_s}^2)}. \tag{3.28}$$

Figure 3.9 shows a good match of single-collector efficiency obtained from DNS-LPT simulations with experimental data. The scatter in the DNS-LPT data is probably indication of the inadequacy of $St_{\text{eff}}$ to collapse $\eta_s$ data from different $(Re_m, \epsilon_s)$ combinations. The solid line in Fig. 3.9 is the correlation (Eq. 3.8) suggested by D'Ottavio and Goren (1983) and the dashed line in Fig. 3.9 is the new correlation fitted to DNS-LPT data, which reads as

$$\eta_s = \frac{St_{\text{eff}}^{2.55}}{3.07 + St_{\text{eff}}^{2.55}}. \tag{3.29}$$

Equation 3.29 will be used for comparison of analytical particle expression with the DNS-LPT date in Sec. 3.5.2.2.

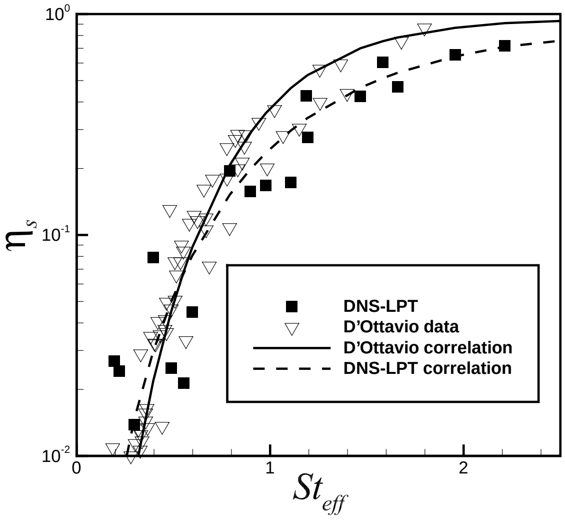

Figure 3.9 Comparison of single-collector efficiency as a function of effective Stokes number obtained from DNS-LPT simulations with the experimental data and correlation of D'Ottavio and Goren (1983) along with a correlation fitted to DNS-LPT date. Solid squares are simulation results, open gradients are experimental data, solid line is D'Ottavio correlation and dashed line is correlation fitted to DNS-LPT data.

The validation of single-collector efficiency with experimental data shows that the DNS-LPT approach developed in the present study gives accurate predictions of granular filtration.

## 3.5 Comparison of analytical model predictions with the DNS-LPT results

Polydisperse single-collector efficiency for different particle size distributions, and axial profiles of the particle flux predicted by the polydisperse filtration model are com-

Table 3.4 Granular filtration parameters for DNS-LPT validation

| **Parameters** | **Values simulated** | **Experiments** |
|---|---|---|
| $\epsilon_s$ | 0.4, 0.5 | 0.63 |
| $Re_m$ | 10, 20, 30, 50 | 10 - 1000 |
| $St$ | 0.05, 0.07, 0.1, 0.25 | $8.6 \times 10^{-4}$ - 0.18 |
| ${}^{L}/_{D_g}$ | 10 | 8 - 50 |

pared with results from the DNS-LPT code developed in Sec. 3.3 for both Stokes flow and at moderate Reynolds number.

### 3.5.1 Stokes flow

We consider particle filtration in a 2D unit cell for which Araújo et al. (2006) gave a correlation for monodisperse single-collector efficiency (Eq. 3.6), which is modified for the current study (see Eq. 3.7). We consider a polydisperse distribution of particles injected upstream, and the polydisperse filtration model predicts: (a) the cumulative polydisperse single-collector efficiency as a function of Stokes number, and (b) the total polydisperse single-collector efficiency. These are compared with Lagrangian particle tracking (LPT) simulation in flow fields obtained from the improved Kuwabara solution (Marshall et al., 1994) for Stokes flow in a 2D unit cell. Log-normal and gamma particle size distributions are considered as test cases. The CDFs of the log-normal and gamma particle size distributions at the inlet are shown in Figs. 3.10(a) and 3.10(b).

The cumulative polydisperse single-collector efficiency $\eta^{cum}_{s,poly}$ calculated analytically using Eq. 3.5 gives a very good match with $\eta^{cum}_{s,poly}$ obtained from LPT results for both log-normal and gamma distributions, as shown in Figs. 3.11(a) and 3.11(b). In the LPT simulations the size distribution is discrete and $\eta_{s,mono}$ is obtained for each discrete particle size, and then $\eta^{cum}_{s,poly}$ is obtained by adding the discrete PDF (of the particle size distribution) $\eta_{s,mono}$. A snapshot of the LPT simulation is shown in Fig. 3.12,

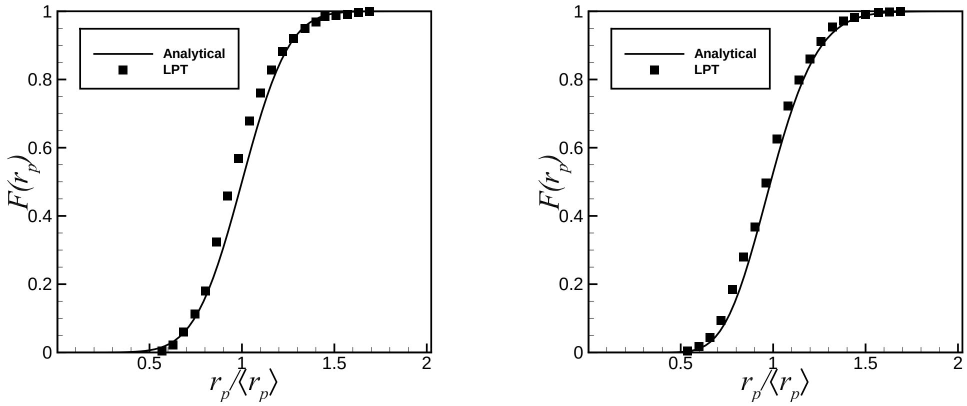

(a) (b)

Figure 3.10 CDF's of particle radius used in the analytical model and LPT simulations: (a) log-normal distribution of normalized particle radius with a mean 0.22 and a normalized standard deviation of $1.52 \times 10^{-2}$ (mean Stokes number $St = 0.50$ based on mean particle radius), both lengths are normalized by $D_g/2$. (b) gamma distribution of normalized particle radius with a mean 0.22 and a normalized standard deviation of $1.52 \times 10^{-2}$ (mean Stokes number $St = 0.50$ based on mean particle radius), both lengths are normalized by $D_g/2$.

where $\delta/2$ is the release position at the inlet of the computational cell above which the particle will always escape and $\delta/2$ increases with increase in particle size or Stokes number. The monodisperse single-collector efficiency is $\eta_{s,mono} = \delta/D$, where $D$ is the diameter of the collector. This simulation approach is similar to that used by Araújo et al. (2006) to calculate the single-collector efficiency. These results demonstrate the predictive capability of the simple analytical model developed in Sec. 3.2.1.

### 3.5.2 Moderate Reynolds number flow

#### 3.5.2.1 Particle size distribution along the granular bed

We now consider the analytical model's prediction of particle filtration in a three-dimensional granular bed. In this case we use the empirical correlation (Eq. 3.8)

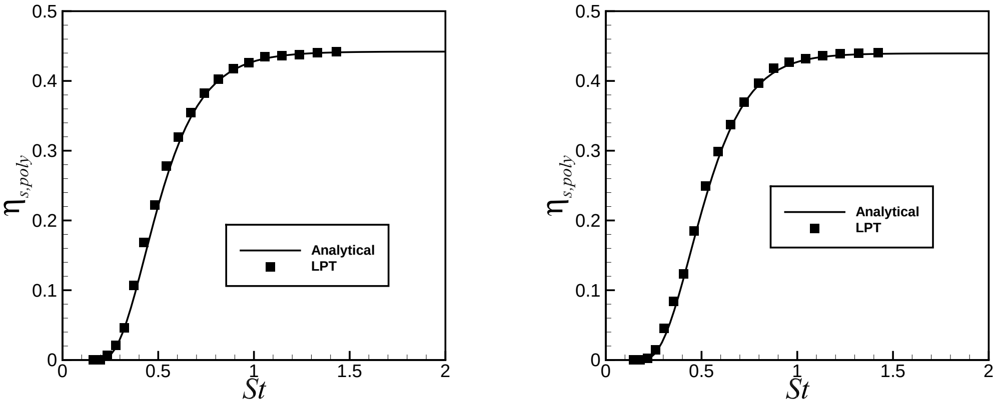

(a) (b)

Figure 3.11 Comparison of cumulative polydisperse single-collector efficiency $\eta_{s,poly}^{cum}$ with Stokes number between the analytical model and LPT simulations: (a) log-normal distribution of normalized particle radius with a mean of 0.22 and a normalized standard deviation of $1.52 \times 10^{-2}$ (mean Stokes number $St = 0.50$ based on mean particle radius), both lengths are normalized by $D_g/2$. (b) gamma distribution of normalized particle radius with a mean of 0.22 and a normalized standard deviation of $1.52 \times 10^{-2}$ (mean Stokes number $St = 0.50$ based on mean particle radius), both lengths are normalized by $D_g/2$.

of D'Ottavio and Goren (1983) for the single-collector efficiency of monodisperse particles. Results obtained from the 3D analytical model are compared with the DNS-LPT results obtained from the 3D granular bed for moderate Reynolds number. In the moderate Reynolds number case the DNS–LPT simulations use flow field PUReIBM.

Recall that our analysis (cf. Sec. 3.2.5) does not assume that the particle size distribution is constant along the length of granular bed, which is an assumption in most of the analytical models developed in the literature. The expression developed in Section 3.2.5 (Eq. 3.19) allows the particle size distribution to evolve along the length of bed due to variation in the filtration rate of particles of different sizes (Stokes number). In Fig. 3.13 we see how the particle size distribution varies along the length of the domain.

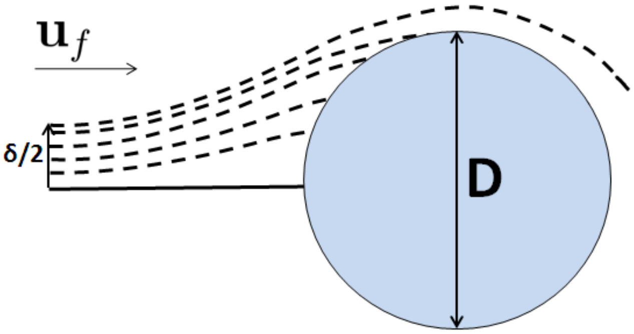

Figure 3.12 Particle trajectories when released from different positions at the inlet of a periodic unit cell

To understand this analysis further, we modify Eq. 3.15 as follows to obtain an expression for the evolution of the particle size distribution:

$$J(x)\frac{df(r|x)}{dx} + f(r|x)\frac{dJ(x)}{dx} = -\lambda\left(St_{\text{eff}}\right)J(x)f(r|x). \tag{3.30}$$

Rearranging terms in Eq. 3.30 leads to:

$$\frac{df(r|x)}{dx} = -\frac{1}{J(x)}\frac{dJ(x)}{dx}f(r|x) - \lambda\left(St_{\text{eff}}\right)f(r|x). \tag{3.31}$$

The first term on the right-hand side of Eq. 3.31 simply rescales the particle size distribution and the second term changes the shape of the particle size distribution along the length of the bed. Figure 3.14(a) shows the analytical prediction of particle size distribution at three axial locations in a granular bed, and the comparison of these analytical predictions with the DNS-LPT simulations are shown in Figs. 3.14(b), 3.14(c) and 3.14(d), respectively. It can be seen in Fig. 3.14 that the particle size distribution changes along the length of the bed and the analytical model predicts particle size distributions similar to the DNS-LPT results.

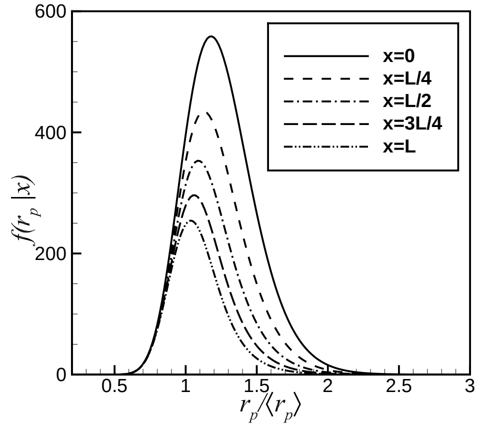

Figure 3.13 Analytical prediction of particle radius PDF along the granular bed of length $L$ at lengths $x = 0$, $x = L/4$, $x = L/2$, $x = 3L/4$ and $x = L$ for a log-normal distribution of normalized mean particle radius of $3.75 \times 10^{-3}$ and a normalized standard deviation of $7.5 \times 10^{-4}$ at the inlet plane (mean effective Stokes number $St_{\text{eff}} = 1.12$ based on mean particle radius, granule volume fraction $\epsilon_s = 0.5$ and mean slip Reynolds number $Re_m = 10$), both lengths are normalized by $D_g$.

#### 3.5.2.2 Axial variation of particle flux

Two test cases (test cases A and B in Table 3.2(a)) are chosen for comparison of the results obtained from the particle flux expression (Eq. 3.19) with the DNS-LPT results. The CDF of the particle radius for both the test cases are given in Figs. 3.15(a)-3.15(b).

The analytical prediction (see Eq. 3.19) of steady state normalized particle flux $J(x)/J(0)$ as a function of axial location $x$ is compared with DNS-LPT results in Figs. 3.16(a) and 3.16(b) for log-normal particle size distributions (test cases A and B). The granule solid volume fraction is 0.5 and the mean slip Reynolds number is 10 for these test cases. It should be noted that the error bars in the DNS-LPT simulations are 95% confidence intervals obtained from averaging over 5 independent simulations corresponding to different granule configurations with the same volume fraction $\epsilon_s$ and $g(r)$ (radial distribution function). Figures. 3.16(a) and 3.16(b) show that the particle flux decays along the axial coordinate due to filtration, and the trend of steady state normalized particle flux profile predicted by the analytical model is similar to the flux profile of DNS-LPT. It can also be seen in Figs. 3.16(a) and 3.16(b) that the analytical solution (solid line) overpredicts the decay of particle flux compared to the DNS-LPT results. This overprediction of particle flux decay in both test cases when compared with DNS-LPT data is due to the correlation (Eq. 3.8) used in the analytical particle flux expression (Eq. 3.19), which overpredicts the single-collector efficiency when compared with the DNS-LPT (see Fig. 3.9). To confirm this hypothesis we use the new correlation (Eq. 3.29) for single-collector efficiency fitted to DNS-LPT. The new correlation (Eq. 3.29) gives a better fit to DNS-LPT data, as seen in Fig. 3.9. The analytical particle flux expression with Eq. 3.29 instead of Eq. 3.8 predicts particle flux profiles (dashed lines in Figs. 3.16(a) - 3.16(b)) that match the DNS-LPT data. This good agreement between DNS-LPT and the model for axial variation of particle flux lends support to the theoretical formulation in Sec. 3.2.5, allowing prediction of axial flux profiles in granular filtration problems.

## 3.6 Conclusions

We have derived expressions for the cumulative polydisperse single-collector efficiency $\eta^{cum}_{s,poly}(St)$ and total polydisperse single-collector efficiency $\langle\eta_{s,poly}\rangle$ for granular filtration of particles with arbitrary size distributions in Stokes flow and moderate Reynolds number flows. Recognizing the Stokes number as the principal parameter determining filtration due to inertial impaction and interception, we transform the size distribution of particles to a distribution of Stokes number for the Stokes flow case. The expressions are also extended to moderate Reynolds number by converting the size distribution of particles to a distribution of effective Stokes number.

We also derived a transport equation for axial variation of the particle flux for polydisperse particles, which leads to an analytical solution for the size-dependent particle flux as a function of axial location. We developed a DNS-LPT approach for granular filtration of polydisperse particles that is valid for low and moderate Reynolds numbers. The penetration and single-collector efficiency obtained from DNS-LPT results give a good match with existing experimental data of D'Ottavio and Goren (1983). The results obtained from polydisperse analytical model give a very good match with 2D-LPT and DNS-LPT simulations. The analytical solution for the axial variation of particle flux predicts profiles similar to DNS-LPT results.

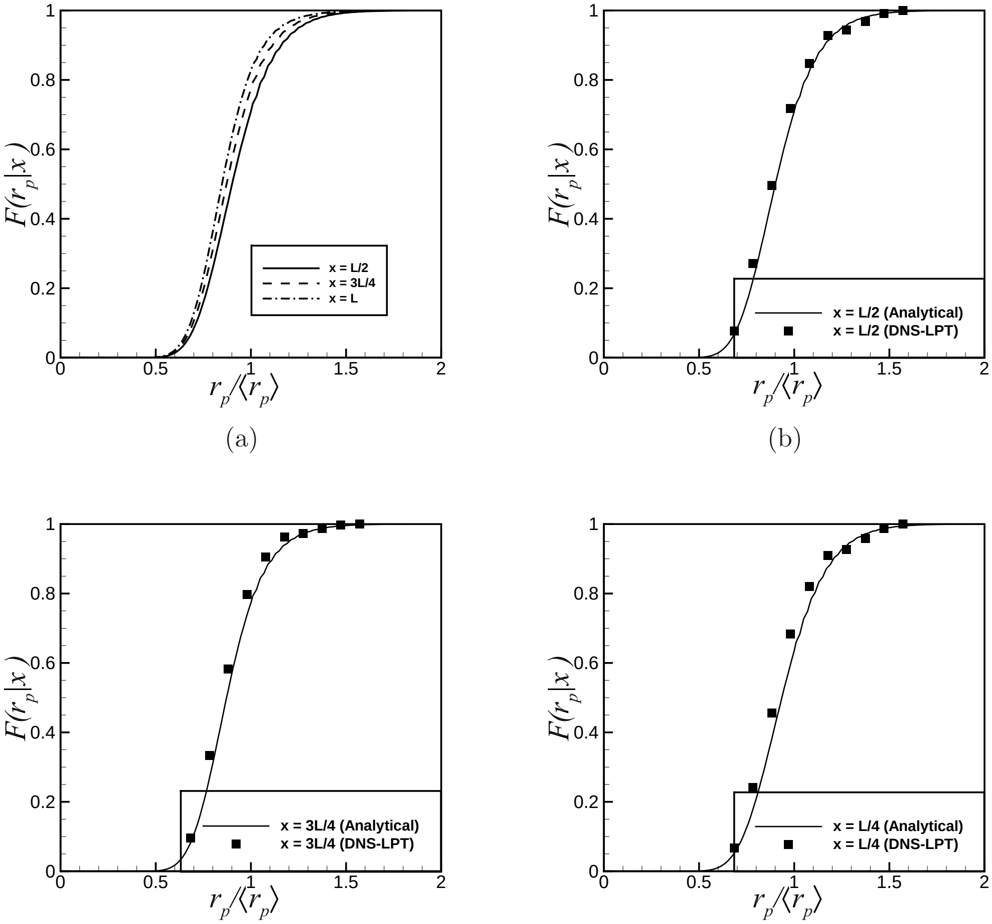

(a)

(b)

(c)

(d)

Figure 3.14 CDF of particle radius along the granular bed of length $L$, initialized with a log-normal distribution of normalized mean particle radius (by the radius of the granule) of $3.75 \times 10^{-3}$ and a normalized standard deviation of $7.5 \times 10^{-4}$ at the inlet plane (mean effective Stokes number $St_{\text{eff}} = 1.12$ based on mean particle radius, granule volume fraction $\epsilon_s = 0.5$ and mean slip Reynolds number $Re_m = 10$), both lengths are normalized by $D_g$: (a) analytical prediction of particle size distribution at lengths $L/2$, $3L/4$ and $L$ (b), (c) and (d) comparison of analytical prediction with DNS-LPT simulations at lengths $L/2$, $3L/4$ and $L$, respectively.

.

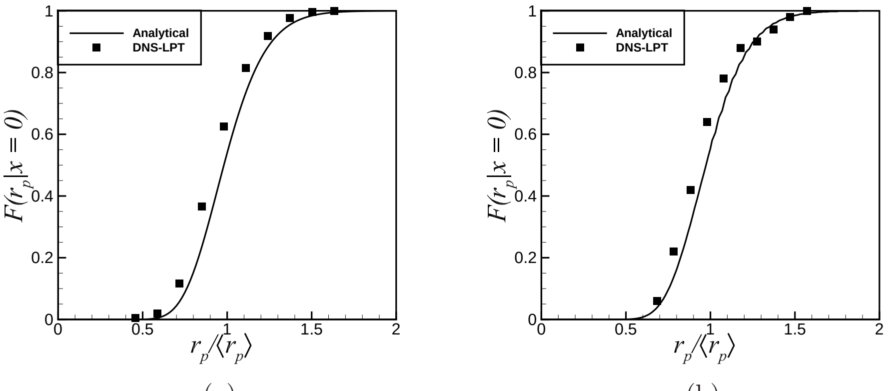

(a)

(b)

Figure 3.15 CDF of normalized particle radius at the inlet plane for a log-normal distribution of particles with : (a) normalized mean particle radius of $3.0 \times 10^{-3}$ and a normalized standard deviation of $6.0 \times 10^{-4}$ (mean effective Stokes number $St_{\text{eff}} = 0.72$ based on mean particle radius, granule volume fraction $\epsilon_s = 0.5$ and mean slip Reynolds number $Re_m = 10$), both lengths are normalized by $D_g$.(b) normalized mean particle radius of $3.75 \times 10^{-3}$ and a normalized standard deviation of $7.5 \times 10^{-4}$ (mean effective Stokes number $St_{\text{eff}} = 1.12$ based on mean particle radius, granule volume fraction $\epsilon_s = 0.5$ and mean slip Reynolds number $Re_m = 10$), both lengths are normalized by $D_g$.

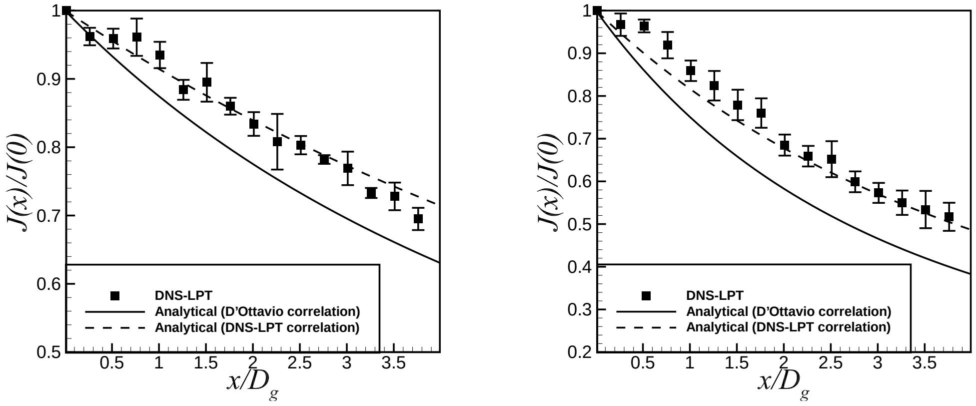

(a)

(b)

Figure 3.16 Steady state normalized particle flux $J(x)/J(0)$ along the flow domain for a log-normal distribution of particles: (a) Normalized mean particle radius of $3.0 \times 10^{-3}$ and a normalized standard deviation of $6.0 \times 10^{-4}$ (mean effective Stokes number $St_{\text{eff}} = 0.72$ based on mean particle radius, granule volume fraction $\epsilon_s = 0.5$ and mean slip Reynolds number $Re_m = 10$), both lengths are normalized by $D_g$.(b) Normalized mean particle radius $3.75 \times 10^{-3}$ and a nomrmalized standard deviation of $7.5 \times 10^{-4}$ (mean effective Stokes number $St_{\text{eff}} = 1.12$ based on mean particle radius, granule volume fraction $\epsilon_s = 0.5$ and mean slip Reynolds number $Re_m = 10$), both lengths are normalized by $D_g$.

# CHAPTER 4. Effect of particle bouncing on filtration efficiency in granular beds: direct numerical simulation and laser-based measurements

This chapter is a manuscript in preparation for Aerosol science and technology titled :Effect of particle bouncing on filtration efficiency in granular beds: direct numerical simulation and laser-based measurements authored by R. Kolakaluri,M. Cecconi, T. R. Meyer, and S. Subramaniam.

## 4.1 Introduction

Filtration of particulates from high speed gas flows using granular filters has widespread applications (El-Hedok et al., 2011; Meyer and Edwards, 1978; Ward, 1981; Goren, 1982; Ritzert et al., 2004). The versatility of granular filtration is evident form its scope of applications and ease of usage. Granular filters also perform better in high-temperature and high-pressure gas cleaning applications than fibrous filters which fail in these extreme conditions. The deposition of particles upon impact on a granule surface is an important step in granular filters as the particles are known to either deposit or rebound from granule surfaces. Particles are known to rebound from the granule surface when the impact velocity exceeds a characteristic critical velocity, which depends on the particle and granule size, shape and their material properties. The simple assumption of particle deposition on the surface of the granule upon impact is a good approximation for particles impacting on granules at low velocities. In some applications the bouncing or rebound of particles is desirable and in other cases it is not. Hence it is necessary to have a fundamental understanding of adhesion process occurring during particle impaction on the granule surface.

A particle bounces from a granule surface if the kinetic energy of the particle is able to overcome the adhesion energy at the surface. Researchers (Dahneke, 1971; Wall et al., 1990) has derived energy balance equations for the interaction of a particle with a surface, and have developed theoretical models for the critical velocity above which the particle will bounce from the surface. Experimental measurements of adhesion for particles impacting surfaces were conducted using two different approaches. One is the direct approach where measurements are made of the incoming and rebounding particle velocities (Dahneke, 1973; Wall et al., 1990) and in the second experimental approach, the onset of particle bounce from the surface is detected as a decrease in collection which occurs when the impact velocity of the particles is greater than the critical velocity. The latter approach was used by D'Ottavio and Goren (1983); Jung et al. (1989); Aylor and Ferrandino (1985); Wang and John (1988).

Due to the difficulties in measuring the incoming and rebounding velocities of particle from a granule surface in a granular bed, the second experimental approach is mostly used. D'Ottavio and Goren (1983); Jung et al. (1989) proposed correlations based on the second experimental approach for the probability of sticking or adhesion probability $\gamma$ as

$$\gamma = \frac{\eta_{s,bounce}}{\eta_s} \tag{4.1}$$

where $\eta_s$ is the single-collector efficiency considering particles stick to granules upon collision to granules and $\eta_{s,bounce}$ is the single-collector efficiency when the particles are allowed to rebound from the surface of the granules. The correlation for probability of sticking is given in terms of the effective Stokes number $St_{eff}$, which combines three independent dimensionless groups mean slip Reynolds number $Re_m = (1 -$

$\epsilon_s) \langle W \rangle D_g \rho_f / \mu$, particle Stokes number $St = \langle W \rangle d_p^2 \rho_p / 9 D_g \mu$ and granule volume fraction $\epsilon_s$ into one D'Ottavio and Goren (1983). In the above expressions, $\langle W \rangle$ is the mean slip velocity between fluid and granules, $D_g$ is the granule diameter, $\rho_p$ is the particle density, $d_p$ is the particle diameter, $\rho_f$ is the fluid density and $\mu$ is the fluid dynamic viscosity.

The bouncing studies done by Dahneke (1973, 1995); Wall et al. (1990) are for simple rebounding of particles from a flat surface. These are done in vacuum where the effect of the viscous drag forces and the effect of neighbouring granules are missing, and hence they cannot be directly applied to granular filtration problems. In both studies of the probability of sticking (D'Ottavio and Goren, 1983; Jung et al., 1989) computed by Eq. 4.1 for different conditions when plotted with effective Stokes number have order of magnitude scatter, which can be attributed to particles having different adhesion energy and kinetic energy. It is important to suggest a correlation for the probability of sticking $\gamma$ as a function of both the effective Stokes number and the adhesion energy so that the correlation be used in CFD simulations of granular filter for different kinds of particles.

In this study we use a DNS-LPT approach (Kolakaluri et al., 2013; Kolakaluri and Subramaniam, 2013) to simulate granular filtration and allow the particles to bounce from the surface of the granule if the incoming velocity of the particles is greater that the critical velocity (Dahneke, 1995). In the DNS-LPT approach we use flow past a homogeneous random assembly of granules which is a better representation of the complex flow structure in a granular bed. By using the DNS-LPT approach for simulating the granular filtration, we are able to include the effect of viscous drag forces and the effect of neighbouring granules on the bouncing of particles in a granular bed and also account for the incoming kinetic energy of the particles.

The paper is organized as follows. In Section 4.2 we describe the experimental setup of the granular filter and the critical velocity calculation for experiments are described in Section 4.3. The DNS–LPT simulation methodology and the bouncing implementation are described in Section 4.4. Finally, in Section 4.5 we compare the DNS–LPT results with the experiments and published results, and also suggest a correlation for probability of sticking $\gamma$ as a function of the adhesion energy and effective Stokes number.

## 4.2 Experimental setup

A schematic of the experimental setup is shown in Fig.5.4.3, where it can be seen that the particles are released into the duct and allowed to flow into the granular bed through the annular pipe. The measurements of the particles at the inlet and outlet of the granular bed is done using laser sheets. Laser sheets are passed horizontally through the test section before and after the filter, and signal from both regions is collected on a common camera. This ensures proper normalization between the two regions due to the matched sensitivity and uniformity of the detector. The current tests with monodisperse particles allow extraction of filtration efficiency, defined as the average difference in particles before and after the filter divided by the average incoming particles. Data were collected for over 200 scattering images for varying bed length using an Nd:YAG 5 nano second pulsed laser.

Table 4.1 Experimental conditions

| **Variables** | **Values** |
|---|---|
| $\epsilon_s$ | 0.5 |
| $Re_m$ | 61 |
| $D_g$ | $2 \times 10^{-3}$m |
| $d_p$ | $2 \times 10^{-5}$m |
| $\rho_p$ | 1200 kg/m$^3$ |
| $^{L}/_{D_g}$ | 5.6 , 10 |

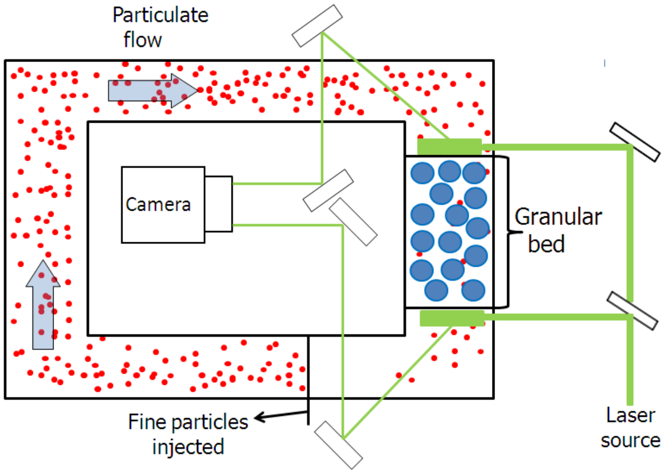

Figure 4.1 Schematic drawing of experimental apparatus

## 4.3 Theory behind critical velocity calculation

At low impact velocities, particles colliding with the granules adhere to the surface due to insufficient kinetic energy to escape the adhesion potential well. If the velocity of the particle approaching towards the granule is greater than a critical value, then the particle will have enough kinetic energy to escape the adhesion potential well, resulting in particle bouncing from the granule surface. The expression for critical velocity of a particle colliding on a surface is given by Dahneke (1995) as:

$$V_{crit} = \left[\frac{2E}{m}\frac{(1-e^2)}{e^2}\right]^{1/2}, \tag{4.2}$$

where $E$ is the adhesion energy, $e$ is the coefficient of restitution, and $m$ is the mass of the particle. In the absence of electrostatic forces, the adhesion energy $E$ between the particle and the granule can be estimated by the Bradley-Hamaker theory. For a particle of diameter $d_p$ and a spherical granule of diameter $D_g$, $E$ is given as

$$E = \frac{Ad_p}{12\delta_0(1+N_R)}, \tag{4.3}$$

where $A$ is the Hamaker constant and $\delta_0$ is the average center to center distance between the atoms composing the particle and granule, $N_R$ is the ratio of particle diameter to the granule diameter. If we know the adhesion energy $E$, coefficient restitution $e$ at the contact of particle and surface, and the diameter of the particle and granule. The critical velocity at which the particle bounce from the granule surface can be found using Eq. 4.2-4.3.

If the coefficient of restitution $e$ is not known prior it can also be obtained by (Dahneke, 1995)

$$e = \left[e_0^2 + \exp\left(-3.4\Lambda\right) - 1\right]^{1/2}, \tag{4.4}$$

where $e_0$ is the value of $e$ corresponding to the case of no flexural work, and $\Lambda$ is the inelasticity parameter. Dahneke (1971) gave an expression for sphere-cylinder interaction, which can also be used for sphere-sphere interaction because of the granule being much bigger than the particles. The inelasticity parameter is given as

$$\Lambda = \frac{2}{3\pi^{2/5}} \left[\frac{d_p^2}{D_g^2}\right] \left[\frac{1}{1 + \dfrac{d_p}{D_g}}\right]^{1/10} \left[\frac{V_n}{V_s}\right]^{1/5} \left[\frac{\rho_p}{\rho_g}\right]^{3/5} \left[\frac{\kappa_g}{\kappa_g + \kappa_p}\right]^{2/5}, \tag{4.5}$$

where $V_n$ is the incident normal velocity of the particle and $V_s$ is defined as $1/(\kappa_g \rho_g)^{1/2}$, $d_p$ and $D_g$ are the particle and granule diameters, respectively and $\kappa_p$ and $\kappa_g$ are defined by $\kappa_i = (1 - \nu_i^2)/Y_i$, where $\nu_i$ and $Y_i$ are the Poisson ratio and Young modulus for material $i$. In the next section we discuss the critical velocity calculations for experiments

### 4.3.1 Critical velocity calculation for experiments

The experimental setup is shown in Fig. 5.4.3. The experiments are done with fly ash of $20 \times 10^{-6}$ diameter and silica granules of $2 \times 10^{-3}$ diameter for a mean Reynolds number of 61 and a solid volume fraction of $\epsilon_s = 0.5$. The Hamaker constant for the flyash and silica interaction can be obtained from the expression given by Israelachvili

(2010):

$$A_{silica-ash} = \left(A_{silica} \times A_{flyash}\right)^{1/2}, \tag{4.6}$$

The critical velocity obtained from Eq. 4.2 is normalized with a reference velocity to be used in the DNS-LPT simulations and the normalized critical velocity $V^*_{critical}$ is shown in Table. 4.2. In the next section we describe the DNS-LPT simulation methodology and the bouncing implementation in the DNS-LPT simulations.

Table 4.2 Numerical values

| **Variables** | **Values** | **Units** | |
|---|---|---|---|
| $A_{silica-ash}$ | $1.626 \times 10^{-20}$ | Joule | |
| $E_{silica-ash}$ | $1.609 \times 10^{-16}$ | Joule | Eq. 4.3 |
| $V_{critical}$ | $1.723 \times 10^{-3}$ | m/s | Eq. 4.2 |
| $V^*_{critical}$ | $2.69 \times 10^{-3}$ | m/s | |

## 4.4 DNS-LPT simulation methodology

Here we describe how the mean flow Reynolds number and granule volume fraction are specified in the DNS. Granules are initialized in a lattice arrangement corresponding to a specified granule volume fraction $\epsilon_s$, corresponding to the granule volume fraction the granules are initialized in a lattice arrangement with a Maxwellian velocity distribution and the granules are then allowed to collide elastically to obtain a equilibrium configuration. The mean pressure gradient that corresponds to a specified mean slip Reynolds number is imposed and allowed to evolve in time until it attains a steady value required to drive a desired flow rate.

Lagrangian tracking of particles is done in steady flow fields obtained from PUReIBM. The particles are injected at a specified injection rate $\dot{m}_{in}$ continuously into the computational domain. The particles injected at the inlet are initialized with the fluid velocity at the particle positions. The boundary conditions for both the cases is inflow at $x = 0$ and outflow at $x = L$ where $L$ is the length of the computational domain. In the $y$ and $z$ direction the particles are given periodic boundary condition. A particle is considered to be trapped by the granular assembly when the distance between the centres of the granule and the particle is less than $(r_p + D_g/2)$ , where $r_p$ is the radius of the particle and $D_g$ is the diameter of the granule and the normal particle velocity is less than the characteristic critical velocity. At the same distance from the granule surface the particle is allowed to bounce if the normal particle velocity is greater than the characteristic critical velocity. The particles are removed from the simulation at the outlet plane $x = L$. The bouncing of particles implementation into DNS–LPT is described in next section.

### 4.4.1 Bouncing implementation: Hard-sphere collision model

The particle bounces from the surface of the granule if the normal pre-collisional particle velocity is greater than the critical velocity. The post-collisional velocity of the particle depends on the coefficient of restitution $e$, which is defined as

$$e = \frac{\mathbf{v}_2^{'} - \mathbf{v}_1^{'}}{\mathbf{v}_1 - \mathbf{v}_2}. \tag{4.7}$$

Where $\mathbf{v}_1$ and $\mathbf{v}_2$ are the pre-collisional velocities of the particle and granule, and $\mathbf{v}_1^{'}$ and $\mathbf{v}_2^{'}$ are the post-collisional velocities of the particles and granule. Solving the momentum conservation equation and Eqn. 4.7 can be written as

$$\mathbf{v}_1^{'} = \mathbf{v}_1 + \frac{m_2(\mathbf{v}_2 - \mathbf{v}_1)(1 + e)}{m_1 + m_2}. \tag{4.8}$$

The post-collisional velocities of the particle and granule can be further written as

$$\mathbf{v}_1^{'} = \mathbf{v}_1 - \frac{m_2(1 + e)}{m_1 + m_2}(\mathbf{k} \cdot \mathbf{v}_{12})\mathbf{k}, \tag{4.9}$$

and

$$\mathbf{v}_2^{'} = \mathbf{v}_2 + \frac{m_1(1 + e)}{m_1 + m_2}(\mathbf{k} \cdot \mathbf{v}_{12})\mathbf{k}. \tag{4.10}$$

Where **k** is the unit vector along the line joining the centers of both the particle and the granule and $\mathbf{v}_{12}$ is the relative velocity between particles.

## 4.5 Results and Discussions

### 4.5.1 Comparison of DNS–LPT with laser-based experiments

The laser experiments are done for two different granular beds, the length of the first granular bed is $0.44''$ and the other granular bed is $0.79''$. In experiments the granular filter efficiency $\eta$ is obtained by measuring the mass of particles at the inlet and outlet:

$$\eta = \frac{\dot{m}_{in} - \dot{m}_{out}}{\dot{m}_{in}}, \tag{4.11}$$

where $\dot{m}_{in}$ is the mass of the particles at the inlet and $\dot{m}_{out}$ is the mass of particles at the outlet of the granular bed. The filter efficiency $\eta$ obtained from DNS-LPT results are compared with two experimental cases ($0.44''$ filter and $0.79''$ filter).

It can be seen in Fig. 4.2 that with the implementation of bouncing mechanism, the DNS simulation gave a better match with the experimental results compared to the DNS-LPT results with $P_{stick} = 1$, where $P_{stick}$ is the probability of sticking of particles on granule surface. Two bounds on the coefficient of restitution $e$ can be observed from Fig. 4.2, one is as $e \to 0$ that is inelastic limit, all particles regardless of their initial velocity lose all their energy and stick to the granules and this is more like going to the no-bounce limit. The other bound is as $e \to 1$, $V_{critical}$ tends to go to a very small value (Eq. 4.2 and Fig. 4.4) and very few particles will stick as the probablity of $V > V_{critical}$ is small. Hence $\eta$ tends to a very small value as $e \to 1$. The error bar on the DNS-LPT are the standard deviation obtained from averaging the penetration over time after the steady state is reached.

In Fig. 4.3, we can see a very good comparison of the DNS results with experimental results for $0.79''$ filter. The same kind of bound on $e$ can be observed for $0.79''$ filter as

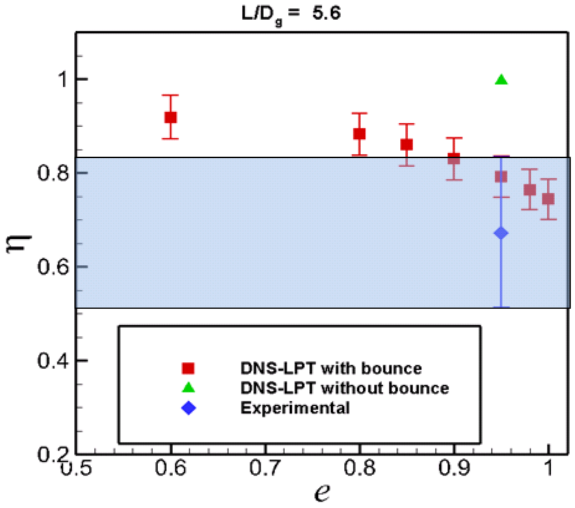

Figure 4.2 The comparison of filter efficiency obtained from DNS with experimental results. DNS is for different coefficient of restitution for a filter of length 0.44″ at mean Reynolds number 61 and solid volume fraction 0.5.

observed for 0.44″ filter, except the effect of $e$ on the filter efficiency is less in the case of 0.79″ filter compared to small filter, this is due to increase in probability of particles to collide on granule surface due to the increase in the length of granular filter.

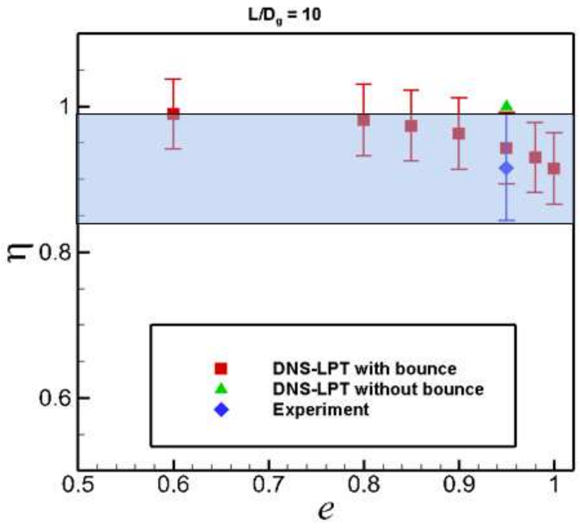

Figure 4.3 The comparison of filter efficiency obtained from DNS with experimental results. DNS is for different coefficient of restitution for a filter of length $0.79''$ at mean Reynolds number 61 and solid volume fraction 0.5.

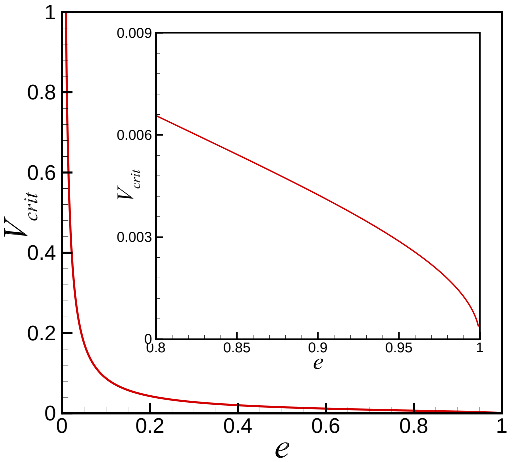

Figure 4.4 The variation of $V_{critical}$ for fixed adhesion energy $E$ and mass of the particle $m_p$.

### 4.5.2 Comparison of DNS–LPT with published results

The DNS-LPT results of the adhesion probability $\gamma$ when compared with the results of D'Ottavio and Goren (1983) gives a reasonable match as seen in Fig. 4.5. Where the effective Stokes number in Fig. 4.5 is defined as

$$St_{\text{eff}} = \left[A(\epsilon_s) + 1.14 Re_m^{1/2} \left(1 - \epsilon_s\right)^{-3/2}\right] \frac{St}{2}, \tag{4.12}$$

$$A(\epsilon_s) = \frac{(6 - 6{\epsilon_s}^{5/3})}{(6 - 9{\epsilon_s}^{1/3} + 9{\epsilon_s}^{5/3} - 6{\epsilon_s}^{2})}. \tag{4.13}$$

The effective Stokes number suggested by D'Ottavio and Goren (1983) to collapse single-collector efficiency data for moderate mean slip Reynolds number was modified to reflect the weak dependence of single-collector efficiency on mean flow Reynolds number for $Re_m > 10$ by changing the $Re_m^{1/2}$ dependence to $Re_m^{1/5}$ (Kolakaluri and Subramaniam, 2013). In the remaining part of this study we will be using the modified effective Stokes number $St^*_{\text{eff}}$, which gives a better collapse than the effective Stokes number. The

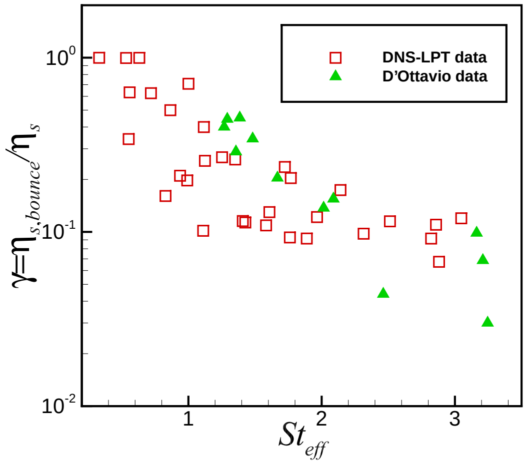

Figure 4.5 Comparison of adhesion probability $\gamma$ obtained from DNS–LPT results withD'Ottavio and Goren (1983).

modified effective Stokes number is defined as

$$St^*_{\text{eff}} = \left[ A(\epsilon_s) + 1.14 Re_m^{1/5} \left(1 - \epsilon_s\right)^{-3/2} \right] \frac{St}{2}. \tag{4.14}$$

However there is lot of scatter in both the experimental and DNS-LPT data, which is mainly due to the particles having different adhesion energy $E$ that binds to the granules and the differences in the the granular temperature $T$ of the particles in the granular bed. The granular temperature $T$ is a measure of the variance in the particle velocities and is defined as $T = \frac{1}{3} \langle v_i'' v_i'' \rangle$, where $v_i''$ is the fluctuation in the particle velocity defined with respect to the mean particle velocity. In order to introduce the effect of adhesion energy and particle granular temperature in the adhesion probability, we use a normalized adhesion energy $H_T = E/0.5 m_p T$, where $m_p$ is the mass of each particle.

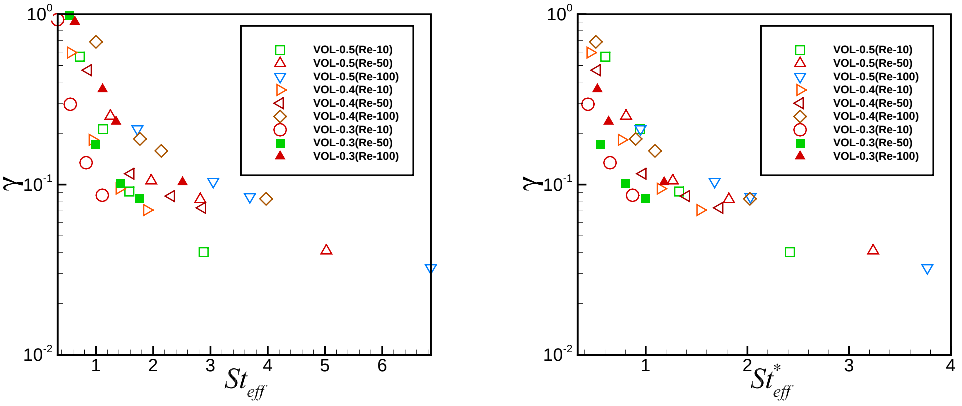

(a) (b)

Figure 4.6 (a)Adhesion probability $\gamma$ with effective Stokes number $St_{eff}$ from DNS-LPT data.(b)Adhesion probability $\gamma$ with modified effective Stokes number $St^*_{eff}$ from DNS-LPT data.

In Fig. 4.6(a)-4.6(b) we can see the variation of adhesion probability with the effective Stokes number and modified effective Stokes number, and the modified effective Stokes number was not able to reduce the scatter in the adhesion probability data, which further points to the scatter in the data is due to different adhesion energy between particles and granules and the granular temperature of the particles in the granular bed.

### 4.5.3 Particle velocity variance in a granular bed

The granular temperature $T(x)$ is obtained from the particle velocity variance which depends on the particle inertia or Stokes number. In a granular bed the granular temperature reaches steady state after the filtration rate reaches a steady value. The variation of granular temperature in a granular bed along the mean flow direction is shown in Fig. 4.7. It can also also be seen in Fig. 4.7 that granular temperature decrease with particles Stokes number. For particles with $St \approx 0$ the particle granular temperature depends only on the turbulent kinetic energy of the fluid. Tenneti et al. (2013a) reported that the turbulent kinetic energy normalized by the mean energy of the fluid increase with volume fraction and decrease with increase in mean flow Reynolds up to $Re_m = 50$ and beyond $Re_m = 50$ it has a weak power law dependence on $Re_m$. It can

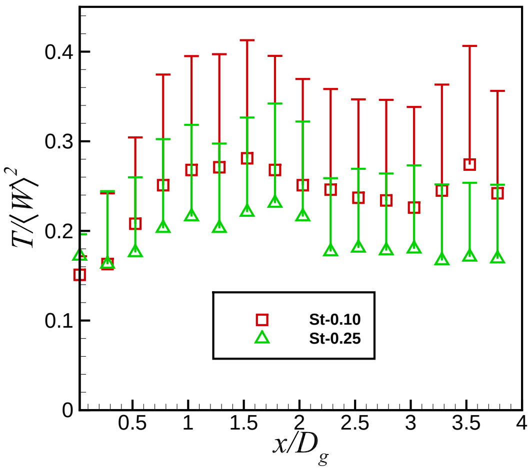

Figure 4.7 Variation of adhesion probability with the modified effective Stokes number and adhesion energy normalized by the granular temperature.

be seen in Fig. 4.8 that the granular temperature normalized by the turbulent kinetic energy decreases with a power law dependence with increase in particle Stokes number. This decrease is due to less influence of the fluid turbulent kinetic energy on the particle fluctuating energy with increase in particle inertia.

Tenneti (2013) suggested a correlation for steady state granular temperature in terms of mean slip Reynolds number, granule volume fraction and density ratio of particle and fluid:

$$\frac{T_{SS}}{|\mathbf{W}|^2} = 2(1-\epsilon_s)^3 \exp -0.02(1-\epsilon_s) Re_m \left(\frac{\rho_p}{\rho_f}\right)^{-1}. \tag{4.15}$$

For the $St = 0.10$ cases shown in Fig. 4.7 the $T_{SS}$ obtained from DNS–LPT simulations is 0.26, while the $T_{SS}$ obtained from Eq. 4.15 is 0.014137, which indicates that Eq. 4.15 underpredicts the particle granular temperature. Eq. 4.15 is underpredicting granular temperature compared to DNS–LPT because it has been developed from PR-DNS of particles with $St \approx 100$. Hence, a correlation is suggested for particle granular temperature from DNS–LPT in terms of the turbulent kinetic energy with a power law dependence on Stokes number as

$$T = k_f(1 - 0.6St^{0.7}). \tag{4.16}$$

The adhesion energy is a function of the properties of the particles and the granules, which has a positive effect towards particle sticking on the granule surface and on the other hand granular temperature is a measure of the fluctuating energy of the particles which helps to overcome the adhesion energy near granule surface and help the particles to bounce from the granule surface. Hence, the ratio of the adhesion energy to the granular temperature will be an appropriate parameter to quantify the adhesion probability of the particles. In Fig. 4.9(a) we can see the variation of the adhesion probability with the adhesion energy normalized by the granular temperature ($H_T$) and the modified effective Stokes number. We can see in Fig. 4.9(a) that with decrease in $H_T$ the adhesion

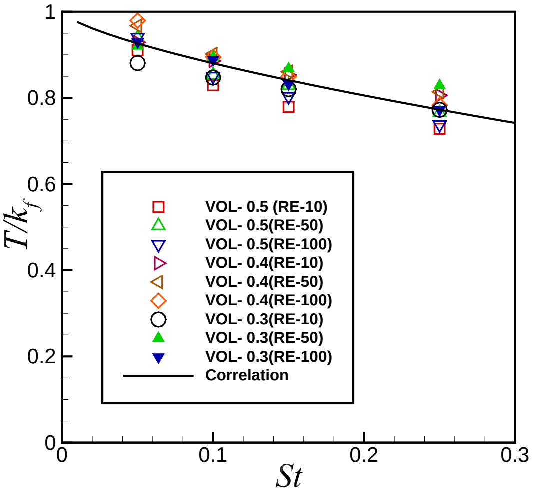

Figure 4.8 Variation of granular temperature normalized by the turbulent kinetic energy with particle Stokes number.

probability decrease and also the adhesion probability decrease with increase in effective Stokes number. Hence we can have a better understanding of the adhesion probability with the information of both $H_T$ and modified effective Stokes number. It can be seen in fig. 4.9(b) that the normalized adhesion energy raised to a negative power increases with Reynolds number and we also know that the $\gamma$ decrease with Reynolds number due to increase in bouncing, hence we can use normalized adhesion energy $H_T$ raised to a negative power to reduce the scatter in $\gamma$. $H_T$ is used to provide a correlation for adhesion probability in next section.

### 4.5.4 Model for adhesion probability

In the previous subsection we have seen that the adhesion probability is a strong function of the adhesion energy normalized by the granular temperature. In fig. 4.5 we have seen that the modified effective Stokes number was not sufficient to collapse the adhesion probability data, but by including the effect of the adhesion energy normalized

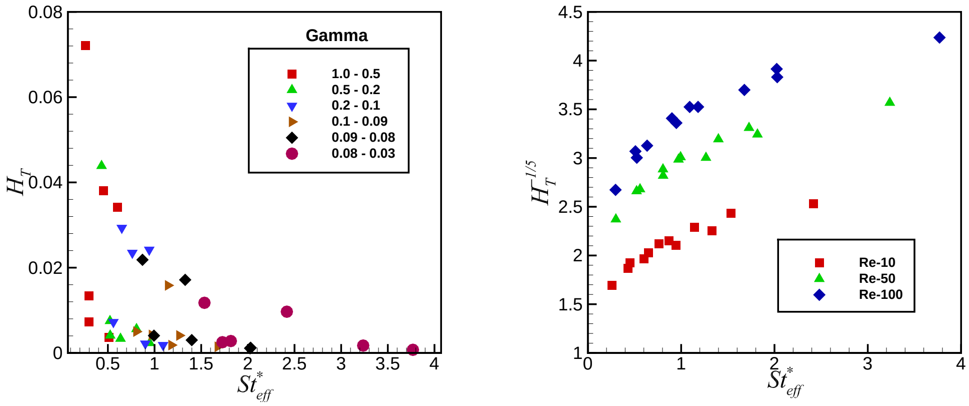

(a)

(b)

Figure 4.9 (a)Variation of adhesion probability with the modified effective Stokes number and adhesion energy normalized by the granular temperature.(b)Variation of $H_T$ with modified effective Stokes number $St^*_{eff}$.

by the granular temperature $H_T$ raised to a negative power we are able to collapse the adhesion probability data with modified effective Stokes number as can be seen in Fig. 4.10. Hence a correlation is proposed for the adhesion probability as a function of $H_T$ and the modified effective Stokes :

$$\gamma = 0.05 {St^*_{eff}}^{-3/2} H_T^{-1/5}. \tag{4.17}$$

## 4.6 Conclusions

The filter efficiency used to quantify the performance of a granular filter was determined experimentally using laser based experiments and a DNS–LPT approach was developed for granular filtration with bouncing of particles implemented using hard-sphere collision between particles and granules. The DNS–LPT results gave a decent match with the experiments with bouncing of particles implemented in the DNS approach. The adhesion probability obtained from DNS–LPT results gave a good match

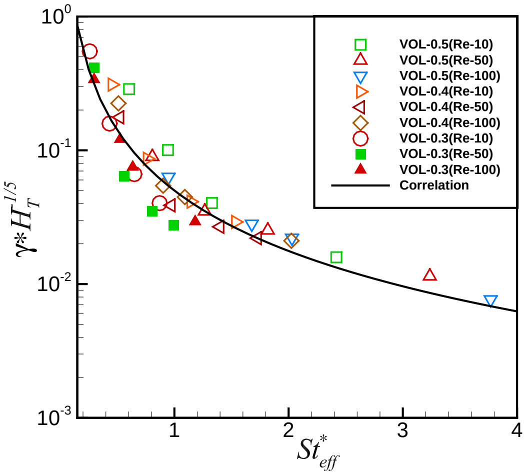

Figure 4.10 Adhesion probability $\gamma$ with the modified effective Stokes number.

with existing experimental data of D'Ottavio and Goren (1983) and the scatter in both the published results and the DNS-LPT results are due to different adhesion energy and granular temperature of the particles. A correlation for adhesion probability was also proposed from DNS–LPT data, which gave a good collapse of data with the inclusion of adhesion energy and granular temperature. The suggested correlation is valid for a wide range of particle Stokes number, granule volume fraction and mean slip Reynolds number and adhesion energy.

# CHAPTER 5. CFD modeling of granular filtration

## 5.1 Introduction

Granular filtration was traditionally used for water treatment, but due to the ease of its usage it is also widely used in chemical industries. Granular filtration is mostly used to treat flue gas, combustion products, polymers, and petrochemical products. The common process of conducting granular filtration is in the fixed-bed mode (D'Ottavio and Goren, 1983; Gal et al., 1985; Jung et al., 1989), but it can also conducted in a moving-bed (Ritzert et al., 2004; El-Hedok et al., 2011) or fluidized-bed mode so that the operation can be carried out continuously.

Granular filtration consists of two solid phases and one fluid phase : One of the solid phases comprises the granules through which the fluid flows, and the other solid phase consists of fine particles that are suspended in the fluid phase. Direct numerical simulation of a full-scale granular bed is prohibitively expensive in terms of the required computational resources. This is due to the range of length and time scales that need to be simulated. The other alternative approaches possible to simulate a full-scale granular bed would be to either use a Lagrangian-Eulerian (LE) or Eulerian-Eulerian (EE) approach. Current implementations of the LE approach in commercial software (that is needed to represent the complex geometry of a realistic moving bed granular filter) are computationally expensive, and hence the Eulerian-Eulerian two-fluid approach is chosen to model a full-scale granular bed.

In this study we develop a CFD model, where the granules and fluid phases are modeled using an Euler-Euler two-fluid model and the fine particles that are suspended in the fluid phase are simulated using two User-Defined-Scalars (UDS). One of the UDS represents the number density of particles suspended in the fluid phase and the other UDS is for number density of particles deposited on the granules, which are moving with the granules. The sink term in the UDS due to the deposition of particle on the granule surface is introduced in the UDS using User-Defined-Functions (UDF).

The chapter is organized as follows. In section 5.2 we describe the CFD model and the implementation procedure is discussed in section 5.3. The verification of the CFD model and comparison of CFD results with experiments are done in section 5.4. Section 5.5 reports the conclusions of this work.

## 5.2 Model description

### 5.2.1 Eulerian-Eulerian model

In the Euler-Euler model, the phases are treated as interpenetrating continua. The phases are described by means of continuity and momentum equation that are derived by ensemble averaging the local instantaneous balance equations (Enwald et al., 1996; Drew, 1971). The continuity equation for each phase is given as

$$\frac{\partial}{\partial t}(\epsilon_\phi \rho_\phi) + \nabla \cdot (\epsilon_\phi \rho_\phi \mathbf{U}_\phi) = 0, \tag{5.1}$$

where $\epsilon_\phi$ is the phase fraction, $\rho_\phi$ is the phase density and $\mathbf{U}_\phi$ is the phase velocity. The fluid phase momentum equation is given as

$$\frac{\partial}{\partial t}(\epsilon_f \rho_f \mathbf{U}_f) + \nabla \cdot (\epsilon_f \rho_f \mathbf{U}_f \mathbf{U}_f) = \nabla \cdot \tau_f - \epsilon_f \nabla p + \epsilon_f \rho_f \mathbf{g} - K_{drag}(\mathbf{U}_f - \mathbf{U}_s), \tag{5.2}$$

where the fluid phase stress tensor is given as:

$$\tau_f = \mu_f \left[\nabla \mathbf{U}_f + \nabla^T \mathbf{U}_f\right] - \frac{2}{3}\mu_f (\nabla \cdot \mathbf{U}_f)\mathbf{I}. \tag{5.3}$$

The granule phase momentum equation is written as

$$\frac{\partial}{\partial t}(\epsilon_s \rho_s \mathbf{U}_s) + \nabla \cdot (\epsilon_s \rho_s \mathbf{U}_s \mathbf{U}_s) = \nabla \cdot \tau_s - \epsilon_s \nabla p - \nabla P_s + \epsilon_s \rho_s \mathbf{g} + K_{drag}(\mathbf{U}_f - \mathbf{U}_s), \tag{5.4}$$

and the granule phase stress tensor is given as

$$\tau_s = \mu_s \left[ \nabla \mathbf{U}_s + \nabla^T \mathbf{U}_s \right] - (\lambda_s - \frac{2}{3}\mu_s)(\nabla \cdot \mathbf{U}_s)\mathbf{I}. \tag{5.5}$$

The interphase momentum transfer between the granular and fluid phase is modeled using an interphase drag term, which is a function of drag coefficient $K_{drag}$ and this coefficient is calculated according to Gidaspow (1994) and Modified Ergun's equation (Macdonald et al., 1979):

$$K_{drag} = \frac{3}{4} \frac{C_d \epsilon_f \epsilon_g \rho_f |\mathbf{U}_f - \mathbf{U}_s|}{D_g} \qquad \text{if} \quad \epsilon_s < 0.2 \tag{5.6}$$

$$K_{drag} = 180 \frac{\mu_f \epsilon_s^2}{\epsilon_f^2 D_g^2} + 1.8 \frac{\rho_f \epsilon_s |\mathbf{U}_f - \mathbf{U}_s|}{\epsilon_f D_g} \qquad \text{if} \quad \epsilon_s > 0.2. \tag{5.7}$$

Kinetic theory of the granular flow (Gidaspow, 1994) is used to calculate the dynamical properties of the granule phase, where the particle pressure and the particle shear and bulk velocities are calculated as a function of granular temperature $T$. The transport equation for the granular temperature $T$ is given as

$$\frac{\partial}{\partial t}(\epsilon_s \rho_s T) + \nabla \cdot (\epsilon_s \rho_s \mathbf{U}_s T) = \frac{2}{3} \left[ (-P_s \mathbf{I} + \tau_s) : \nabla \mathbf{U}_s + \nabla \cdot (\kappa_s \nabla T) - \gamma_s + J_{vis} + J_{slip} \right] \tag{5.8}$$

The particle phase bulk viscosity is given as (Gidaspow, 1994):

$$\lambda_s = \frac{4}{3} \epsilon_s^2 \rho_s D_g g_0 (1 + e_s) \left( \frac{T}{\pi} \right)^{0.5}, \tag{5.9}$$

where $g_0$ is the radial distribution function at contact and the particle pressure is calculated according to

$$P_s = \rho_s \epsilon_s T + 2 \rho_s \epsilon_s^2 g_0 T (1 + e_s). \tag{5.10}$$

The particle shear viscosity is given as a sum of collisional and kinetic contribution (Gidaspow, 1994) as shown below:

$$\mu_s = \frac{4}{5}\epsilon_s^2 \rho_s D_g g_0 (1+e_s) \left(\frac{T}{\pi}\right)^{0.5} + \frac{10\rho_s D_g \sqrt{T\pi}}{96 g_0 (1+e_s)} \left[1 + \frac{4}{5}(1+e_s)\epsilon_s g_0\right]^2. \tag{5.11}$$

The dissipation of granular energy due to viscous dissipation $J_{vis}$ and the production of granular temperature $J_{slip}$is modelled as (Gidaspow, 1994):

$$J_{vis} = -3K_{drag}T \tag{5.12}$$

$$J_{slip} = \frac{81\epsilon_s \mu_g^2}{g_0 d_p^3 \rho_s \sqrt{\pi T}} |\mathbf{U}_f - \mathbf{U}_s|^2. \tag{5.13}$$

### 5.2.2 Particle velocity model

The second particle phase in the granular bed is solved using as an advective scalar equation, which reads as

$$\frac{\partial \phi}{\partial t} + \nabla \cdot (\mathbf{u}\phi) = S_\phi, \tag{5.14}$$

where $\phi$ is the concentration of particles, $\mathbf{u}$ is the fluid velocity, and $S_\phi$ is the sink term due to particle filtration. Kolakaluri and Subramaniam (2013) found from DNS-LPT simulations that there is non-zero mean slip velocity for finite inertia particles in fluid flow. Hence the advective scalar equation is modified to include the particle velocity as

$$\frac{\partial \phi}{\partial t} + \nabla \cdot (\langle \mathbf{V} \rangle \phi) = S_\phi, \tag{5.15}$$

where $\langle \mathbf{V} \rangle$ is the mean particle velocity, and further the sink term can be modeled as $S = \lambda |\langle \mathbf{W}_{pg} \rangle| \phi$, where $\lambda$ is the filter coefficient and $\langle \mathbf{W}_{pg} \rangle = \langle \mathbf{V} \rangle - \langle \mathbf{V}_g \rangle$ is the relative velocity between the particles and the granules (not the slip between fluid and granule). In this CFD study we use the filter coefficient suggested by Kolakaluri and Subramaniam (2013):

$$\lambda = \frac{{St_{eff}^*}^{3.2}}{4.3 + {St_{eff}^*}^{3.2}}. \tag{5.16}$$

Eq. 5.15 can be discretized and can be written in modified form as

$$\frac{\phi_{n+1} - \phi_n}{\Delta t} + \int_S \rho\phi_n \langle \mathbf{V} \rangle \, d\mathbf{S} = -\int_V \rho\phi_n \lambda | \langle \mathbf{W}_{pg} \rangle | dV, \tag{5.17}$$

where $n$ is the current time step, $S$ and $V$ are the surface area and volume of the computational cell, respectively. UDF's are used for both RHS and LHS of Eq. 5.17 for implementation in ANSYS-FLUENT. In the EE CFD model, the particle velocity is obtained from the fluid velocity using the equilibrium Eulerian model suggested by Ferry and Balachandar (2001):

$$\mathbf{V} = \mathbf{u} + (1 - \beta) \left( -\mathbf{a}\tau + \left( \frac{\mathrm{D}\mathbf{a}}{\mathrm{D}t} + \mathbf{a}.\nabla\mathbf{u} \right) \tau^2 + O(\tau^3) \right), \tag{5.18}$$

where $\beta$ is the density parameter, $\mathbf{a}$ is the modified acceleration, $\mathbf{V}$ is the particle velocity, $\mathbf{u}$ is the fluid velocity and $\tau$ is the particle response time. If we neglect the second order terms, Eq. 5.18 can be reduced to

$$\mathbf{V} = \mathbf{u} - (1 - \beta)\mathbf{a}\tau, \tag{5.19}$$

where the fluid acceleration term $\mathbf{a}$ is written as

$$\mathbf{a} = \frac{D\mathbf{u}}{Dt} = \frac{d\mathbf{u}}{dt} + \mathbf{u} \cdot \nabla\mathbf{u} \tag{5.20}$$

The particle flux equation (Eq. 5.17) needs to be coupled with the EE CFD model. Since the mass loading of the particle phase is assumed to be negligible, fluid and granular momentum balance is assumed to be unaffected by particle fluid momentum transfer. Hence, one-way coupling between the particles and fluid phase is considered in this model. The numerical implementation of the particle model is discussed in the next section.

## 5.3 Numerical implementation of the scalar equations

In ANSYS-FLUENT, we solve two UDS equations. One UDS equation is used to solve the number density of particles suspended in the fluid phase with the particles depositing on the granule surface as sink term in the UDS equation. The other UDS equation is solved for the number density of particles deposited on the granule surface removed form the granular bed with granule velocity. The UDS equations are coupled with the multi-fluid CFD model. The algorithm for the coupling is as follows.

1. Solve the EE equations in each cell and obtain the velocities and volume fractions of the fluid and granule phases.
2. Solve both the UDS equations for the concentration of particles in the fluid and the particles deposited on the granule surface with UDFs for the sink terms.
3. As particles deposit on the granule surface, there is change in porosity of the granular bed which is implemented using a UDF.
4. Repeat Step 2 with the modified porosity of the granular bed.

## 5.4 Results and discussion

### 5.4.1 Validation of CFD model

The geometry used is of MBGF and the model is shown in Fig. 5.4(b). The fluid phase is given a constant velocity with a uniform profile at the inlet, and the pressure boundary condition is atmospheric pressure at the outlet. The initial velocity of the fluid phase at the inlet was set based on the flow rate and the granular phase is patched with zero velocity and a granular temperature equal to $1.0 \times 10^{-4}\text{m}^2\text{s}^{-2}$. The granular phase is allowed to freely fall due to the gravity with a pressure outlet boundary condition at the outlet. The fluid phase is given a no-slip boundary condition at the walls and the granular phase is given a partial-slip boundary condition (Johnson and Jackson, 1987) at the walls. The initial condition for the granule phase fraction is close packed for the regions occupied by the granules and zero where there is fluid.

The validation of the EE CFD model is done by comparing static bed results with Ergun's (Macdonald et al., 1979) correlation for pressure drop in packed beds. The pressure gradient obtained from the modified Ergun's equation (Macdonald et al., 1979) for the experimental conditions is 8500N/m$^2$ and the values obtained for a particular section (Fig. 5.1(a)) in the granular bed for three different meshes are given in Tab. 5.1. It can seen in Fig. 5.1(b) that with increase in the level of refinement in the mesh size the pressure gradient converges to a pressure gradient value close to the modified Ergun's equation. In this study the remaining results generated are obtained using the coarse grid with 1 level grid refinement. In the next section, we verify the CFD model for different computational meshes.

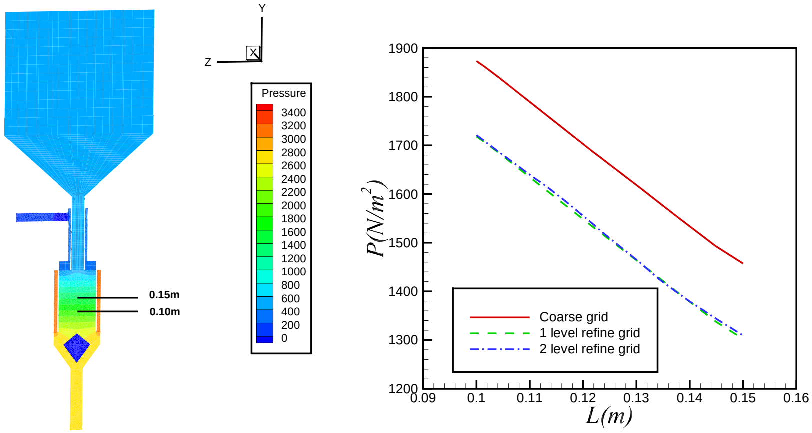

Figure 5.1 (a)Static Pressure contour for a static granular bed (b)Pressure drop along a section of granular bed.

### 5.4.2 Verification of UDFs and particle velocity model

The flow conditions for the test case chosen for verification of the particle velocity model implementation in ANSYS-FLUENT are mean slip Reynolds number $Re_m = 10$, granule volume fraction $\epsilon_s = 0.5$ and a particle Stokes number $St = 0.25$. Here the

Table 5.1 Pressure gradient along the bed

| **Condition** | **Values**($N/m^3$) | **No. of cells** |
|---|---|---|
| Modified Ergun's Eqn. | 8500 | |
| Coarse grid | 8447.7 | 24420 |
| Medium grid | 8468.6 | 79545 |
| Fine grid | 8468.6 | 195458 |

results obtained from the ANSYS-FLUENT simulations are compared with the DNS-LPT results. In the case of ANSYS-FLUENT the simulation setup is inflow at the inlet and pressure outlet, with periodic boundary condition on $y$ and $z$ direction. In the case of DNS-LPT simulations the fluid flow has periodic boundary conditions imposed in all three directions, and inflow and outflow boundary conditions on the particles (with periodic boundary conditions in $y$ and $z$ directions).

Table 5.2 Simulation conditions

| **Variables** | **DNS-LPT** | **FLUENT** |
|---|---|---|
| $\epsilon_s$ | 0.50 | 0.50 |
| $Re_m$ | 10 | 10 |
| $L/D_g$ | 4 | 8 |
| $St$ | 0.25 | 0.25 |

In Fig. 5.2(a) we can see that the difference between the particle velocity predicted by the fast Eulerian model and the fluid velocity implemented in ANSYS-FLUENT is very small, which indicates that the fast Eulerian model is not able to predict the slip velocity between the particle and fluid observed in DNS-LPT simulations(see Fig. 5.2(b)). This is one probable reason for the underprediction of the particle flux by ANSYS-FLUENT as seen in Fig. 5.3.

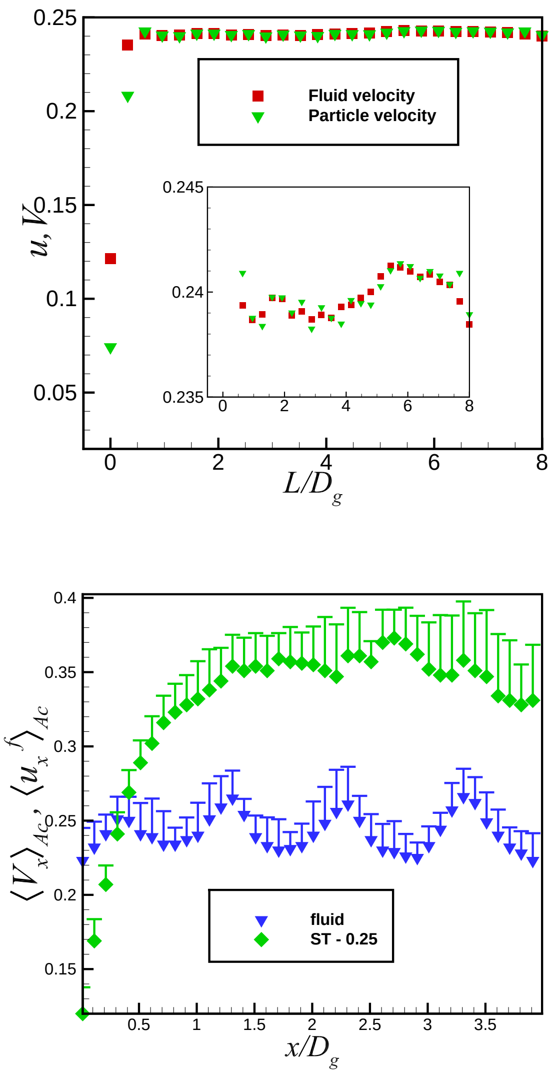

Figure 5.2 (a)Variation of fluid and particle velocity along the granular bed from ANSYS-FLUENT (b)Variation of mean particle velocity $\langle V \rangle_{A_c}$ from DNS-LPT for particle Stokes number 0.25 along the granular bed for a volume fraction 0.5 and Reynolds number 10 with particles initialized with fluid velocity and the mean fluid velocity $\langle u_f \rangle_{A_c}$ is shown for reference.

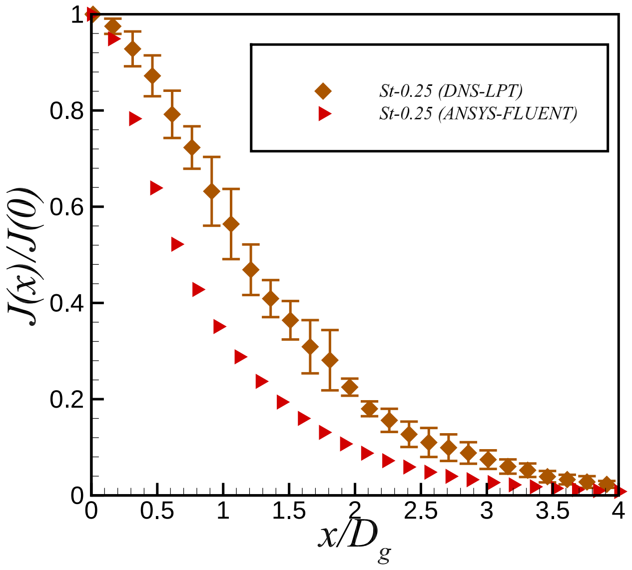

Figure 5.3 Steady state normalized particle flux $J(x)/J(0)$ along the flow domain for particle Stokes number 0.25 for a volume fraction 0.5 and Reynolds number 10 obtained from DNS-LPT and ANSYS-FLUENT.

### 5.4.3 Experimental setup

The dimensions of the moving bed granular filter experimental setup are given in Fig. 5.4(a). The flow conditions and the properties of the particles and granules are given in Tab. 5.3

More details on the experimental setup and the running conditions can be found in El-Hedok et al. (2011). The computational domain generated to represent the granular bed in shown in Fig. 5.4(b) and the computational domain was generated in ICEM-CFD.

### 5.4.4 Comparison with experiments

We simulated a case which is same as the experimental setup of El-Hedok et al. (2011). By using the filter dimensions and properties of char and granular material

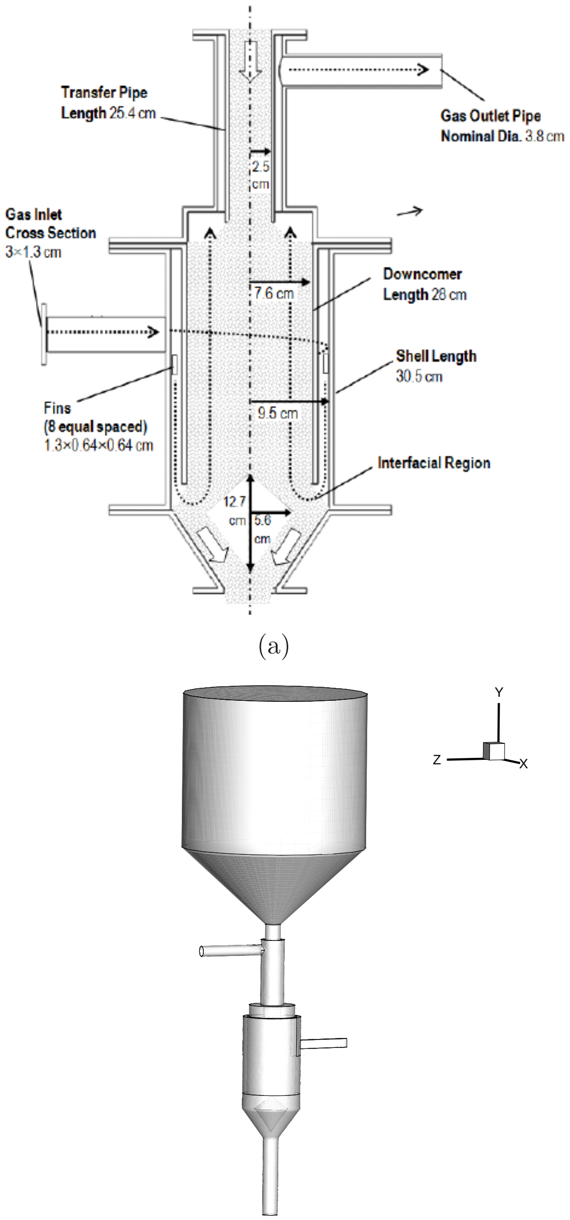

(a)

(b)

Figure 5.4 (a) Experimental setup of moving-bed granular filter (b)Three-dimensional model of moving-bed granular filter.

Table 5.3 Experimental conditions

| **Variables** | **Values** |
|---|---|
| $\epsilon_s$ | 0.63 |
| $Re_m$ | 70 |
| $D_g$ | $2 \times 10^{-3}$m |
| $d_p$ | $2 \times 10^{-5}$m |
| $\rho_p$ | 1200 kg/m$^3$ |
| $Q$ | 650 lpm |

given in Tab. 5.3, we estimate the gas inflow speed, char concentration at the inlet, and granule discharge speed. The inflow boundary conditions are given in Tab. 5.4. The accumulated char concentration on a slice along the axis of the granular bed is shown in Figs. 5.4.4. The char concentration contours shown in Figs. 5.4.4 are after operating the MBGF for 1 and 10 minutes. As one can observe in these Figures that with time the char accumulation is transported by the granular flow toward the granular outlet and eventually the granular bed starts to clog. The char contours in Figs. 5.4.4 gives us a qualitative comparison of the char concentration in the granular bed and also shows that the maximum concentration of char is observed in the interfacial region. The char accumulation with time obtained from the CFD simulation is compared with the experiments in Fig. 5.6. Overall the trends are consistent with the experiment, although the CFD predicts a higher char accumulation.

Table 5.4 Inflow boundary conditions

| **Variables** | **Values** |
|---|---|
| Fluid inlet | 30 m/s |
| Char concentration | $1.72 \times 10^{-6}$kg/m$^3$ |
| Granule discharge speed | $5.42 \times 10^{-3}$m/s |
| $\epsilon_s$ | 0.63 |

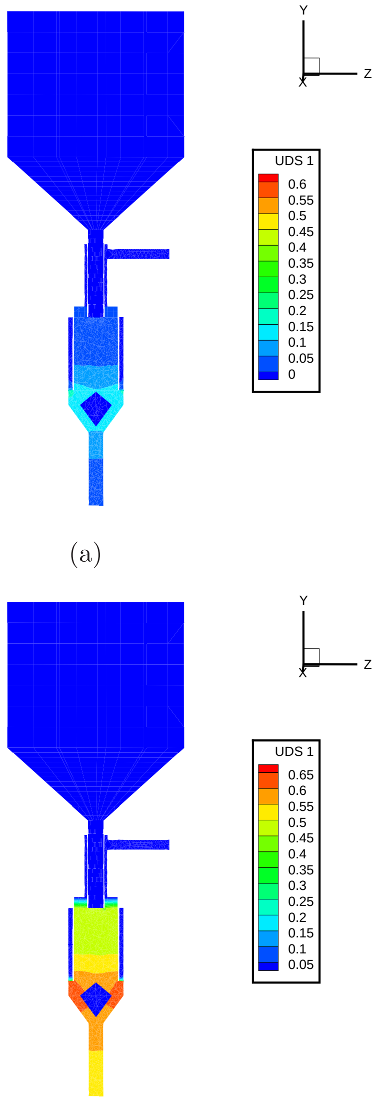

(a)

(b)

Figure 5.5 Char concentration along a section at $x = 0$ (a) after 1 minute (b) after 10 minutes.

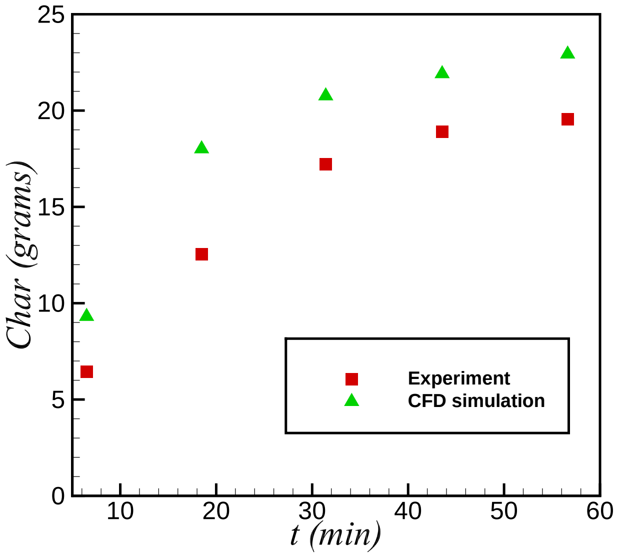

Figure 5.6 Char accumulation with time

## 5.5 Conclusions

A 3D CFD model is developed to simulate the full-scale MBGF. The model for filter coefficient obtained from the DNS-LPT is implemented in the CFD model along with the fast Eulerian model to calculate the particle velocity from fluid velocity. The CFD model give a good comparison of pressure gradient when compared with the modified Ergun's Equation for fixed bed. The char accumulation obtained from the CFD model gave a reasonable match with the experiments.

# CHAPTER 6. Modeling and Simulation of Sprays as Multiphase Flows

This chapter is a manuscript in review for International Journal of Spray and Combustion Dynamics :Modeling and Simulation of Sprays as Multiphase Flows authored by R. Kolakaluri,S. Subramaniam and Panchagnula, M. V..

## Abstract

The characteristic features of sprays pose unique challenges to multiphase flow methods that are used to model and simulate their behavior. This article reviews the principal modeling challenges posed by sprays, and discusses the capabilities of different modeling approaches by classifying them according to the basis of their statistical representation and the level of closure. This provides guidelines for their comparative assessment and also a perspective on the outlook for spray modeling. Multiphase flow simulation approaches that are used for spray computations are classified according to scale, accuracy, computational cost and problem complexity. The requirements of a simulation method to be successfully used for spray computation are then discussed. The review concludes with a perspective on the outlook for spray simulation methods.

## 6.1 Introduction

The purpose of this article is to review the principal challenges in modeling and simulation of sprays, and to summarize the progress made in addressing these challenges using current multiphase flow modeling approaches. Implications for the outlook of spray modeling and simulation methods are also outlined.

Sprays have found widespread application in many engineered systems owing to the simple, inexpensive and efficient manner in which interfacial area can be increased by several orders of magnitude. In these applications, the spray process is essential to enhancing transport of mass, momentum or energy. As simple a device as a spray nozzle is, the physics governing the breakup of the bulk liquid and subsequent transport is extremely complex. The primary breakup of the liquid into dispersed droplets and ligaments is a complicated phenomenon, and has been the topic of a recent review Gorokhovski and Herrmann (2008). The focus of this review is on modeling and simulation of the dispersed spray, and not on primary atomization. Some of the complexities encountered in the dispersed part of the spray are outlined hereunder in the context of spray combustion.

At the outset, the spray is a classical two-phase flow problem, which could also involve mass transfer from the drop phase to the continuous phase due to vaporization. In the case of reacting flows, there is also energy release and transport, which further enhances vaporization. This coupled nature of the transport phenomena makes spray combustion a problem that is both interesting and challenging.

Sprays are characterized by a wide range of droplet sizes and velocities. To illustrate this point, we consider data obtained from a typical Phase Doppler Particle Analyzer (PDPA) measurement in a hollow cone spray. Figures 6.1(a) and 6.1(b) show scatter plots of droplet size versus droplet velocity at two different locations in the spray. This dataset shows that the drop speeds and drop diameters at a given spatial location may vary over two orders of magnitude. This distribution of velocity and radius makes spray modeling a challenging problem because the *mean* velocity and radius are not adequate to characterize the complex spray-gas interaction. Later we will see that any statistical description of sprays must take this feature into account if it is to reproduce spray phenomena accurately. Figures 6.1(a) and 6.1(b) also reveal that the small drops have a wider range of velocity values as compared to the large drops. The correlation coefficient between size and velocity for the data shown in Fig. 6.1(a) is 0.326, and it is 0.473 for the data shown in Fig. 6.1(b). The scatter plots also indicate that the joint probability density function (pdf) of velocity and diameter is strongly dependent on spatial location within the spray.

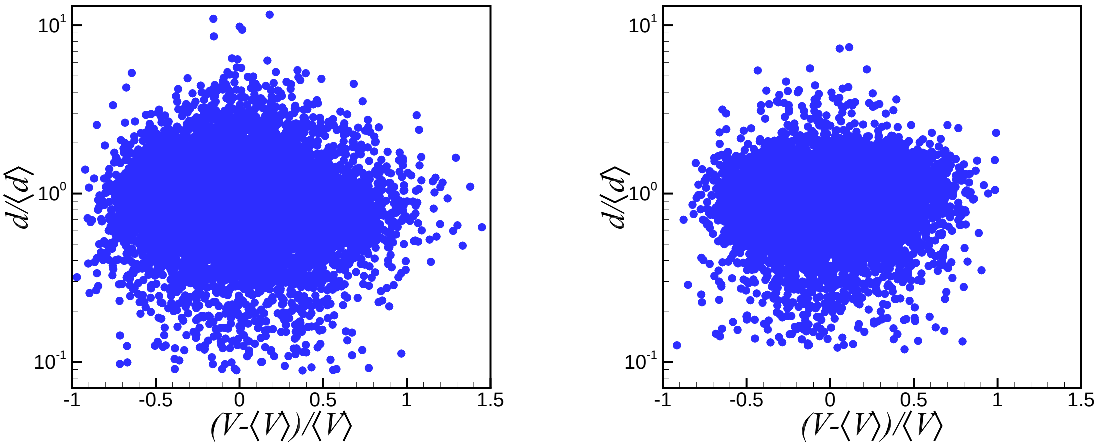

Figure 6.1 Scatter plot of drop diameter and drop velocity magnitude for a sample of 10000 drops in a hollow cone spray :(a) 12.5 mm downstream of the nozzle at the centerline (b) 25 mm downstream of the nozzle at the centerline.

Although statistical descriptions of velocity distributions using pdf's or moments are widely used in single–phase turbulent flows, there are some additional features that are peculiar to sprays which merit special attention. Figure 6.2 is a plot of droplet velocity vectors at two nearby spatial locations in the spray that are separated by 2 mm.

Each vector is colored based on the diameter of the drop (green and cyan indicates large drops and blue and red indicates small drops). Although the data at each location is not recorded simultaneously, the results indicate that the distribution of velocity and radius at a given spatial location (indicated by the black square box in Fig. 6.2) arises from the flux of droplets originating at different neighboring locations (in this example, from the two locations where the velocity vectors originate). This observation has two important consequences. The first is that, unlike the case of single-phase turbulence where momentum transfer at the level of a fluid particle at a given spatial location is diffusive (due to viscosity) at the small scales, the transfer of momentum in the dispersed phase in sprays can be kinetic (streaming) and collisional. Secondly, the presence of a distribution of droplet velocities in an arbitrarily small spatial neighborhood of a single spatial location arising from a kinetic transport mechanism results in a phenomenon termed *polykineticity*. In its simplest setting, one can imagine the possibility of the droplet velocity having arbitrarily large changes in magnitude (and sign) in an infinitesimal spatial neighborhood because of two dilute droplet streams crossing each other Desjardins et al. (2008). As seen in Fig. 6.2, there is a high degree of polykineticity in this spray, both in magnitude and direction. These aspects distinguish spray modeling from standard single-phase turbulence modeling. Although there is a similar distribution of fluid particle velocity in single–phase turbulence, in that case the random velocity field is continuous and differentiable because the fluid particle is a continuum concept that is affected by viscous diffusion at the small scales. The Reynolds–averaged equations for mean and higher moments in single-phase turbulence retain the diffusive nature of the Navier–Stokes (NS) equations that govern a realization of the fluid velocity field. On the other hand, in the case of sprays the transport equation for the velocity distribution (see Sec. 6.3.2) is governed by kinetic and collisional terms. The averaged moment equations derived from this transport equation will have a viscous diffusive term only if there is separation of scales and the collisional term dominates.

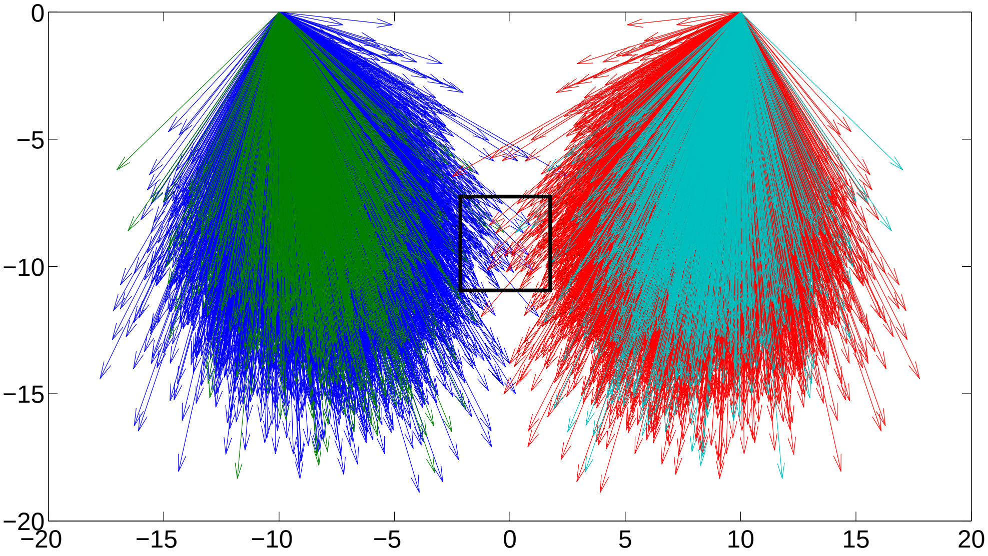

Figure 6.2 Plot indicating velocity vectors at a point in the spray for a sample of 10000 drops. The velocity vectors are colored green and cyan for large drops and blue and red for small drops.

Figure 6.2 also shows that the larger drops have a preferential direction of movement that is different from the smaller drops. Capturing this size-dependent velocity is important for accurate prediction of drop dispersion. With these observations as the background, we would like to emphasize that any spray model should be able to handle polydispersity, size–velocity correlation, and polykineticity. In addition, spray velocity distributions are not equilibrium (Maxwellian) distributions. The nonlinear, non-equilibrium, polydisperse and polykinetic characteristics of sprays pose modeling challenges that are elaborated in further detail in Section 6.2.

Fully–resolved direct numerical simulation (DNS) Helenbrook and Edwards (2002); Quan et al. (2009); Dwyer et al. (1994) of liquid droplets in an ambient gas, wherein boundary conditions are imposed on each droplet's surface and all flow features around each droplet are fully resolved, offer a high–fidelity representation of droplet-gas interaction that requires no models at the continuum level (the final stage of droplet breakup still has to be modeled). However, such computations are very demanding and not practical for spray applications. Nevertheless, such DNS studies are very useful for model development, as seen in gas-solid flows Tenneti and Subramaniam (2013); Tenneti et al. (2011, 2013b). In order to estimate the complexity of solving a realistic spray problem using DNS, let us consider the spray from a typical airblast atomizer that flows about 10 kg/hr of Jet-A while producing drops with a mean diameter on the order of $50\mu$m. This corresponds to a drop number flux of $\approx 10^7$ drops per second. For realistic domain sizes and simulation time intervals, the number of drops that need to be accounted for could easily be $O(10^9)$. Clearly droplet-resolved simulations of such a large problem is not only computationally challenging, but also unnecessary for device–scale simulations.

Statistical descriptions of multiphase flow are useful to engineers because of the need to reduce the amount of information obtained from a single realization of a spray, to the essential quantities that are relevant for engineering design. Multiphase flow modeling approaches are usually classified as Lagrangian-Eulerian (LE) or Eulerian-Eulerian (EE), but this terminology is misleading because the same statistical modeling approach can lead to equations that are solved in either the Lagrangian or Eulerian frame of reference Pai and Subramaniam (2009). A more useful classification is based on the statistical representation of multiphase flow that is used to develop the model, rather than the frame of reference employed to solve the resulting model equations. This leads to a classification based on the *random–field* and *stochastic point process* approaches that are described in Section 6.3. These and other spray modeling approaches described in Sec. 6.3 have varying levels of capability in addressing the modeling challenges posed by sprays. These are compared in Sec. 6.3.3.

The spray modeling approaches described in Sec. 6.3 lead to model equations that are simulated using a wide range of methods, and these are discussed in Sec. 6.4. The principal requirements of spray simulations are then outlined in Sec. 6.4.2. The utility of various simulation approaches is reviewed from the standpoint of a tradeoff of accuracy and computational cost. Finally, the principal findings of this review are summarized in Sec. 6.5.

## 6.2 Challenges in modeling sprays

As mentioned before, modeling sprays is challenging because they are characterized by:

1. Wide range of volume fraction and droplet Knudsen number.
2. Randomness in the configuration of the dispersed phase.
3. Nonlinearities such as drag dependence on the droplet velocity.
4. Polydispersity and size–velocity correlation.
5. Multiscale interactions.
6. Polykineticity.
7. Nonequilibrium effects that lead to phenomena such as preferential concentration and clustering.

All these can have a significant impact on the design and performance of spray devices in various applications. These challenges and the associated physics will be discussed next.

### 6.2.1 Wide range of volume fraction and droplet Knudsen number

Sprays are characterized by volume flux variations of more than one order of magnitude over the visible part of a spray. For the case where the drops of all sizes are moving with nearly the same mean velocity, the variations of volume flux and volume fraction would be the same. In general, where this may not be true, normalized volume flux and volume fractions are independent measurements. Figure 6.3 is a plot of normalized volume flux in a hollow cone spray versus radial dimension. The plot indicates the variation at two axial locations of 12.5mm and 25mm. Firstly, it can be seen from fig 3 that the normalized volume flux varies over an order of magnitude in the spray. As can be seen in Fig. 6.3, the volume flux (and other macroscopic spray parameters) vary on a length scale ≈ 1mm. This has direct implications to the calculation of mean free path, which is discussed below.

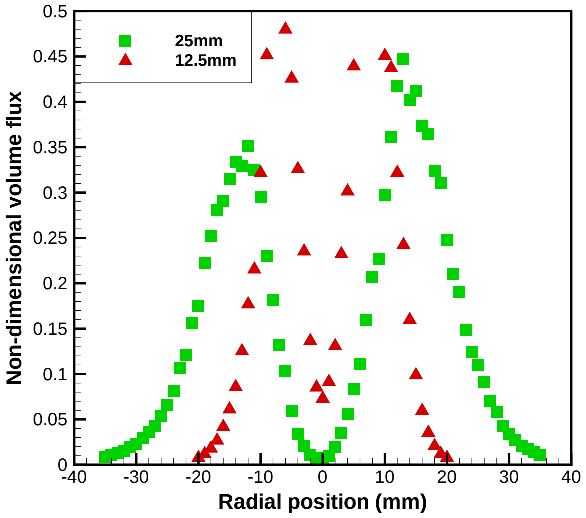

Figure 6.3 Liquid volume flux at 12.5 and 25 mm downstream of the nozzle exit at the centerline.

Figure 6.4 is a plot of the pdf of a non-dimensional free path estimator. The free path estimator is defined as the pair-wise spacing between drops and is an indicator of the conventionally defined free path. This free path estimator was calculated from the pair-wise time spacing and the relative velocity between a pair of drops arriving successively in a PDPA measurement volume. The symbols in Fig. 6.4 are from the experimental PDPA data while the solid line is a best fit lognormal distribution. It is interesting to note that the drop spacing exhibits the characteristic long-tailed distribution similar to drop size. Also, the mean of the distribution is skewed by the large values owing to the long tail. This may have interesting implications in the definition of a *mean* free path. The Knudsen number (defined as the ratio of the mean free path $\lambda$ to

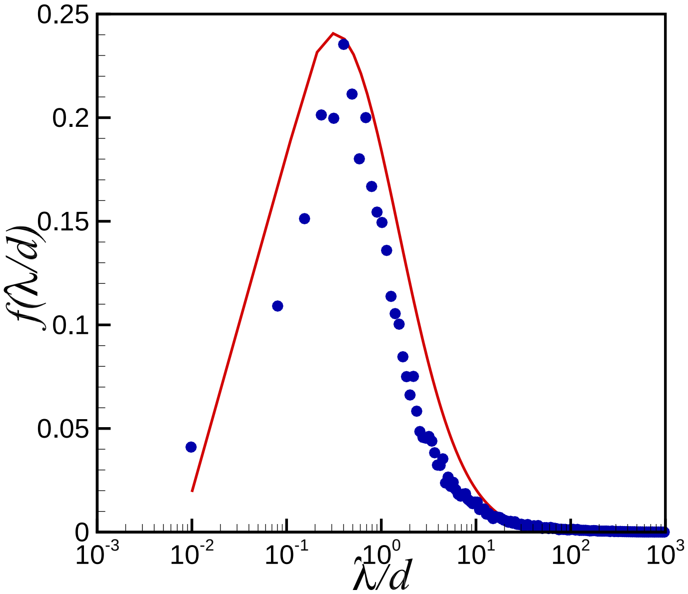

Figure 6.4 Probability density function of droplet free path estimator at 25 mm downstream of the nozzle exit at the centerline: data from PDPA measurement and line is the best fit lognormal distribution.

a length scale $L$ that is characteristic of the variation of mean quantities) is used to quantify the separation of macro from microscales. The length scale $L$ associated with the gradient of the volume flux along the radial position (Fig. 6.3) is used to calculate the Knudsen number in Fig. 6.5. Although continuum fields may be meaningfully defined in terms of ensemble averages for any liquid volume fraction Drew and Passman (1998), the separation of scales $\lambda \ll L$ is crucial for the development of continuum balance equations. If in addition, the flow is collision dominated, then standard kinetic theory treatments apply and the Chapman-Enskog (CE) closure approximations can be employed for low Knudsen number ($Kn < 0.1$ is usually taken as the limit for NS equations to apply in a continuum description of the liquid phase Oran et al. (1998)). Higher Knudsen numbers ($0.1 < Kn < 1.0$) are classified as the 'slip regime' (NS equations may be applied with partial-slip boundary condition at walls Beskok and Karniadakis (1996)), while $Kn > 1.0$ is usually considered as dominated by free–molecule transport.

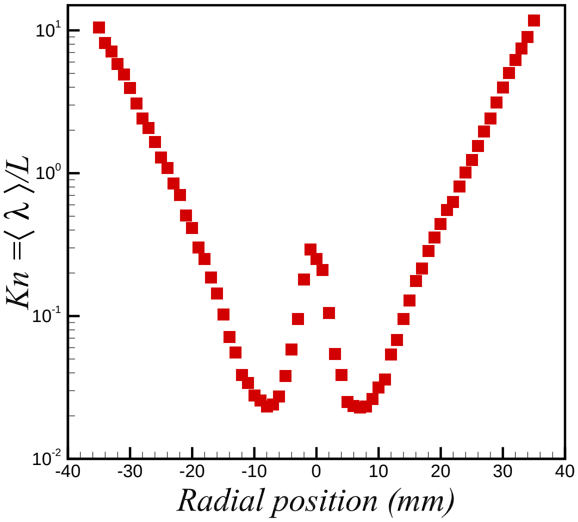

Figure 6.5 Variation of droplet Knudsen number with radial location in the hollow cone spray.

The Knudsen number based on the non-dimensional mean free path estimator is calculated from point-wise data and plotted in Fig. 6.5 as a function of radial position. As can be seen, this quantity varies over two orders of magnitude. This brings into glaring view one of the central complexities in spray modeling, that the droplets can be represented as a continuum at the spray core while at the edges they must be treated as a rarefied gas. Similar observations have been reported from simulation of dilute gas-solid flows in risers Passalacqua et al. (2010). Any model invoked to model spray distribution must asymptote to these limits in the appropriate physical regions.

We also estimated the mean free path using two standard kinetic theory formulae ($\lambda = 1/\sqrt{2}nd^2\pi$ Liboff (2003) and $\nu = GT_{tr}^{1/2}$ Luding et al. (1998)) where $n$ is the droplet number density, $d$ is the droplet diameter, $\nu$ is the Enskog collision frequency, $T_{tr}$ is the granular temperature, $G = 8d^2ng(d)\sqrt{\pi/m}$, $m$ is the mass of the droplet, and $g(d)$ is the radial distribution function at contact. The mean free path obtained from these estimates are approximately 0.19m for our estimates of the droplet number density and granular temperature from droplet velocity variance. This estimate is almost 170 times greater than the average of the free path estimator plotted in Fig. 6.4. Although it is difficult to arrive at a definitive conclusion concerning the magnitude of the mean free path because of the assumption involved in both calculations, our free path estimator is conservative in terms of delineating the range of validity of the continuum model of sprays.

In regions of high volume fraction the local Knudsen number may be less than 0.1, but the Knudsen number can be large if either the flow is dilute, or the (droplet) Mach number is large Passalacqua et al. (2010). The latter consideration follows from the usual practice of estimating the magnitude of the pair relative velocity using the granular temperature in homogeneous granular flows, but the droplet velocity covariance may be a poor estimate of the pair relative velocity magnitude in sprays. An additional consideration is that for high volume fraction, which for sprays corresponds to high mass loading, two-way momentum coupling of the carrier and dispersed phases needs to be taken into account.

### 6.2.2 Randomness in configuration of the dispersed phase

The statistical variability inherent in sprays that was noted earlier necessitates statistical models. The positions and velocities of the spray droplets can be modeled as random vectors. An important characteristic of sprays is the correlation of droplet velocity with spatial location, and representing this joint dependence is important for accurate calculation of spray and gas dynamics. Fluctuations in droplet velocity arise from momentum exchange with the carrier gas and from collisions with neighboring droplets. The nonlinear dependence of droplet acceleration on droplet velocity outside the Stokes flow regime (based on droplet Reynolds number) implies that for accurate representation of interphase momentum transfer it is not sufficient to merely represent the spray by the average drop diameter.

### 6.2.3 Nonlinearities such as drag dependence on velocity distribution

In addition to the nonlinearity of the NS equations governing the gas phase dynamics, the inertia of spray droplets results in a nonlinear dependence on droplet velocity, when the droplet Reynolds number $Re_d > 1$. The droplet Reynolds number is defined as $Re_d = |\langle W \rangle| d/\nu$, where $|\langle W \rangle|$ is the slip velocity between the droplet and gas, $d$ is the droplet diameter, and $\nu$ is the kinematic viscocity. The momentum transfer due to drag between gas and droplets is characterized by a drag law Schiller and Naumann (1933); A. A. Amsden, and P. J. O'Rourke, and T. D. Butler (1989). Even for monodisperse droplets, the distribution of droplet velocities implies that the mean momentum exchanged by the droplets with the gas is not the momentum exchange evaluated at the mean droplet velocity. As droplets evaporate, their size and inertia decrease, and this couples energy balance to mass and momentum balance equation Dwyer and Dandy (1990); Dwyer (1989). To illustrate this point, Fig. 6.6 shows a scatter plot of fully–resolved direct numerical simulation (FR-DNS) data of the acceleration of monodisperse solid particles plotted versus their velocity. This nonlinear dependence of acceleration or drag on velocity can be seen in Fig 6.6 for both the data obtained from FR-DNS and also the instantaneous drag law. However the FR-DNS data also shows the origins of the randomness in the dispersed phase configuration, which is not captured by the simple extension of a mean drag law Tenneti et al. (2010); Garzò et al. (2012).

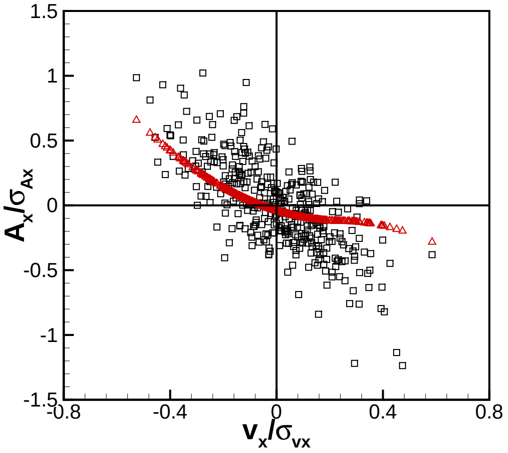

Figure 6.6 Scatter plot of streamwise component of acceleration versus the streamwise component of velocity. Square symbols (□) show acceleration obtained from FR-DNS Tenneti et al. (2010) of steady flow past a homogeneous fixed assembly of particles for mean flow Reynolds number 20 and a solid volume fraction of 0.2, while the upper triangles(△) show the acceleration predicted by simple extension of a mean drag law Hill et al. (2001b).

### 6.2.4 Polydispersity and size-velocity correlation

Droplet size influences heat, mass and momentum exchange with the carrier gas. In order to accurately capture the mean interphase momentum, mass and heat transfer terms, spray models must incorporate the size *distribution* of droplets. As noted earlier, the size-velocity correlation is significant in sprays (cf. Fig. 6.1) and since these interphase exchange terms also depend strongly on the droplet size and velocity, it is necessary that models capture this joint size-velocity dependence accurately. The other aspect of polydispersity is that it introduces an additional range of length and time scales into the spray problem. Figure 6.7 shows fluid velocity contours and particle velocity in a freely evolving bidisperse gas-solid flow to illustrate this point.

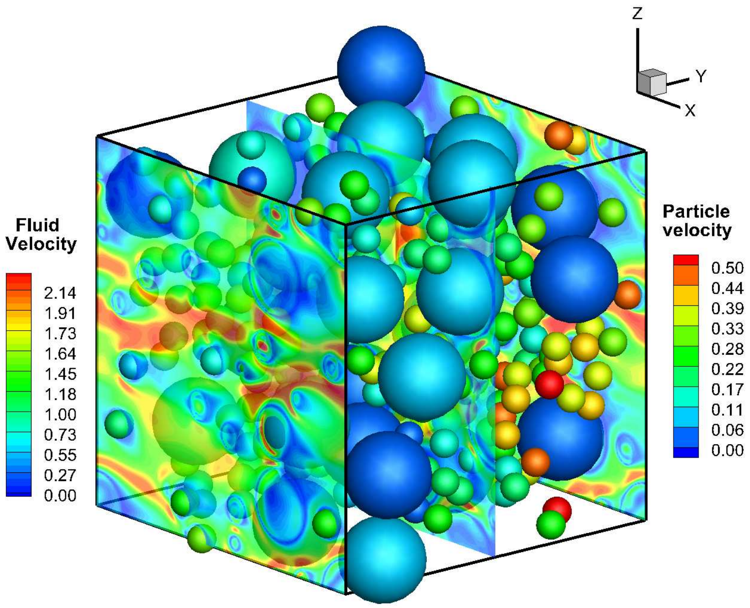

Figure 6.7 Contours of fluid and particle velocity in a freely evolving bidisperse gas-solid flow for a mean particle Reynolds number of 50 and a particle volume fraction of 0.3.

### 6.2.5 Multiscale interactions

Monodisperse particles or droplets interacting with a turbulent carrier-phase that is inherently multiscale in nature is itself a complex problem that poses formidable modeling challenges Pai and Subramaniam (2006); Xu and Subramaniam (2006); Pai and Subramaniam (2012). The presence of a wide range of length and time scales in both the carrier and dispersed phase poses a significant modeling challenge in multiphase flows. The specific issues associated with this challenge will be discussed hereunder.

#### 6.2.5.1 Dispersed phase interactions with turbulence

Turbulence in the carrier phase results in a range of length and time scales. In fact, even laminar multiphase flows can exhibit significant levels of non–turbulent velocity fluctuations with a range of length and time scales, as recently shown by FR–DNS of Tenneti et al. Tenneti et al. (2013a). The density difference between the dispersed and carrier phases results in droplets having higher inertia than fluid material volumes or eddies of the same size. Therefore, dispersed phase droplets may interact dynamically and exchange momentum with fluid eddies that are much larger in size Pai and Subramaniam (2007). The droplet momentum response time can be used to calculate the size of a turbulent eddy in the inertial sub–range with the same eddy turnover time. This in turn can be used to define a range of eddy length scales with which the dispersed phase may interact dynamically Pai and Subramaniam (2006, 2007). It should also be noted that the droplets may not exchange momentum over the same time scale with eddies of all sizes in the carrier–fluid turbulent kinetic energy spectrum. These observations motivate the development of multiscale interaction models for droplet acceleration.

#### 6.2.5.2 Scales of structures in dispersed phase

It was already noted that the range of free path distribution in sprays can result in a wide variation in the droplet Knudsen number, resulting in lack of separation between micro and macroscales in regions of high Knudsen number. Further evidence of this lack of scale separation in multiphase flows is obtained from FR–DNS of heat transfer in gas-solid flows where it is found that fluid heating (or cooling) by particles can result in the mean fluid temperature varying on scales comparable to the mesoscale spatial structure of particles (see Fig. 6.8). This lack of scale separation has implications for modeling.

Models that are local in physical space are strictly valid only if the characteristic length scale of variation of mean quantities (macroscale denoted by $\ell_{\text{macro}}$) is always greater than a characteristic length scale $\ell_{\text{meso}}$ associated with the pair correlation of particles or droplets. (Usually the characteristic length scale of the pair correlation function is on the order of $1-10$ droplet diameters, although in clustered or preferentially concentrated flows it could be higher.) This is because if scale separation does not exist and $\ell_{\text{meso}} \sim \ell_{\text{macro}}$, then surface phenomena such as heat transfer and vaporization occurring at a distance $\ell_{\text{meso}}$ from the physical location $\mathbf{x}$ would affect the evolution of mean fields at $\mathbf{x}$. In the current scenario, all multiphase models are of the local type.

Multiscale interactions are responsible for phenomena like preferential concentration and clustering that affect interphase transfer processes of momentum, heat and mass between the carrier and dispersed phases Breault and Guenther (2009). At the microscale, the acceleration, heat and mass transfer experienced by individual droplets can be affected by their being deep inside a group or cluster of droplets, or in a relatively isolated location. In fact, Chiu and coworkers delineated several modes of droplet combustion based on their group behavior Chiu et al. (1982); Chiu and Su (1997); Chiu and Liu (1977). Preferential concentration of $O(1)$ Stokes number particles or droplets in low vorticity regions of turbulent flow leads to the formation of mesoscale structures Eaton and Fessler (1994); Squires and Eaton (1991c). In gas–solid flows it is also reported that the average drag experienced by the solid particles can depend significantly on the presence of clusters Mckeen and Pugsley (2003); Garg et al. (2010a). It follows that the interphase source terms in the carrier phase that represent momentum coupling should also account for this multiscale interaction.

### 6.2.6 Polykineticity

As mentioned earlier, sharp changes in the droplet phase velocity over very short distances is a complicating feature of any spray. In order to understand the intricacies,

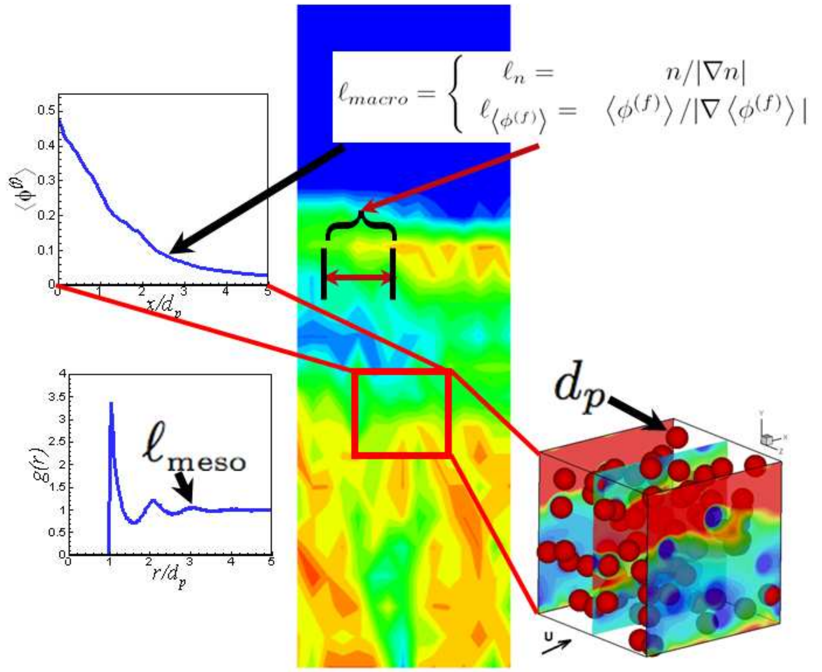

Figure 6.8 Scale of structures in the dispersed and carrier phases. Macroscale structures correspond to gradients of the number density of the dispersed phase and scaled gas-phase mean temperature shown here for a gas–solid flow in a central-jet fluidized bed. FR-DNS reveals that the scale of variation of the scaled gas-phase mean temperature is on the order of a few particle diameters (top left panel), while the pair correlation of particles (bottom left panel) reveals that the scale of mesoscale structures in the solid phase is also on the same order (2−4 particle diameters). The microscale corresponds to length scales on the order of a particle diameter, as shown in the FR-DNS simulation with contours of fluid velocity in the right panel.

let us consider the limiting regions discussed in Fig. 6.5, where the Knudsen number was shown to vary over two orders of magnitude. In the dense spray region, where $Kn$ is small, the high frequency of droplet collisions acts as a momentum diffusion mechanism erasing sharp velocity gradients in the droplet phase. This is akin to the kinetic theoretic origins of viscosity. However, as we transition to the rarefied gas regime, the possibility of sharp gradients in the velocity field is increased. This is best explained by the canonical problem of crossing jets where two dilute particle laden jets would cross each other Desjardins et al. (2008), if the collision frequency is sufficiently small. As the particle volume fraction is increased, the jets exhibit increased momentum diffusion finally resulting in a coalesced jet for the case of a dense particulate jet. This transition region is of interest to sprays as most of the volume flux in the spray would fall in this region of Knudsen number.

This transition regime is characterized by the droplet phase velocity being non-unique. Typically, this is handled by invoking a multivelocity model Williams (1958) similar in principle to the Boltzmann equation. In this approach, the velocity of the particulate phase is treated as an independent variable and locally allowing the droplets to manifest a probability distribution in this variable. Typical NS (deterministic) modeling approach would suggest that this distribution be a dirac-delta function. We will revisit this proposition when we discuss the population balance method.

### 6.2.7 Nonequilibrium characteristics of the droplet velocity pdf

In sprays and gas-solid flow in risers, the particle Stokes [1] and Knudsen numbers [2] span a wide range resulting in velocity distributions that can be far from the equilibrium Maxwellian distribution that arises from elastic collisions in the collision–dominated low

---

[1] The particle or droplet Stokes number is the ratio of the particle momentum response time to a characteristic flow time scale.

[2] The particle or droplet Knudsen number is the ratio of the mean free path of a particle to a characteristic length scale associated with the variation of the average number density field.

Knudsen number regime. This is because these velocity distributions are not always equilibrated by collisions but can be dominated by transport Fox (2012). In such cases, accurate representation of the non-equilibrium velocity distribution can be important for predictive spray modeling.

### 6.2.8 Requirements of multiphase models

Given the aforementioned complexities in modeling sprays, it is useful to first lay out the primary requirements of a robust model.

1. *Mathematical representation that is capable of representing the physical phenomena of interest*:

   One of the key challenges in statistical models is knowledge of what constitutes an *adequate* level of description to accurately describe physical phenomena of interest. For instance, in the case of single–phase turbulent flows, a statistical closure at the level of the mean velocities and Reynolds stresses (second moment closure) is often adequate for nonreacting flows, but closure at the joint probability density of composition Pope (1985, 2000); Fox (2003); Libby and Williams (1993) is required for reacting flows with temperature-dependent Arrhenius-type reactions. Similarly, in the case of sprays the mathematical representation must be adequate to represent the principal phenomena of interest, such as size-velocity correlation.

2. *Accurate and consistent models for the unclosed terms that need to be modeled*:

   As described in Section 6.3, there are two principal spray modeling approaches, commonly referred to as LE and EE in the literature Subramaniam (2013). There are consistency conditions that arising from the equivalence between these two descriptions, and therefore models developed in either approach should be consistent with the implied moment closures in both approaches Pai and Subramaniam

(2009). The models should also be Galilean–invariant Subramaniam (2013). Finally, all spray sub–models should be formulated such that they are independent of numerical parameters, for only then can numerically convergent solutions be expected.

3. *Ability to represent complex geometry*:

   The wide variety of application areas in which sprays are encountered often employ devices with complex geometries. In order to understand and analyze spray characteristics and optimize designs it is important to represent the complex geometrical features of these applications. Therefore spray simulation codes need to have the capability to represent complex geometry in order to be useful in design optimization of spray devices.

## 6.3 Multiphase Flow Models

As shown in Fig. 6.9, the two principal approaches used to model multiphase flows are: (i) the *random field* approach in which both dispersed and carrier phases are represented as random fields in the Eulerian frame, and (ii) the *stochastic point process* approach in which the dispersed phase is represented as a stochastic point process in the Lagrangian frame and the carrier phase is represented as a random field in the Eulerian frame. The random field approach at the closure level of moments leads to the EE two–fluid theory in its ensemble–averaged Drew (1983); Drew and Passman (1998) and volume–averaged variants Ishii (1975). Polydispersity in such approaches can be modeled using the sectional method in an Eulerian frame Greenberg et al. (1986, 1993), where the continuous size distribution is approximated by a finite number of size classes corresponding to the average diameter in an interval. The sectional approach Laurent et al. (2004b); Laurent and Massot (2001) has been derived rigorously starting from a kinetic description based on Williams' transport equation for the ddf Laurent et al. (2004a) and is sometimes also referred to as the multi-fluid approach [3].

The LE or Euler–Lagrange approach corresponds to a closure of the stochastic point process representation at the level of the droplet distribution function (ddf) or number density function (NDF), with the carrier phase being represented in an Eulerian frame through a Reynolds–averaged Navier–Stokes (RANS) closure, Large Eddy Simulation (LES) or Direct Numerical Simulation (DNS) (see Fig. 6.9). Fox Fox (2012) notes that a mesoscopic description of the dispersed phase in terms of the kinetic equation governing the NDF evolution is the preferred approach for physics–based modeling of multiphase flows.

### 6.3.1 Random–field description

In statistical theories of turbulent single-phase flow, the Eulerian velocity field is represented as a random vector field Pope (2000). A similar approach can be adopted for two–phase flows, but in addition to the velocity (and pressure) field it is also necessary to specify the location and shape of the dispersed-phase elements. The velocity field $\mathbf{U}(\mathbf{x}, t; \omega)$, which is defined in both thermodynamic phases, is a vector field that is defined at each point $\mathbf{x}$ in the flow domain in physical space, on the $\omega$th realization. The dispersed–phase elements in that same realization are similarly described by a dispersed–phase indicator *field* $I_d(\mathbf{x}, t; \omega)$, which is unity for all points inside the dispersed–phase elements that are contained in the flow domain, and zero outside. Statistical theories based on random–field representations can be formulated using multipoint joint probability density functions, but these have not resulted in tractable engineering models even for single–phase turbulent flow  Pope (2000); Monin and Yaglom (1975); Hopf (1952).

---

[3] However, the term multi–fluid is also used to describe a slightly different approach that extends the two–fluid model to multiple size classes in gas–solid flow Syamlal et al. (1993)

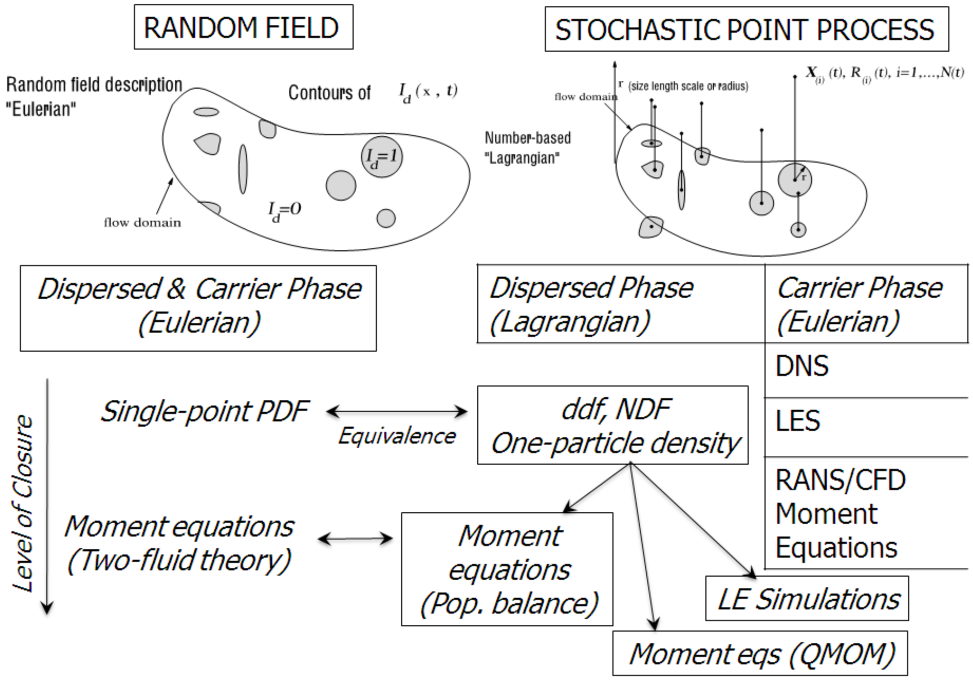

Figure 6.9 Representations of multiphase flow as random field or a stochastic point process embedded in a random field, leading to the EE and LE approaches, respectively. The equivalence between these approaches is indicated.

#### 6.3.1.1 Two–fluid theory

If statistical information at only a single space–time location $(\mathbf{x}, t)$ of the random–field representation is considered, this results in a single–point EE two–fluid theory. In this case, the statistics of the velocity field $\mathbf{U}(\mathbf{x}, t; \omega)$, and the dispersed–phase indicator field $I_d(\mathbf{x}, t; \omega)$, are considered at a single space–time location, i.e., the indicator *field* reduces to an indicator *function*. The velocity and indicator function can be treated as random variables (or random vector in the case of velocity) *parametrized* by space and time variables. The averaged equations resulting from this approach are described in Drew Drew (1983), and Drew and Passman Drew and Passman (1998). The single–point EE theory can also be developed at the more fundamental level of probability density functions also, and this theory is developed by Pai and Subramaniam Pai and Subramaniam (2009).

### 6.3.2 Lagrangian representation of the dispersed phase

An alternative approach is to describe the dispersed–phase consisting of $N_s$ solid particles or spray droplets using Lagrangian coordinates $\{\mathbf{X}^{(i)}(t), \mathbf{V}^{(i)}(t), R^{(i)}(t), i = 1, \dots, N_s(t)\}$, where $\mathbf{X}^{(i)}(t)$ denotes the $i^{th}$ dispersed–phase element's position at time $t$, $\mathbf{V}^{(i)}(t)$ represents its velocity, and $R^{(i)}(t)$ its radius. The rigorous development of a statistical theory of multiphase flows Subramaniam (2000b) using the Lagrangian approach relies on the *theory of stochastic point processes* Daley and Vere-Jones (1988), which is considerably different from the *theory of random fields* Pope (2000); Panchev (1971); Adler (1981) that forms the basis for the EE approach. The representation of sprays using a stochastic point process and the definition of the ddf have been discussed in detail elsewhere Subramaniam (2000b, 2001b, 2013). Starting from the definition of the ddf, one can derive William's spray equation Subramaniam (2001b), which is the following collisional form of the ddf evolution equation:

$$\begin{aligned}\frac{\partial f}{\partial t} + \frac{\partial}{\partial x_k}[v_k f] + \frac{\partial}{\partial v_k}\left[\langle A_k|\mathbf{x},\mathbf{v},r;t\rangle f\right] \\ + \frac{\partial}{\partial r}\left[\langle \Theta|\mathbf{x},\mathbf{v},r;t\rangle f\right] = \dot{f}_{\text{coll}} + \dot{f}_{\text{coal}} + \dot{f}_{\text{bu}}.\end{aligned} \tag{6.1}$$

In the above equation $\langle A_k|\mathbf{x},\mathbf{v},r;t\rangle$ represents the expected acceleration conditional on the location $[\,\mathbf{x},\mathbf{v},r]$ in phase space. Similarly $\langle \Theta|\mathbf{x},\mathbf{v},r;t\rangle$ represents the expected rate of change of radius (hereafter referred to as the expected vaporization rate) conditional on the location $[\,\mathbf{x},\mathbf{v},r]$ in phase space.

#### 6.3.2.1 LE approach

In typical implementations of the LE approach (e.g., the KIVA family of codes A. A. Amsden, and P. J. O'Rourke, and T. D. Butler (1989); Amsden (1993)) a solution method based on computational particles is used to indirectly solve for the ddf evolution, while the gas–phase is represented using a RANS model Subramaniam (2013). Interphase coupling is accounted for by source terms that appear in the Eulerian gas–phase conservation equations for mass, momentum and energy. These source terms are computed from computational particle properties using a statistical estimator Garg et al. (2007, 2009); Subramaniam (2013).

#### 6.3.2.2 Population balance modeling

The population balance concept was first presented by Hulburt and Katz Hulburt and Katz (1964), and the model derivation was based on the Boltzmann-type equation and the problems treated are particle nucleation, growth and agglomeration. We use a similar approach, where the droplets are described using a one-particle distribution function $f(\mathbf{x},\mathbf{v},r,t)$, where the one-particle distribution function gives us the probability of the number of droplets. The evolution of $f(\mathbf{x},\mathbf{v},r,t)$ is influenced by (i) convective transport, (ii) nucleation and organic growth, (iii) external force fields, (iv) collision and the resulting exchange of momentum, (v) breakup and (vi) coalescence. The associated physics of these phenomena is modeled in a population balance framework. In this framework, microscopic droplet processes, for example, collision, breakup and agglomeration are introduced into a macroscale transport model through a set of constitutive kernel functions. These kernel functions capture the microscopic physics in a statistical sense and influence the macroscopic evolution of $f(\mathbf{x}, \mathbf{v}, r, t)$.

In this context the evolution of the one-particle distribution function $f(\mathbf{x}, \mathbf{v}, r, t)$ is given by

$$\begin{aligned}\frac{\partial f}{\partial t} + \frac{\partial}{\partial x_k}[v_k f] + \frac{\partial}{\partial v_k}\left[\langle A_k|\mathbf{x}, \mathbf{v}, r; t\rangle f\right] + \frac{\partial}{\partial r}\left[\langle \Theta|\mathbf{x}, \mathbf{v}, r; t\rangle f\right]& \\ = \mathbb{C} + B_B - D_B + B_C - D_C,& \qquad (6.2)\end{aligned}$$

where the birth and death of droplet $r$ due to breakup and coalescence respectively are :

$$B_B = \int_r^\infty \beta(r \mid r_j)\Gamma(f, \mathbf{v}, r_j) f(\mathbf{x}, \mathbf{v}, r_j, t)\, dr_j, \qquad (6.3)$$

$$D_B = \Gamma(f, \mathbf{v}, r) f(\mathbf{x}, \mathbf{v}, r, t), \qquad (6.4)$$

$$B_C = \frac{1}{2}\int_0^r a\left[(r^3 - r_j^3)^{1/3}, r_j\right] f(\mathbf{x}, \mathbf{v}, (r^3 - r_j^3)^{1/3}, t) f(\mathbf{x}, \mathbf{v}, r_j, t)\, dr_j, \qquad (6.5)$$

$$D_C = \int_0^\infty a\left(r, r_j\right) f(\mathbf{x}, \mathbf{v}, r, t) f(\mathbf{x}, \mathbf{v}, r_j, t)\, dr_j. \qquad (6.6)$$

The issues involving the LHS of Eq. 6.2 have been discussed elsewhere Fox (2012). The specific issue we will focus on in this section relates to handling the evolution of polydispersity and polykineticity, which will be handled in a population balance framework and are represented as the RHS of Eq. 6.2. The first term on the RHS, $\mathbb{C}$ is the inelastic Boltzmann collision integral discussed in detail by Fox and Vedula Fox and Vedula (2010). In the CE limit, to O($Kn$) ($Kn$ is the particle Knudsen number), this integral gives rise to a gradient diffusion of $f$ in the velocity co-ordinate. The microscale physics of drop breakage or drop-drop agglomeration is handled through a set of three stochastic kernel functions. Firstly, $\Gamma(f, \mathbf{v}, r)$ indicates the breakup frequency of a drop of radius $r$ with a distribution function, $f$. The second function, $\beta(r|r_j)$ is the probability kernel of a drop of radius $r$ forming from a breakup event of drop with radius $r_j$. This kernel is responsible for redistribution of mass from larger size classes to smaller size classes. The third kernel function, $a(r, r_j)$ represents the coalescence probability of two drops of sizes $r$ and $r_j$. These three functions can either be obtained experimentally or from fully resolved simulations at the microscale. These functions now allow for the modeling of the evolution of populations of drops following the microscale rules defined in these kernel functions.

The primary difference between the LHS of Eq. 6.2 and standard Navier-Stokes equations is the last term, $\nabla_{\mathbf{v}}.(\langle \mathbf{A}|\mathbf{x}, \mathbf{v}, r; t\rangle f)$. This term accounts for the advection of the distribution function through the velocity co-ordinate, due to the action of an external force. Integrating Eq. 6.2 in the velocity co-ordinate, one can show that this term gives rise to $n\langle \mathbf{A}|\mathbf{x}, \mathbf{v}, r; t\rangle$ as a source term on the RHS in Eq. 6.12. This is in accordance with conventional notion where (say) drag force is a source term in the momentum equation for the dispersed phase.

Following the procedure in Fox Fox (2012), transport equations can be written for the moments of $f$. These moment equations of $f$ can also be written in terms of classical Eulerian transport equations for mass and momentum. We will restrict our further discussion to that form and we will simplify Eq. 6.2. The balance of number density can be written as,

$$\frac{\partial n}{\partial t} + \frac{\partial}{\partial x_k}[\langle V_k\rangle n] + \frac{\partial}{\partial r}\left[\langle \Theta|\mathbf{x}, r; t\rangle n\right] = B_B^{'} - D_B^{'} + B_C^{'} - D_C^{'}, \tag{6.7}$$

where the birth and death of droplet $r$ due to breakup and coalescence respectively are

:

$$B_B^{'} = \int_{-\infty}^{\infty} B_B d\mathbf{v} = \int_{-\infty}^{\infty} \int_{r}^{\infty} \beta(r \mid r_j)\Gamma(f, r_j) f(\mathbf{x}, r_j, t)\, dr_j d\mathbf{v}, \tag{6.8}$$

$$D_B^{'} = \int_{-\infty}^{\infty} D_B d\mathbf{v} = \int_{-\infty}^{\infty} \Gamma(f, \mathbf{v}, r) f(\mathbf{x}, \mathbf{v}, r, t) d\mathbf{v}, \tag{6.9}$$

$$B_C^{'} = \int_{-\infty}^{\infty} B_C d\mathbf{v} = \frac{1}{2} \int_{-\infty}^{\infty} \int_{0}^{r} a\left[(r^3 - r_j^3)^{1/3}, r_j\right] f(\mathbf{x}, \mathbf{v}, (r^3 - r_j^3)^{1/3}, t) f(\mathbf{x}, \mathbf{v}, r_j, t)\, dr_j d\mathbf{v}, \tag{6.10}$$

$$D_C^{'} = \int_{-\infty}^{\infty} D_C d\mathbf{v} = \int_{-\infty}^{\infty} \int_{0}^{\infty} a\,(r, r_j)\, f(\mathbf{x}, \mathbf{v}, r, t) f(\mathbf{x}, \mathbf{v}, r_j, t)\, dr_j d\mathbf{v}. \tag{6.11}$$

The mean velocity equation is obtained by multiplying Eq. 6.2 with particle velocity and integrating over the velocity space reads as,

$$\begin{aligned} &\frac{\partial n\langle V_k\rangle}{\partial t} + \frac{\partial}{\partial x_k}[n\langle V_k\rangle \otimes \langle V_k\rangle] + \frac{\partial}{\partial r}\left[n\langle V_k\rangle\langle\Theta|\mathbf{x}, r; t\rangle\right] \\ &= n\langle A_k|\mathbf{x}, r, t\rangle + B_B^{''} - D_B^{''} + B_C^{''} - D_C^{''} + \frac{\partial}{\partial x_k}\left(n\bar{\bar{\tau}}\right), \end{aligned} \tag{6.12}$$

where the birth and death of droplet $r$ due to breakup and coalescence respectively are :

$$B_{B_k}^{''} = \int_{-\infty}^{\infty} v_k B_B d\mathbf{v} = \int_{-\infty}^{\infty} \int_{r}^{\infty} v_k \beta(r \mid r_j)\Gamma(f, r_j) f(\mathbf{x}, r_j, t)\, dr_j d\mathbf{v}, \tag{6.13}$$

$$D_{B_k}^{''} = \int_{-\infty}^{\infty} v_k D_B d\mathbf{v} = \int_{-\infty}^{\infty} v_k \Gamma(f, \mathbf{v}, r) f(\mathbf{x}, \mathbf{v}, r, t) d\mathbf{v}, \tag{6.14}$$

$$B_{C_k}^{''} = \int_{-\infty}^{\infty} v_k B_C d\mathbf{v} = \frac{1}{2} \int_{-\infty}^{\infty} \int_{0}^{r} v_k a\left[(r^3 - r_j^3)^{1/3}, r_j\right] f(\mathbf{x}, \mathbf{v}, (r^3 - r_j^3)^{1/3}, t) f(\mathbf{x}, \mathbf{v}, r_j, t)\, dr_j d\mathbf{v} \tag{6.15}$$

$$D_{C_k}^{''} = \int_{-\infty}^{\infty} v_k D_C d\mathbf{v} = \int_{-\infty}^{\infty} \int_{0}^{\infty} v_k a\,(r, r_j)\, f(\mathbf{x}, \mathbf{v}, r, t) f(\mathbf{x}, \mathbf{v}, r_j, t)\mathbf{v}\, dr_j d\mathbf{v}. \tag{6.16}$$

The velocity of the center of mass $\mathbf{v}_c$ of the two coalescing entities, usually calculated assuming conservation of momentum during a coalescence event:

$$\mathbf{v}_c = \frac{(r^3 - r_j^3)\mathbf{v}\left((r^3 - r_j^3)^{1/3}\right) + (r_j^3)\mathbf{v}(r_j)}{r^3}. \tag{6.17}$$

These equations are obtained by integrating Eq. 6.2 over the velocity space $\mathbf{v}$. The polykineticity aspect explicit in Eq. 6.2 is now retained as a gradient stress term, following the assumption that departures from local equilibrium are small. This is, in principle, similar to modeling turbulence by separating the velocity into a mean velocity field and a fluctuation field with the latter usually modeled as additional gradient stress. These equations are closed in the variables $(n, \langle V \rangle)$ as long as $\overline{\overline{\tau}}$ can be related to the other field variables. These equations are the classical (isothermal) Population Balance Equations (PBE). As mentioned before, the PBE involve four microscopic constitutive kernel functions to handle the breakage and coalescence processes: (i) $\Gamma(f, |\nabla \mathbf{v}|, r)$,(ii) $\beta(r|r_j)$, (iii) $\langle \Theta | \mathbf{x}, \mathbf{v}, r; t \rangle$ and (iv) $a(r, r_j)$. These functions model the (i) frequency of breakage of a drop of size $r$, (ii) the probability density of a drop of size $r$ forming from the breakup of a parent drop of size $r_j$, (iii) the growth rate of a drop of size $r$ and (iv) the agglomeration probability density of two drops of sizes $r$ and $r_j$.

A range of possible forms of these kernel functions have been proposed for bubble breakup. The reader is referred to Jakobsen Jakobsen (2008) and Liao and Lucas Liao and Lucas (2009, 2010) for the breakage and coalescence kernels widely used in the bubble breakup literature. In fact, Krepper and co-workers Krepper et al. (2007) have applied PBE to a wide range of bubbly flow problems and demonstrated good agreement with experimental data.

Sprays are also two-phase in nature similar to bubbly flows, except for two physical differences. Firstly, the inertia associated with the dispersed phase is higher, resulting in velocity field differences. Secondly, the range of Weber numbers and other non-dimensional parameters is quite different in the case of sprays. These two physical differences do not allow the direct usage of the bubble breakup kernel models. Specialized kernels are therefore required for spray PBE applications.

### 6.3.3 Comparative assessment of different modeling approaches

Based on the modeling challenges posed by sprays in Sec. 6.2 and the principal features of multiphase flow modeling approaches reviewed in Sec. 6.3, we provide a comparative assessment of current spray modeling approaches.

#### 6.3.3.1 Wide range of volume fraction and droplet Knudsen number

The LE approach with two-way coupling can be used for dispersed two–phase flows from the dense to the dilute regime for the entire range of droplet Stokes and Knudsen numbers Subramaniam (2013). Both the two–fluid EE and PBE moment equation approaches can be used in regions of the spray where $Kn < 0.1$, but their closure models based on the CE formalism are not applicable in other regions where this criterion is violated (see Fig. 6.5 where the Knudsen number criterion is violated in the center and edges of the hollow cone spray). However, the multi-fluid multi-velocity Eulerian approach that is based on the kinetic description Laurent et al. (2004a) yields excellent agreement for number density evolution when compared with LE simulations for dilute polydisperse, evaporating sprays Kah et al. (2010). The extension of these methods to dense sprays is ongoing and preliminary reports appear promising Doisneau et al. (2012).

#### 6.3.3.2 Randomness in the configuration of dispersed phase

Since the LE approach represents the position pdf of the droplets it can reproduce the transport of the number density accurately even in the dilute collisionless regime. It can also capture droplet trajectory crossing accurately. Droplet velocity fluctuations also arise naturally in the LE approach. Eulerian approaches based on CE type closures that assume collision–dominated flow typically fare poorly in the dilute collisionless regime. They are not capable of capturing droplet trajectory crossing. Eulerian approaches based on quadrature–based moment methods (QBMM) can capture the transport of the number density accurately even in the dilute collisionless regime Desjardins et al. (2008), and they are computationally inexpensive compared to LE methods.

#### 6.3.3.3 Nonlinearities such as drag dependence on velocity distribution

Since the LE approach represents the distribution of droplet velocities it easily captures the nonlinear dependence of droplet acceleration on droplet velocity. Eulerian approaches based on QBMM can also perform well in this regard provided the underlying distribution is represented by sufficient nodes.

#### 6.3.3.4 Polydispersity and size–velocity correlation

In the sectional multifluid EE approach, polydispersity is represented in terms of size classes. A transport equation is associated with each of these size classes, and the interaction of each size class with the gas phase, as well as the interaction between size classes needs to be modeled Greenberg et al. (1986, 1993); Laurent et al. (2004b); Laurent and Massot (2001). The Eulerian sectional approach can capture some aspects of the size–velocity correlation Rayapati et al. (2011). Eulerian approaches based on QBMM can capture size–velocity correlations well. When coupled with the sectional description of droplet sizes Laurent et al. (2004a), the resulting Eulerian multi-fluid, multi-velocity model Kah et al. (2010) is shown to accurately capture both particle trajectory crossings and the size-dependent dynamics of evaporation and fluid drag. Since the LE approach represents the joint size–velocity pdf of the droplets it can reproduce polydispersity, trajectory crossing and size–velocity correlation effects faithfully, and is often used as a benchmark for other simulation approaches.

#### 6.3.3.5 Multiscale interactions

Treating the complex interaction between polydisperse spray droplets and turbulence in the carrier gas is easier in the LE approach than in the multifluid context. However, it should be noted that some phenomena such as clustering or preferential concentration of droplets actually require modeling the evolution of the two–particle or pair correlation function, which is not represented in ddf–based LE models Subramaniam (2013). Also it is possible to devise models of multiscale interactions even in the Eulerian two–fluid approach Xu and Subramaniam (2006).

#### 6.3.3.6 Polykineticity

The two–fluid (or sectional multifluid) EE and PBE moment equation approaches cannot predict the polykineticity inherent in sprays, as illustrated in Fig. 6.2, whereas LE methods can capture this phenomenon correctly. In this context, QBMM are a good alternative to two–fluid EE and PBE moment equation approaches based on CE closures because they capture polykineticity associated with crossing jets Desjardins et al. (2008) by transporting the discretized ddf correctly.

#### 6.3.3.7 Nonequilibrium effects that lead to phenomena such as preferential concentration and clustering

Since nonequilibrium velocity distributions are admissible in the LE approach, it has a significant advantage when it comes to simulation of sprays or riser flows all the way from the dense to the dilute regime over a range of droplet or particle Stokes and Knudsen numbers. The LE approach is capable of representing nonequilibrium velocity distributions. The two–fluid (or sectional multifluid) EE and PBE moment equation approaches that rely on CE closures are usually restricted to small departures from the equilibrium velocity distribution, although more recent developments of the kinetic theory for granular flow do not make this assumption Garzò et al. (2007). However, QBMM that directly transport the discretized ddf can capture nonequilibrium velocity distributions Passalacqua et al. (2011).

#### 6.3.3.8 Collision modeling

A stochastic collision model, such as the NTC model Schmidt and Rutland (2000), is usually employed in the LE approach. Collision integrals are approximated in the two–fluid (or sectional multifluid) EE and PBE moment equation approaches that use CE closures. Collisions can be treated accurately using QBMM because they reduce the collision integrals to quadrature of the discretized ddf Fox (2013).

This comparative assessment of models based on the two-fluid theory and the ddf–based approach that are formulated at different levels of closure throws light on their usage for different applications.

### 6.3.4 Outlook for models

The outlook for spray models based on the foregoing discussion may be summarized as follows. Spray modeling is challenging because sprays possess several unique characteristics that pose formidable modeling challenges. Of the various statistical representations currently available for spray modeling, the kinetic equation (modeled ddf equation) appears to be the most promising mesoscopic descriptor of the dispersed-phase Fox (2012) even though it accounts for two–phase coupling in a sequential, as opposed to simultaneous manner (see Ref. Tenneti and Subramaniam (2013) for details). LE methods can be meaningfully interpreted as an indirect solution to the modeled ddf equation using computational particles, and their ability to accurately model two–phase flow problems with a wide range of Stokes and Knudsen numbers makes them suitable for spray modeling Subramaniam (2013). Recent advancements show LE is numerically convergent and accurate if appropriate algorithms (grid-free estimators and computational particle number density control) are employed Garg et al. (2007, 2009). Estimates of the Knudsen number in sprays indicate that continuum models based on classical kinetic theory closures are valid over some portion of the spray. For hollow-cone sprays, the droplets in the annular fan region show $Kn < 0.1$ corresponding to continuum regime, but both the spray center and spray edge correspond to much higher $Kn$ where classical kinetic theory closures would be inapplicable. Therefore, PBE approaches based on these kinetic theory models would be appropriate for modeling some portions of the spray. However, they may exhibit limitations in capturing polykinetic effects, especially at the spray center and edges. For capturing polykinetic effects, QBMM with accurate numerical schemes for the transport terms would be preferable. Apart from LE, QBMM that approximate the ddf by a few abscissas and weights are an attractive alternative in the Eulerian framework especially since they incur lower computational cost.

## 6.4 Classification of multiphase flow simulations

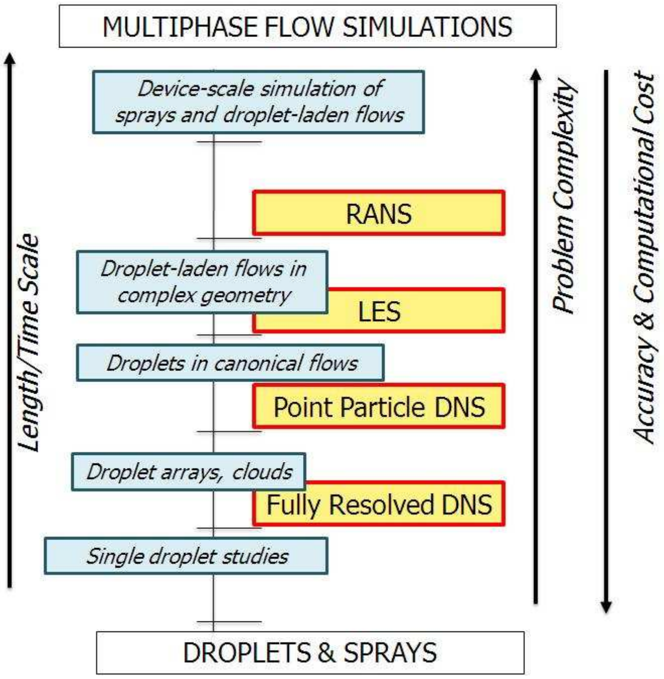

Figure 6.10 Classification of multiphase flow simulation approaches by scale, accuracy, computational cost, and problem complexity.

### 6.4.1 Overview of multiphase flow simulations

Multiphase flow simulations can be classified by the length and time scales they resolve, their accuracy, the computational cost they incur, and the level of complexity in the problem they solve. Figure 6.10 shows simulation approaches ranging from FR–DNS through point–particle DNS (PP–DNS), LES and RANS.

At the smallest scale, single droplet numerical studies with emphasis on droplet vaporization and deformation has been reported by Helenbrook and Edwards (2002); Schmidt et al. (2002); Dwyer and Dandy (1990); Dwyer (1989). Frequently LE methods couple Lagrangian tracking of computational particles to a carrier flow description based on RANS equations. However, it is possible to use the LE approach to couple a Lagrangian description of the dispersed phase with large eddy simulations (LES) or direct numerical simulation (DNS) of the carrier gas phase, resulting in the following principal categories of LE methods:

(1) FR-DNS of droplet-laden, particle-laden or bubbly flow flow where the exact Navier-Stokes equations are solved by fully resolving the droplet, particle or bubble by imposing boundary conditions at each particle or droplet's surface Xu and Subramaniam (2010); Bagchi and Balachandar (2003); Uhlmann (2005); Zhang and Prosperetti (2005); Quan et al. (2009); Gorokhovski and Herrmann (2008); Herrmann (2008); Esmaeeli and Tryggvason (1998); Tenneti et al. (2011).

(2) Point-particle DNS (PP-DNS) with physical droplets or particles Elghobashi and Truesdell (1992); Squires and Eaton (1991b,a); Wang et al. (2009); Mashayek (1998); Mashayek and Jaberi (1999); Sundaram and Collins (1997); Miller and Bellan (1999); Reveillon and Vervisch (2005).

(3) PP-DNS with stochastic particles Boivin, M. and Simonin, O. and Squires, K.D. (1998).

(4) Point particle LES with physical droplets Nora (2000); Apte et al. (2003).

(5) Point particle LES with stochastic particles Almeida and Jaberi (2008); Okong'o and Bellan (2004); Apte et al. (2009).

(6) Averaged equations: RANS CFD A. A. Amsden, and P. J. O'Rourke, and T. D. Butler (1989).

The principal difference between the FR-DNS and PP-DNS is that while the former can be used to quantify the interphase models, the PP-DNS assume models for interphase transfer terms such as particle acceleration and droplet vaporization. However, PP-DNS of sprays have been used very effectively to map out regimes of turbulent combustion Reveillon and Vervisch (2005) and for development of LES sub-models Miller and Bellan (1999). The treatment of collisions can also be used to categorize LE methods as those that employ a statistical treatment of collisions O'Rourke (1981); Schmidt and Rutland (2000); O'Rourke et al. (2009) in contrast to direct calculation of collisions between particles using either hard–sphere collisions Allen and Tildesley (1989) for low volume fraction or soft–sphere discrete element method (DEM) collision models Matuttis et al. (2000); Alam and Luding (2003); Cundall and Strack (1979) for high volume fraction Sun et al. (2007).

The classification shown in Fig. 6.10 allows a comparison of trade-offs between accuracy, problem complexity and computational cost that each of these simulation approaches represents. Moving up the length and time scale axis we have simulations ranging from single–droplet studies and FR–DNS to RANS that are able to access progressively larger system sizes. However, this is at the cost of accuracy, with the single–droplet and FR–DNS studies being most accurate, while the large device–scale simulations necessarily involve modeling assumptions in order to solve more complex problems. The comparison of the computational cost of different approaches (FR–DNS to LES to RANS) is not usually meaningful because they offer different levels of accuracy. It is most meaningful to compare two simulation methods that provide the same level of flow information at the same level of accuracy. However, in general it is true that if the same problem size were to be simulated, the computational cost increases as one goes from RANS to LES to FR–DNS.

### 6.4.2 Requirements of simulations

The principal requirements of a spray simulation code are the following:

(1) Numerically stable and convergent implementation.

(2) Efficient solver.

(3) Ability to represent complex geometry.

(4) Reasonable requirement in terms of computational resources.

These requirements can be used in conjunction with the classification of multiphase flow simulation methods to compare different spray simulation codes and thereby arrive at the set of choices most suitable to the application.

### 6.4.3 Outlook for simulations

We conclude our survey of simulations with an outlook for simulation methods currently in use. FR–DNS is currently restricted to idealized problems such as homogeneous particle or droplet suspensions because of its high computational cost, but if it is performed with adequate resolution it is very useful for gaining insight into flow physics and for model development Tenneti and Subramaniam (2013). Its principal utility is in extracting information for models. It has also been used to reveal interesting flow physics in primary atomization Gorokhovski and Herrmann (2008), although it is still restricted to relatively low Reynolds numbers. Faster computer processors and improved algorithms that can be parallelized efficiently are extending the range of accessible scales and complexity of problems that can be solved using FR–DNS.

For the next level of canonical problems such as channel flow or pipe flow, LES with LE is rapidly becoming a powerful tool to reveal flow features and organization of dispersed phase into structures at length scales currently inaccessible to FR–DNS Okong'o and Bellan (2004); Capecelatro and Desjardins (2012a,b). The challenges for LES of multiphase flows are developing scalable sub-grid closures for both carrier and dispersed phases and capturing instabilities that originate at the microscale.

At the device-scale, the Eulerian multifluid approach coupled with QBMM Kah et al. (2010) to solve a discretized form of the kinetic equation (based on the ddf) is very promising. The QBMM approach can also be coupled with LES (instead of Lagrangian tracking of the dispersed phase elements) and this approach also has great potential to transform spray computations.

## 6.5 Summary

Spray modeling and simulation is challenging because of its unique characteristics as a multiphase flow with coupled nonlinear, multiscale interactions and nonequilibrium effects. A modeling framework based on random field and stochastic point process approaches enables classification of several models currently in use. Spray simulations can be classified on the basis of scale of applicability, accuracy, and computational cost. The choice of spray model and simulation method depends on the multiphase phenomena that need to be captured. This choice ultimately represents a trade-off between accuracy and computational cost.

# CHAPTER 7. CONCLUSIONS AND FUTURE WORK

## 7.1 Conclusions

DNS-LPT simulations have been used to quantify the performance of a granular filter and to investigate the dependence of global filtration quantities such as penetration and single-collector efficiency on granule volume fraction $\epsilon_s$, mean slip Reynolds number $Re_m$, and particle Stokes number $St$ for filtration of inertial particles. For inertial particles we show that the penetration in a granular filter is the outlet particle flux normalized by its inlet value, which reduces to the normalized concentration (or number density) for particles of negligible inertia. For finite mean slip Reynolds number single-collector efficiency $\eta_s$ is a function of granular volume fraction, Stokes number, and mean slip Reynolds number. The effective Stokes number suggested by D'Ottavio and Goren (1983) to collapse single-collector efficiency data for moderate mean slip Reynolds number is modified to reflect the weak dependence of single-collector efficiency on mean flow Reynolds number for $Re_m > 10$ by changing the $Re_m^{1/2}$ dependence to $Re_m^{1/5}$. The single-collector efficiency data obtained from DNS–LPT over the range of granule volume fraction, mean slip Reynolds number and particle Stokes number simulated collapses nicely when plotted against the modified effective Stokes number. Based on the DNS–LPT data we propose a model for the filter coefficient $\lambda$ in terms of the modified effective Stokes number.

In applications such as bio-oil production the particles are generally polydisperse. We derive expressions for the cumulative polydisperse single-collector efficiency $\eta_{s,poly}^{cum}(St)$

and total polydisperse single-collector efficiency $\langle \eta_{s,poly} \rangle$ for granular filtration of particles with arbitrary size distributions in Stokes flow and moderate Reynolds number flows. We also derive a transport equation for axial variation of the particle flux for polydisperse particles, which leads to an analytical solution for the size-dependent particle flux as a function of axial location. The results obtained from the polydisperse analytical model give a very good match with 2D-LPT and DNS-LPT simulations. The analytical solution for the axial variation of particle flux predicts profiles similar to DNS-LPT results.

Bouncing of particles from granule surface is common in granular filtration of high-speed particulate flows. The DNS–LPT approach developed for simulating granular filtration was extended to simulate bouncing of particles using hard-sphere collision between particles and granules. The DNS–LPT results give a reasonable match with the experiments (performed by collaborators) with bouncing of particles. A correlation for adhesion probability is proposed from the DNS–LPT data in terms of modified effective Stokes number and the normalized adhesion energy $H_T$. Normalized adhesion energy is adhesion energy normalized by granular temperature.

The model for filter coefficient suggested in this study using DNS-LPT is implemented and tested in two–fluid CFD simulations using the fast Eulerian model for calculating particle velocity. The results obtained from the CFD simulations of full-scale moving granular bed give reasonable match with the experiments. These conclusions summarize the original research contributions of this dissertation.

## 7.2 Future work

This section summarizes possible extensions of this research work.

### 7.2.1 CFD modeling

1. Test the homogeneous bed problem with the mean particle velocity obtained from DNS instead of using particle velocity obtained from the fast Eulerian model and compare the particle flux profiles obtained from CFD and DNS
2. Re-run the CFD model with the new $\langle V_p \rangle$ correlation and check the particle flux profiles and char accumulation in granular bed

### 7.2.2 DNS-LPT approach

1. Build a correlation for $\langle V_p \rangle (Re_m, \phi, St)$ from DNS-LPT data
2. Extend the DNS-LPT approach to simulate sub-micron particles, where Brownian diffusion is the most important mechanism for filtration of particles and extend DNS-LPT approach to applications dealing with particles with diameter less the $1\mu$m
3. Introduce the temperature effect on the filtration of particles in a granular bed by modeling the thermophoretic force
4. Currently the DNS-LPT approach is used for particles with one-way coupling of particles, but the DNS-LPT approach can be used to simulate two-way coupling between particles and fluid and also allow the granules to grow with the deposition of particles on granule surface
5. The DNS-LPT approach can be used for developing models to be used in CFD code for water filtration. Water treatment of ground water using granular bed is a cheap and efficient method. Ground water get polluted due to different kinds of pollutants:

(a) Inorganic Pollutants: Pb in gasoline, radionuclide, phosphorus and nitrogen, other heavy metals

(b) Organic Pollutants : Pesticides and herbicides and materials in common household and industrial use

(c) Biological Pollutants: Escherichia coli, Cryptosporidium, Giardia

(d) Suspended solids : Clay, silt

Radial collectors can be used to naturally treat and extract clean water. In the design of radial collector wells CFD simulation can provide significant input, but there is a need for development of high fidelity models to improve the CFD simulations and we can use DNS-LPT simulations to develop these high fidelity models. One of the modeling approach is a multiscale approach as shown in Fig. E.1, where the DNS-LPT can be used to develop models for the hydraulic conductance $K$ and the dispersion coefficient $D$, which can be used in a code like MODFLOW (Customized code for finding the head of water in ground). The MODFLOW can be further be used in the development of radial collector wells in remote locations.

Another approach would be using commercial package like ANSYS-FLUENT to simulate the full scale water plant using DNS-LPT and MODFLOW as shown in Fig. E.2 In the second approach the developed models for the conductance $K$ and dispersion coefficient $D$ can be used in commercial package like ANSYS-FLUENT which can be used to simulate a full-scale water treatment plant, and the MODFLOW can be used to setup the boundary conditions for ANSYS-FLUENT.

6. Another application of the DNS-LPT would be in chemical looping combustion.Chemical-looping combustion (CLC) is an energy efficient technology for the combustion of gas or solid fuel and provide a sequestration ready CO2 stream with no additional energy required for separation. In CLC the traditional combustion process is sep-

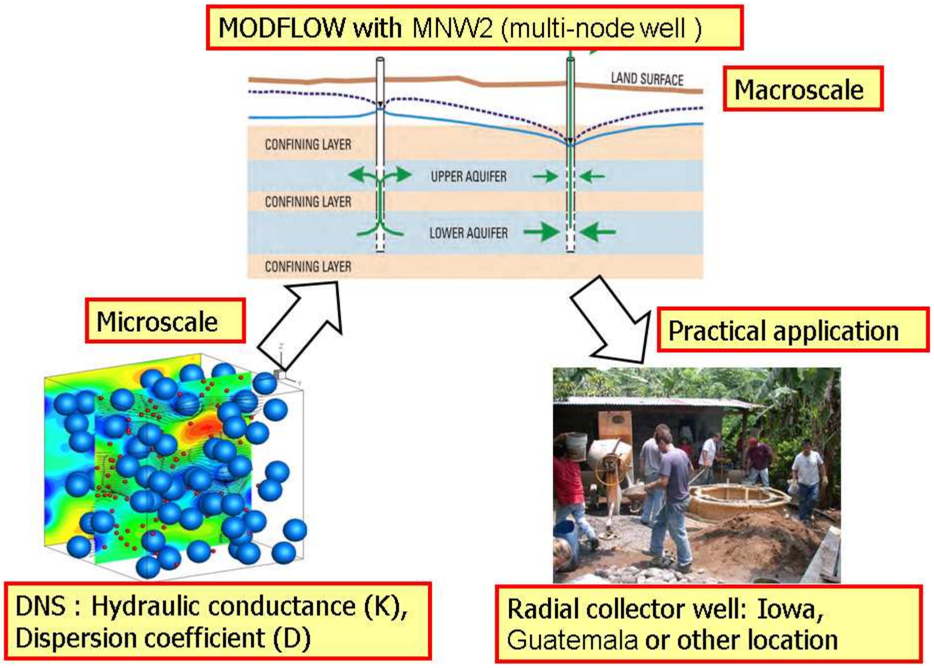

Figure 7.1 Multiscale approach for the development of models for practical application.

arated into two parts, a fuel reactor and an air reactor and a metal oxide is used as an oxygen carrier that circulates between these two reactors. The air reactor (AR) is a high velocity riser and the fuel reactor (FR) is a low-velocity bubbling fluidized bed. The high gas velocity in the AR provides the driving force for both the reactors and the oxygen carriers are collected in a cyclone and then transported to the FR. The reduced metal oxide particles are transported from FR to AR by gravity. This oxygen carrier avoids the direct contact of the air from fuel. A detailed view of the CLC is shown in Fig F.1. CLC is a very promising approach for having a clean environment.

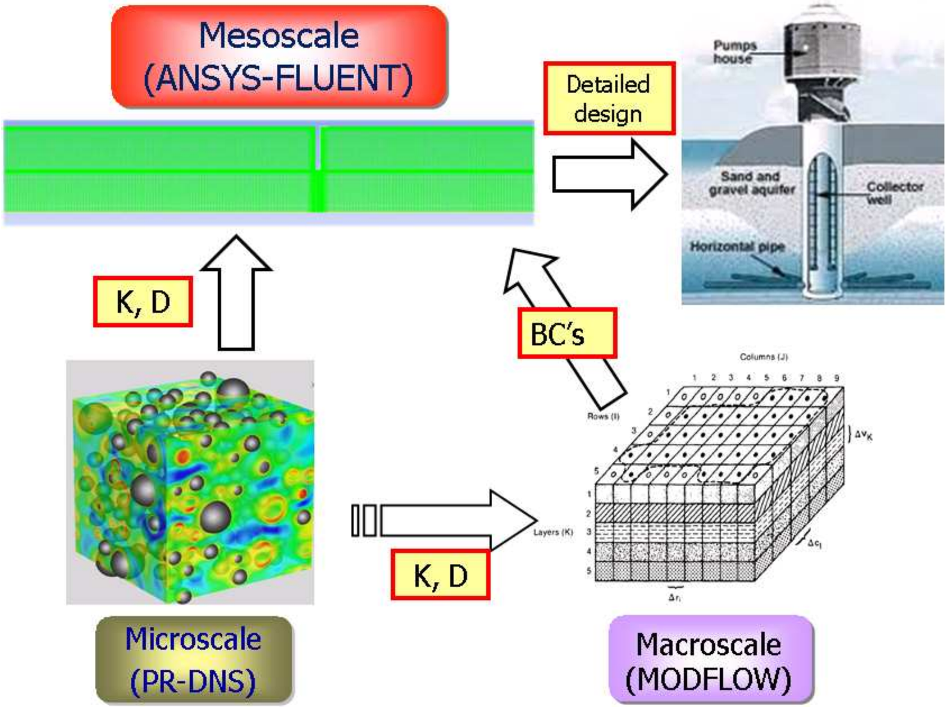

Figure 7.2 Multiscale approach for the development of models for practical application.

Detailed multiphase computational fluid dynamic (CFD) analysis of CLC would allow and speed up the optimization and development of the process. Most of the CFD simulations found in literature are restricted to fuel reactor. An interconnected multi-phase CFD model is necessary to model both the FR and AR allowing an exchange of solid flow between reactors in the form of sink and time-dependent boundary conditions. DNS-LPT can be used to develop model for sink term on both the FR and AR side.

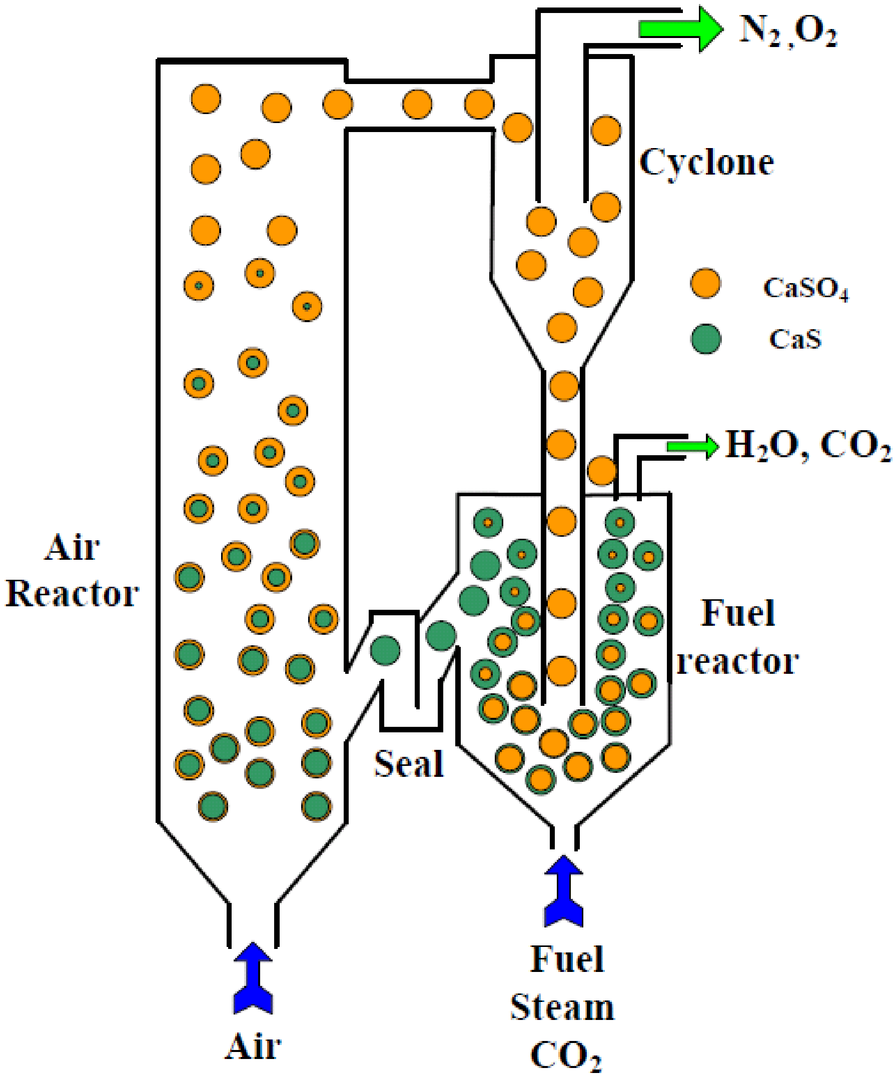

Figure 7.3 Chemical-looping combustion using $CaSO_4$ as oxygen carrier

# APPENDIX A. Mass balance of particles in a granular bed

If we consider an differential volume in a granular with a length $dx$ and a cross-section area $A_c$, the number of spherical collectors in the differential volume, $N_s$, is given by:

$$N_s = \frac{6\epsilon_s A_c dx}{\pi D_g^3}, \tag{A.1}$$

where $D_g$ is diameter of the spherical collector and $\epsilon_s$ is the granule volume fraction. The accumulation of particles in the differential volume can be expressed as:

$$N_s \eta_s \frac{\pi D_g^2}{4} U^s C = -Q dc, \tag{A.2}$$

where $Q = U^s A_c$ is the volumetric flow rate. Further modifying Eq. A.2 using Eq. A.1:

$$\frac{3\eta_s \epsilon_s C dx}{2D_g} = -dc. \tag{A.3}$$

Now considering the $L$ being the granular bed height for which $C = C_0$ at $x = 0$ and $C = C_e$ at $x = L$, we can write :

$$\int_{C_0}^{C_e} \frac{dC}{C} = -\frac{3\eta_s \epsilon_s}{2D_g} \int_0^L dx, \tag{A.4}$$

and can be further written as

$$\ln \frac{C_e}{C_0} = -\frac{3\eta_s \epsilon_s L}{2D_g}. \tag{A.5}$$

# APPENDIX B. Numerical calculation of particle number density and flux

The particle number density $n(x,t)$ is calculated at cell center in simulation, if the length of the computational domain is discretized with $M$ grid cells in each direction then the size of each grid cell is $\Delta x = L/M$. The number density is represented at cell center and is calculated in each cell as

$$n(\mathbf{x},t) = \frac{N_{cell}}{(\Delta x)^3}, \tag{B.1}$$

where $N_{cell}$ is the number of particles in each cell. The mean particle velocity $\langle V_k \rangle$ is also represented at cell center and is calculated as

$$\langle V_x \rangle = \frac{\sum\limits_{i=1}^{N_{cell}} V_x^i}{N_{cell}}. \tag{B.2}$$

The particle flux $J_k = \langle V_k \rangle n$ at the cell center is calculated as

$$J_x = \frac{\sum\limits_{i=1}^{N_{cell}} V_x^i}{(\Delta x)^3}. \tag{B.3}$$

Since in the granular filtration problem the particles are homogeneous in $yz$ direction and varies along $x$ direction. The number density, particle flux, mean particle velocity and fluid velocity are reported as cross-sectional averages. They are calculated as

$$\langle u^{(f)} \rangle_{A_c} = \frac{\sum\limits_{j=1}^{M_y} \sum\limits_{k=1}^{M_z} I_f u^f}{\sum\limits_{j=1}^{M_y} \sum\limits_{k=1}^{M_z} I_f}, \tag{B.4}$$

where $M_y$ is the number of cells in $y$ direction, $M_z$ is the number of cells in $z$ direction and $I_f$ is the indicator function which is equal to one if the cell is in fluid otherwise it is zero. The cross section average of the mean particle velocity and the particle flux is also calculated in the same way.

# APPENDIX C. Derivation of the number density equation

The statistical description at the single particle level is given by the single-particle distribution function $f(\mathbf{x},\mathbf{v},r,t)$ also known as droplet distribution function in spray literature (Williams, 1958). The $f(\mathbf{x},\mathbf{v},r,t)$ is related to the position, velocity and radius of the particles by

$$f(\mathbf{x},\mathbf{v},r,t)=\left\langle f^{'}(\mathbf{x},\mathbf{v},r,t)\right\rangle=\left\langle\sum_{i=1}^{N_p(t)} f_i^{'}(\mathbf{x},\mathbf{v},r,t)\right\rangle=\left\langle\sum_{i=1}^{N_p(t)}\delta_{\mathbf{X}^{(i)}}\delta_{\mathbf{V}^{(i)}}\delta_{R^{(i)}}\right\rangle, \qquad \text{(C.1)}$$

where $\delta_{\mathbf{X}^{(i)}}=\delta(\mathbf{x}-\mathbf{X}^{(i)}(t))$, $\delta_{\mathbf{V}^{(i)}}=\delta(\mathbf{v}-\mathbf{V}^{(i)}(t))$ ,$\delta_{R^{(i)}}=\delta(r-R^{(i)}(t))$, $f^{'}$ is the fine-grained density function and $f_i^{'}$ is the fine-grained density function for the $i^{th}$ particle and the expectation in Eq. C.1 is over all possible particle configurations and velocities, respectively (Subramaniam, 2000a). The single-particle distribution function $f(\mathbf{x},\mathbf{v},r,t)$ is an unnormalized density function and integrates to the expected total number of particles $\langle N_p(t)\rangle$, such that

$$\langle N_p(t)\rangle=\int_{[\mathbf{x},\mathbf{v},r_+]} f(\mathbf{x},\mathbf{v},r,t)d\mathbf{x}d\mathbf{v}dr. \qquad \text{(C.2)}$$

The evolution equation for $f(\mathbf{x},\mathbf{v},r,t)$ (Subramaniam, 2001a, 2000a) is:

$$\frac{\partial f}{\partial t}+\frac{\partial}{\partial x_k}(v_k f)+\frac{\partial}{\partial v_k}(\langle A_k|\,\mathbf{x},\mathbf{v},r;t\rangle\, f)=S(\mathbf{x},\mathbf{v},r,t), \qquad \text{(C.3)}$$

where, $S(\mathbf{x},\mathbf{v},r,t)$ is the sink term that arises due to the filtration of particles by granules, and $\langle A_k|\,\mathbf{x},\mathbf{v},r;t\rangle$ is the expected acceleration (Subramaniam, 2001a) conditional on the location $[\mathbf{x},\mathbf{v},r]$ in phase space. Note that summation is implied over repeated Roman indices. In this study, only the drag force is needed to model the conditional acceleration term. The particle distribution function can be decomposed as the particle number density $n(\mathbf{x}, t)$, and a joint probability density function $f^{C}_{\mathbf{VR}}(\mathbf{v}, r|\, \mathbf{x}; t)$ (Subramaniam, 2001a):

$$f(\mathbf{x}, \mathbf{v}, r, t) = n(\mathbf{x}, t) f^{C}_{\mathbf{V}R}(\mathbf{v}, r|\, \mathbf{x}; t). \tag{C.4}$$

For the polydisperse size distributions considered in this work, it is convenient to retain size dependence in the number density, as follows

$$n(\mathbf{x}, r, t) = \int_{[\mathbf{v}]} f(\mathbf{x}, \mathbf{v}, r, t) d\mathbf{v}. \tag{C.5}$$

The decomposition of Eq. C.4 in terms of $n(\mathbf{x}, r, t)$ becomes

$$f(\mathbf{x}, \mathbf{v}, r, t) = n(\mathbf{x}, r, t) f^{C}_{\mathbf{V}|R}(\mathbf{v}, r|\, \mathbf{x}; t), \tag{C.6}$$

which follows from the following relation :

$$f^{C}_{\mathbf{VR}}(\mathbf{v}, r|\, \mathbf{x}; t) = f^{C}_{\mathbf{V}|R}(\mathbf{v}|\, r, \mathbf{x}; t) f_R(r|\, \mathbf{x}; t), \tag{C.7}$$

and

$$n(\mathbf{x}, r, t) = n(\mathbf{x}, t) f_R(r|\, \mathbf{x}; t), \tag{C.8}$$

where $f_R(r|\, \mathbf{x}; t)$ is the size distribution of particles. The particle position distribution manifests in the particle number density $n(\mathbf{x}, r, t)$, which evolves by integrating Eq. C.3 over all the velocity space (Subramaniam, 2001a) as

$$\frac{\partial n(\mathbf{x}, r, t)}{\partial t} + \frac{\partial}{\partial x_k}(\langle V_k | r\rangle\, n(\mathbf{x}, r, t)) = S(\mathbf{x}, r, t). \tag{C.9}$$

The evolution equation for number density of monodisperse particles is

$$\frac{\partial n(\mathbf{x}, t)}{\partial t} + \frac{\partial}{\partial x_k}(\langle V_k \rangle\, n(\mathbf{x}, t)) = S(\mathbf{x}, t). \tag{C.10}$$

# APPENDIX D. Governing equation solved in PUReIBM

The mass and momentum equations that are solved at all grid points in PUReIBM are

$$\frac{\partial u_i}{\partial x_i} = 0, \tag{D.1}$$

and

$$\rho_f \frac{\partial u_i}{\partial t} + \rho_f S_i = -g_{IBM,i} + \mu \frac{\partial^2 u_i}{\partial x_j \partial x_j} + f_{u,i}, \tag{D.2}$$

where $g_{IBM,i}$ is the pressure gradient, $S_i$ is the convective term, and $R_{u,i}$is the immersed boundary force term that accounts for the solid particles in the fluid phase by ensuring no-slip and no-penetration boundary condition at the particle-fluid interface. The thermodynamic density and dynamic viscosity of fluid-phase are $\rho_f$, and $\mu$, respectively. For details about the computation of immersed boundary source term the reader is referred to Garg et al. (2010b); Tenneti et al. (2011).

In PUReIBM, the governing equations Eqs. D.1 and D.2 are solved by imposing a periodic boundary condition on fluctuating variables. The velocity field is decomposed into a spatially uniform mean flow and a fluctuating velocity field $\mathbf{u}'$ that is periodic as

$$\mathbf{u}(\mathbf{x}, t) = \langle \mathbf{u} \rangle_{\mathcal{V}}(t) + \mathbf{u}'(\mathbf{x}, t), \tag{D.3}$$

where the volumetric mean velocity is defined as

$$\langle \mathbf{u} \rangle_{\mathcal{V}}(t) = \frac{1}{V} \int_{\mathcal{V}} \mathbf{u}(\mathbf{x}, t) d\mathcal{V}. \tag{D.4}$$

In the same way the non-linear term $S_i$, pressure gradient $g_i$ and immersed boundary forcing $R_{u,i}$ terms can be decomposed and substituting the decomposed terms in Eqs. D.1

and D.2 yields the mean momentum conservation equation:

$$\rho_f \frac{\partial \langle u_i \rangle_{\mathcal{V}}}{\partial t} = \langle g_i \rangle_{\mathcal{V}} + \langle R_{u,i} \rangle_{\mathcal{V}}. \tag{D.5}$$

The fluctuating velocity field needs to be divergence free, i.e.,

$$\frac{\partial u_i'}{\partial x_i} = 0. \tag{D.6}$$

The conservation equation for the fluctuating momentum can be obtained by subtracting Eq. D.5 from Eq. D.2, which is

$$\rho_f \frac{\partial u_i^{'}}{\partial t} + \rho_f S_i^{'} = -g^{'}_{\ i} + \mu_f \frac{\partial^2 u_i^{'}}{\partial x_j \partial x_j} + R_{u,i}^{'}. \tag{D.7}$$

Taking divergence of Eq. D.7 and using Eq. D.6,the modified pressure Poisson equation for the fluctuating pressure gradient can be obtained:

$$\frac{\partial g_{IBM,i}^{'}}{\partial x_i} = \frac{\partial R_{u,i}^{'}}{\partial x_i} - \rho_f \frac{\partial S_i^{'}}{\partial x_i}. \tag{D.8}$$

The equations from Eq. D.5 to Eq. D.8 are solved to yield the flow field around the granules in PUReIBM.

# APPENDIX E. Water filtration using granular filter

Water treatment of ground water using granular bed is a cheap and efficient method. Ground water get polluted due to different kinds of pollutants:

1. Inorganic Pollutants: Pb in gasoline, radionuclide, phosphorus and nitrogen, other heavy metals
2. Organic Pollutants : Pesticides and herbicides and materials in common household and industrial use
3. Biological Pollutants: Escherichia coli, Cryptosporidium, Giardia
4. Suspended solids : Clay, silt

Radial collectors can be used to naturally treat and extract clean water. In the design of radial collector wells CFD simulation can provide significant input, but there is a need for development of high fidelity models to improve the CFD simulations and we can use DNS-LPT simulations to develop these high fidelity models. One of the modeling approach is a multiscale approach as shown in Fig. E.1, where the DNS-LPT can be used to develop models for the hydraulic conductance $K$ and the dispersion coefficient $D$, which can be used in a code like MODFLOW (Customized code for finding the head of water in ground). The MODFLOW can be further be used in the development of radial collector wells in remote locations.

Another approach would be using commercial package like ANSYS-FLUENT to simulate the full scale water plant using DNS-LPT and MODFLOW as shown in Fig. E.2

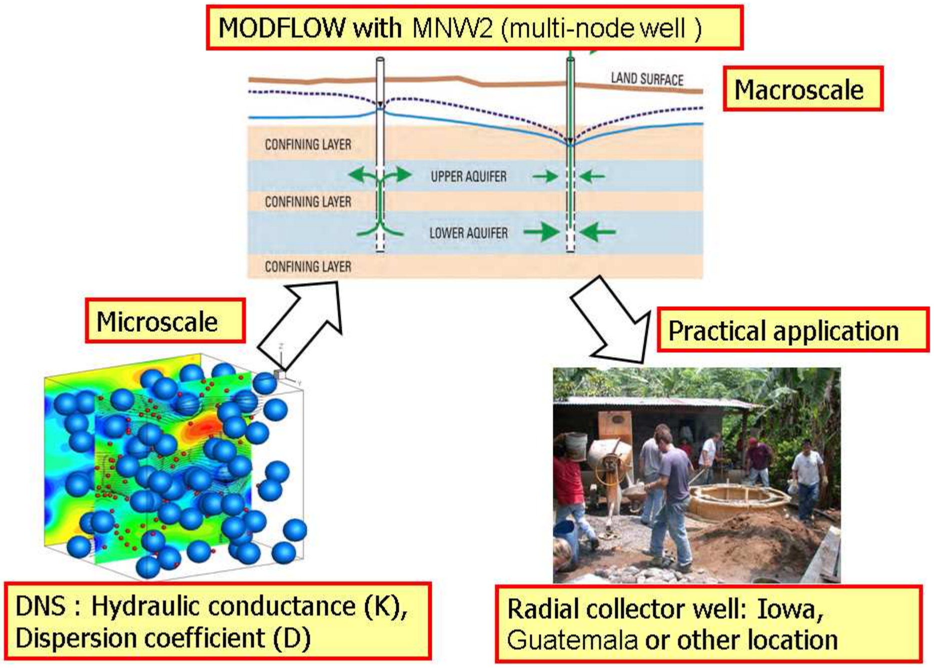

Figure E.1 Multiscale approach for the development of models for practical application.

In the second approach the developed models for the conductance $K$ and dispersion coefficient $D$ can be used in commercial package like ANSYS-FLUENT which can be used to simulate a full-scale water treatment plant, and the MODFLOW can be used to setup the boundary conditions for ANSYS-FLUENT.

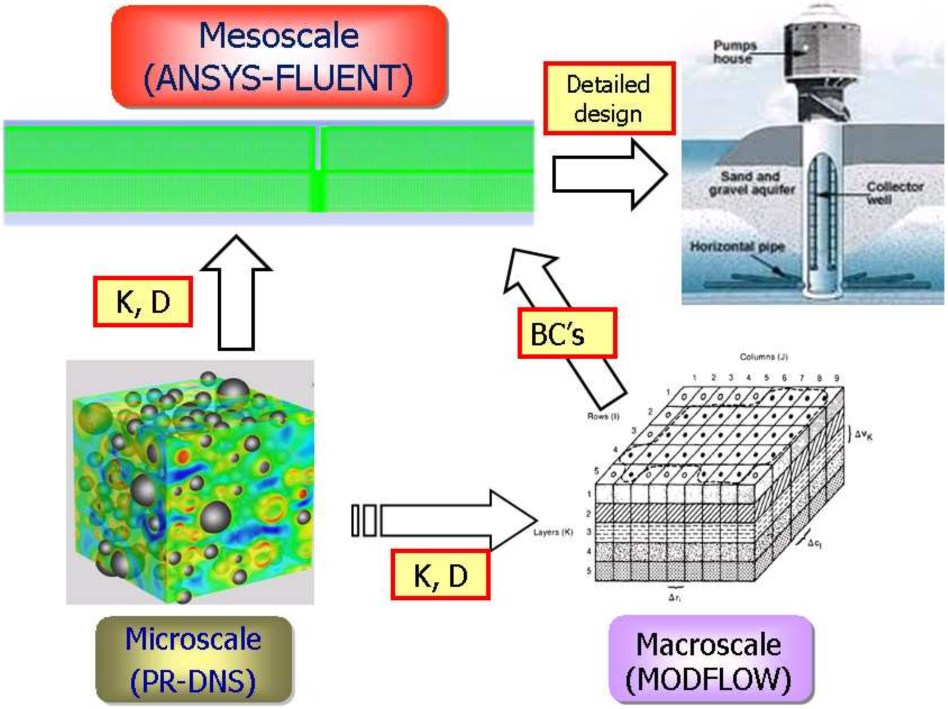

Figure E.2 Multiscale approach for the development of models for practical application.

# APPENDIX F. Chemical looping combustion

Chemical-looping combustion (CLC) is an energy efficient technology for the combustion of gas or solid fuel and provide a sequestration ready CO2 stream with no additional energy required for separation. In CLC the traditional combustion process is separated into two parts, a fuel reactor and an air reactor and a metal oxide is used as an oxygen carrier that circulates between these two reactors. The air reactor (AR) is a high velocity riser and the fuel reactor (FR) is a low-velocity bubbling fluidized bed. The high gas velocity in the AR provides the driving force for both the reactors and the oxygen carriers are collected in a cyclone and then transported to the FR. The reduced metal oxide particles are transported from FR to AR by gravity. This oxygen carrier avoids the direct contact of the air from fuel. A detailed view of the CLC is shown in Fig F.1. CLC is a very promising approach for having a clean environment.

Detailed multiphase computational fluid dynamic (CFD) analysis of CLC would allow and speed up the optimization and development of the process. Most of the CFD simulations found in literature are restricted to fuel reactor. An interconnected multiphase CFD model is necessary to model both the FR and AR allowing an exchange of solid flow between reactors in the form of sink and time-dependent boundary conditions. DNS-LPT can be used to develop model for sink term on both the FR and AR side

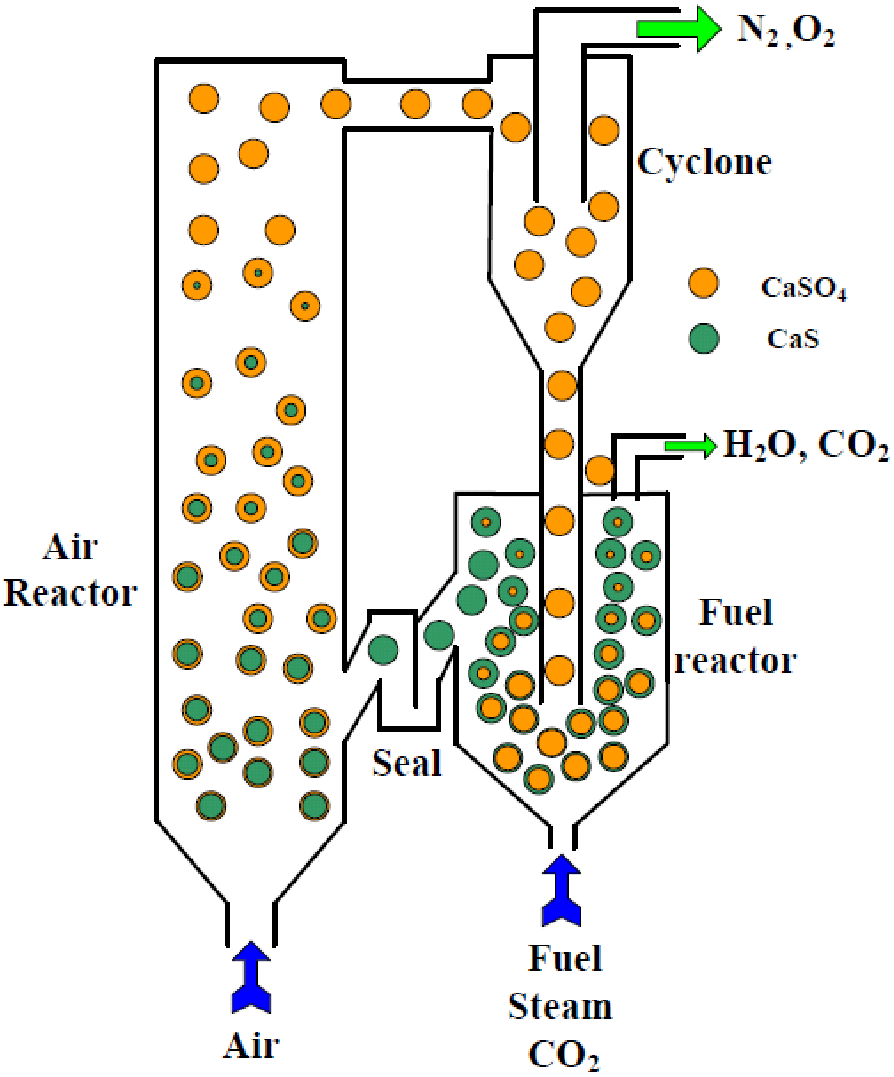

Figure F.1 Chemical-looping combustion using $CaSO_4$ as oxygen carrier

# BIBLIOGRAPHY

A. A. Amsden, and P. J. O'Rourke, and T. D. Butler (1989). KIVA–II: A Computer Program for Chemically Reactive Flows with Sprays. Technical Report LA–11560–MS, Los Alamos National Laboratory.

Adler, R. J. (1981). *The geometry of random fields*. SIAM, Chichester, NY.

Alam, M. and Luding, S. (2003). Rheology of bidisperse granular mixtures via event-driven simulations. *J. Fluid Mech.*, 476:69–103.

Allen, M. P. and Tildesley, D. J. (1989). *Computer Simulation of Liquids*. Oxford University Press, Oxford, United Kingdom.

Almeida, T. and Jaberi, F. (2008). Large-eddy simulation of a dispersed particle-laden turbulent round jet. *International Journal of Heat and Mass Transfer*, 51(3-4):683–695.

Amsden, A. A. (1993). KIVA–3: A KIVA Program with Block–Structured Mesh for Complex Geometries. Technical Report LA–12503–MS, Los Alamos National Laboratory, Los Alamos, NM 87545, USA.

Apte, S. V., Mahesh, K., Gorokhovski, M., and Moin, P. (2009). Stochastic modeling of atomizing spray in a complex swirl injector using large eddy simulation. *Proceedings of the Combustion Institute*, 32(2):2257–2266.

Apte, S. V., Mahesh, K., Moin, P., and Oefelein, J. (2003). Large-eddy simulation of swirling particle-laden flows in a coaxial-jet combustor. *Intl. J. Multiphase Flow*, 29(8):1311–1331.

Araújo, A. D., Andrade, J. S., and Herrmann, H. J. (2006). Critical Role of Gravity in Filters. *Phys. Rev. Lett.*, 97(13):138001.

Aylor, D. E. and Ferrandino, F. J. (1985). Rebound of pollen and spores during deposition on cylinders by inertial impaction. *Atmospheric Environment*, 19:803–806.

Bagchi, P. and Balachandar, S. (2003). Effect of turbulence on the drag and lift of a particle. *Phys. Fluids*, 15(11):3496.

Beetstra, R., van der Hoef, M. A., and Kuipers, J. A. M. (2007). Drag force of intermediate Reynolds number flows past mono– and bidisperse arrays of spheres. *A.I.Ch.E.J.*, 53:489–501.

Bensaid, S., Marchisio, D. L., and Fino, D. (2010). Numerical simulation of soot filtration and combustion within diesel particulate filters. *Chem. Eng. Sci.*, 65:357–363.

Beskok, A. and Karniadakis, G. E. (1996). Rarefaction and compressibility effects in gas microflows. *ASME Journal of Fluids Engineering*, 118:448–456.

Boivin, M. and Simonin, O. and Squires, K.D. (1998). Direct numerical simulation of turbulence modulation by particles in isotropic turbulence. *Journal of Fluid Mechanics*, 375:235–263.

Breault, R. W. and Guenther, C. P. (2009). Mass transfer in the core-annular and fast fluidization flow regimes of a CFB. *Powder Technology*, 190(3):385 – 389.

Capecelatro, J. and Desjardins, O. (2012a). An Euler-Lagrange strategy for simulating particle-laden flows. *Journal of Computational Physics*. (in review).

Capecelatro, J. and Desjardins, O. (2012b). Detailed investigation of clustering in riser flows using an Euler-Lagrange approach. 244th ACS National Meeting & Exposition, Philadelphia, PA.

Chiu, H. H., Kim, H. Y., and Croke, E. J. (1982). Internal group combustion of liquid droplets. In *Nineteenth Symposium (International) on Combustion*. The Combustion Institute.

Chiu, H. H. and Liu, T. M. (1977). Group combustion of liquid droplets. *Comb. Sci. and Technology*, 17(3-4):127–142.

Chiu, H. H. and Su, S. P. (1997). Theory of droplets .2. states, structures, and laws of interacting droplets. *Atomization and Sprays*, 7(1):1–32.

Cundall, P. A. and Strack, O. D. L. (1979). A discrete numerical model for granular assemblies. *Geotechnique*, 29:47–65.

Dahneke, B. (1971). The Capture of Aerosol Particles by Surfaces. *Journal of colloid and interface science*, 37(2):342–353.

Dahneke, B. (1973). Measurements of bouncing of small latex spheres. *Journal of colloid and interface science*, 45(3):584–590.

Dahneke, B. (1995). Particle Bounce or Capture - Search for an Adequate Theory: I. Conservation-of-Energy Model for a Simple Collision Process. *Aerosol Science and Technology*, 23(1):25–39.

Daley, D. J. and Vere-Jones, D. (1988). *An Introduction to the Theory of Point Processes*. Springer–Verlag, New York.

Davis, M. L. (2010). *Water and Wastewater Engineering: Design Principles and Practice*. The McGraw-Hill Companies, Inc.

Desjardins, O., Fox, R. O., and Villedieu, P. (2008). A quadrature-based moment method for dilute fluid-particle flows. *J. Comp. Phys.*, 227(4):2514–2539.

Doisneau, F., Sibra, A., Dupays, J., Murrone, A., Laurent, F., and Massot, M. (2012). An efficient and accurate numerical strategy for two-way coupling in unsteady polydisperse moderately dense sprays: application to Solid Rocket Motor instabilities. *Journal of Propulsion and Power*, pages 1–34.

D'Ottavio, T. and Goren, S. L. (1983). Aerosol Capture in Granular Beds in the Impaction Dominated Regime. *Aerosol Science and Technology*, 2(2):91–108.

Drew, D. A. (1971). Average field equations for two–phase media. *Stud. Appl. Math.*, 50:133–166.

Drew, D. A. (1983). Mathematical modeling of two–phase flow. *Annu. Rev. Fluid Mech.*, 15:261–291.

Drew, D. A. and Passman, S. L. (1998). *Theory of Multicomponent Fluids*. Applied Mathematical Sciences. Springer, New York.

Dwyer, H. A. (1989). Calculations of droplet dynamics in high temperature environments. *Prog. Energy Combust. Science*, 15:131–158.

Dwyer, H. A. and Dandy, D. S. (1990). Some influences of particle shape on drag and heat transfer. *Phys. Fluids A*, **2**((12)):2110–2118.

Dwyer, H. A., Nirschl, H., Kerschl, P., and Denk, V. (1994). Heat, mass and momentum transfer about arbitrary group of particles. In *Twenty–fifth Symposium (International) on Combustion*, pages 389–395. The Combustion Institute.

Eaton, J. K. and Fessler, J. R. (1994). Preferential Concentration of Particles by Turbulence. *Intl. J. Multiphase Flow*, 20:169–209.

El-Hedok, I. A., Whitmer, L., and Brown, R. C. (2011). The Influence of Granular Flow Rate on the Performance of a Moving Bed Granular Filter. *Powder Technology*, 214(1):69–76.

Elghobashi, S. E. and Truesdell, G. C. (1992). Direct simulation of particle dispersion in a decaying isotropic turbulence. *J. Fluid Mech.*, 242:655–700.

Enwald, H., Peirano, E., and Almstedt, A. E. (1996). Eulerian two–phase flow theory applied to fluidization. *Intl. J. Multiphase Flow*, 22:21–66.

Esmaeeli, A. and Tryggvason, G. (1998). Direct numerical simulation of bubbly flows. Part 1. Low Reynolds number arrays. *J. Fluid Mech.*, 377:313–345.

Fedkiew, P. and Newman, J. (1977). Mass transfer at high peclet numbers for creeping flow in a packed bed reactor. *A.I.Ch.E.J.*, 23:255.

Ferry, J. and Balachandar, S. (2001). A fast Eulerian method for disperse two-phase flow. *Intl. J. Multiphase Flow*, 27:1199–1226.

Fox, R. O. (2003). *Computational Models for Turbulent Reacting Flows.* Cambridge University Press.

Fox, R. O. (2012). Large-eddy-simulation tools for multiphase flows. *Annu. Rev. Fluid Mech.*, 44(1):47–76.

Fox, R. O. (2013). *Computational Models for Polydisperse Particulate and Multiphase Systems.* Cambridge University Press.

Fox, R. O. and Vedula, P. (2010). Quadrature-based moment model for moderately dense polydisperse gas-particle flows. *Ind. Eng. Chem. Res.*, 49(11):5174–5187.

Gal, E., Tardos, G., and Pfeffer, R. (1985). A Study of Inertial Effects in Granular Bed Filtration. *AIChE Journal*, 31(7):1093–1104.

Garg, R., Narayanan, C., Lakehal, D., and Subramaniam, S. (2007). Accurate Numerical Estimation of Interphase Momentum Transfer in Lagrangian-Eulerian Simulations of Dispersed Two-Phase Flows. *Intl. J. Multiphase Flow*, 33(12):1337–1364.

Garg, R., Narayanan, C., Lakehal, D., and Subramaniam, S. (2009). A Numerically Convergent Lagrangian-Eulerian Simulation Method for Dispersed Two-Phase Flows. *Intl. J. Multiphase Flow*, 35(4):376–388.

Garg, R., Shahnam, M., and Huckaby, E. (2010a). Continuum simulations of CO2 capture by dry regenerable Potassium based sorbents Reactive Multiphase Flows. In *Proceedings of the International Conference on Multiphase Flow*.

Garg, R., Tenneti, S., Mohd-Yusof, J., and Subramaniam, S. (2010b). Direct Numerical Simulation of Gas-Solids Flow based on the Immersed Boundary Method. In Pannala, S., Syamlal, M., and O'Brien, T. J., editors, *Computational Gas-Solids Flows and Reacting Systems: Theory, Methods and Practice*. IGI Global, 1st edition.

Garzò, V., Dufty, J. W., and Hrenya, C. M. (2007). Enskog theory for polydisperse granular mixtures. I. Navier-Stokes order transport. *Phys. Rev. E*, 76:031303.

Garzò, V., Tenneti, S., Subramaniam, S., and Hrenya, C. M. (2012). Enskog kinetic theory for monodisperse gassolid flows. *J. Fluid Mech.*, 712:129–168.

Gidaspow, D. (1994). *Multiphase Flow and Fluidization*. Academic Press.

Goren, S. L. (1982). Granular bed filtration for high-temperature pressure gas cleaning. *Solids Handling Processing Industry*, 14:24–29.

Gorokhovski, M. and Herrmann, M. (2008). Modeling Primary Atomization. *Annual Review of Fluid Mechanics*, 40(1):343–366.

Greenberg, J. B., Albagli, D., and Tambour, Y. (1986). An opposed jet quasi-monodisperse spray diffusion flame. *Combustion Science and Technology*, 50:255–270.

Greenberg, J. B., Silverman, I., and Tambour, Y. (1993). On the origin of spray sectional conservation equations. *Combustion and Flame*, 93:90–106.

Gutfinger, G. and Tardos, G. I. (1979). Theoretical and experimental investigation on granular bed dust filters. *Atmos. Environ.*,, 13:553.

Happel, J. (1958). Viscous flow in multiparticle systems:slow motion of fluids relative to beds of spherical particles. *A.I.Ch.E.J.*, 4:197.

Helenbrook, B. T. and Edwards, C. F. (2002). Quasi-steady deformation and drag of uncontaminated liquid drops. *Intl. J. Multiphase Flow*, 28(10):1631–1657.

Herrmann, M. (2008). A balanced force refined level set grid method for two-phase flows on unstructured flow solver grids. *Journal of Computational Physics*, 227(4):2674–2706.

Hill, R. J., Koch, D. L., and Ladd, A. J. C. (2001a). The first effects of fluid inertia on flows in ordered and random arrays of spheres. *J. Fluid Mech.*, 448:213–241.

Hill, R. J., Koch, D. L., and Ladd, A. J. C. (2001b). Moderate–Reynolds–number flows in ordered and random arrays of spheres. *J. Fluid Mech.*, 448:243–278.

Hopf, E. (1952). Statistical hydromechanics and functional calculus. *Journal of Rational Mechanics and Analysis*, 1:87–123.

Hulburt, H. M. and Katz, S. (1964). Some problems in particle technology: A statistical mechanical formulation. *Chem. Eng. Sci.*, 19:555–574.

Ishii, M. (1975). *Thermo–fluid dynamic theory of two–phase flow*. Eyrolles, Paris, France.

Israelachvili, J. N. (2010). *Intermolecular and Surface Forces, Third Edition*. Academic Press, 3rd edition.

Jackson, S. and Calvert, S. (1966). Entrained particle collection in packed beds. *A.I.Ch.E.J.*, 12(6):1075.

Jakobsen, H. A. (2008). *Chemical reactor modeling: Multiphase reactive flows.* Springer, 1st edition.

Johnson, P. C. and Jackson, R. (1987). Frictional-collisional constitutive relations for granular materials, with application to plane shearing. *J. Fluid Mech.*, 176:67–93.

Jung, Y. and Tien, C. (1992). Increase in Collector Efficiency due to Deposition in Polydispersed Granular Filtration - An Experimental Study. *Journal of Aerosol Science*, 23(5):525 – 537.

Jung, Y., Walata, S. A., and Tien, C. (1989). Experimental Determination of the Initial Collection Efficiency of Granular Beds in the Inertial-Impaction-Dominated Region. *Aerosol Science and Technology*, 11(2):168–182.

Kah, D., Laurent, F., Fréret, L., Chaisemartin, S. D., Fox, R. O., Reveillon, J., and Massot, M. (2010). Eulerian quadrature-based moment models for dilute polydisperse evaporating sprays. *Flow, Turbulence and Combustion*, 85:649–676.

Kim, H. T., Kwon, S. B., Park, Y. O., and Lee, K. W. (2000). Diffusional Filtration of Polydispersed Aerosol Particles by Fibrous and Packed-Bed Filters. *Filtration & Separation*, 37(6):37–42.

Kolakaluri, R., Murphy, E., Brown, R. C., Fox, R. O., and Subramaniam, S. (2013). Filtration model for polydisperse particulates in gas-solid flow using particle–resolved direct numerical simulation. *AICHE Journal.* (In preparation).

Kolakaluri, R. and Subramaniam, S. (2013). Study of inertial particulates in a granular filter using direct numerical simulation. *AICHE Journal.* (In preparation).

Krepper, E., Beyer, M., Frank, T., Lucas, D., and Prasser, H. M. (2007). Application of a population balance approach for polydispersed bubbly flows. In *Proceedings of the sixth International Conference on Multiphase Flow*.

Kuwabara, S. (1959). The forces experienced by randomly distributed parallel circular cylinders or spheres in a viscous flow at small Reynolds number . *J. Phys. Soc. Japan*, 14:527.

Kwon, S. B., Kim, H. T., and Lee, K. W. (2002). Analytic Solutions to Diffusional Deposition of Polydisperse Aerosols in Fibrous Filters. *Aerosol Science and Technology*, 36(931315906):742—747.

Lamb (1932). *Hydrodynamics*. Cambridge Univ. Press, 6th. edition.

Laurent, F. and Massot, M. (2001). Multi-fluid modeling of laminar polydisperse spray flames: Origin, assumptions and comparisons of section and sampling methods. *Combustion Theory and Modeling*, 5:537–572.

Laurent, F., Massot, M., and Villedieu, P. (2004a). Eulerian multi-fluid modeling for the numerical simulation of coalescence in polydisperse dense liquid sprays. *Journal of Computational Physics*, 194:505–543.

Laurent, F., Santoro, V., Noskov, M., Smooke, M. D., Gomez, A., and Massot, M. (2004b). Accurate treatment of size distribution effects in polydisperse spray diffusion flames: multi-fluid modeling, computations and experiments. *Combustion Theory and Modeling*, 8:385–412.

Liao, Y. and Lucas, D. (2009). A literature review of theoretical models for drop and bubble breakup in turbulent dispersions. *Chem. Eng. Sci.*, 64:3389–3406.

Liao, Y. and Lucas, D. (2010). A literature review on mechanisms and models for the coalescence process of fluid particles. *Chem. Eng. Sci.*, 65:2851–2864.

Libby, P. A. and Williams, F. A. (1993). *Turbulent Reacting Flows*. Combustion Treatise. Academic Press, Harcourt Brace and Co., New York.

Liboff, R. L. (2003). *Kinetic theory : Classical, Quantum, and Relativistic descriptions*. Springer-Verlag, New York, 3rd edition.

Long, W. and Hilpert, M. (2009). A correlation for the collector efficiency of Brownian particles in clean-bed filtration in sphere packings by a Lattice-Boltzmann method. *Environmental science & technology*, 43(12):4419–24.

Luding, S., Huthmann, M., McNamara, S., and Zippelius, a. (1998). Homogeneous cooling of rough, dissipative particles: Theory and simulations. *Phys. Rev. E*, 58(3):3416–3425.

Macdonald, I. F., El-Sayed, M. S., Mow, K., and Dullien, F. A. L. (1979). Flow through media-the ergun equation revisited. *I & EC Fundamentals*, 18(3):199–208.

Marshall, H., Sahraoui, M., and Kaviany, M. (1994). An Improved Analytic Solution for Analysis of Particle Trajectories in Fibrous, Two-Dimensional Filters. *Phys. Fluids*, 6:507.

Mashayek, F. (1998). Direct numerical simulations of evaporating droplet dispersion in forced low Mach number turbulence. *Intl. J. Heat Mass Transfer*, 41(17):2601–2617.

Mashayek, F. and Jaberi, F. A. (1999). Particle dispersion in forced isotropic low–Mach–number turbulence. *Intl. J. Heat Mass Transfer*, 42(15):2823–2836.

Matuttis, H. G., Luding, S., and Herrmann, H. J. (2000). Discrete element simulations of dense packings and heaps made of spherical and non-spherical particles. *Powder Technology*, 109(1-3):278–292.

Mckeen, T. and Pugsley, T. (2003). Simulation and experimental validation of a freely bubbling bed of FCC catalyst. *Powder Technology*, 129(1-3):139 – 152.

Meyer, J. P. and Edwards, M. S. (1978). Survey of industrial coal conversion equipment capabilities: High temperature, high-pressure gas purification. Technical Report ORNL/TM-6072, Oak Ridge Nat. Lab.

Miller, R. S. and Bellan, J. (1999). Direct numerical simulation of a confined three-dimensional gas mixing layer with one evaporating hydrocarbon-droplet-laden stream. *Journal of Fluid Mechanics*, 384:293–338.

Monin, A. S. and Yaglom, A. M. (1975). *Statistical Fluid Mechanics II*. MIT Press.

Niera, A. M. and Payatakes, A. C. (1978). Collocation solution of creeping newtonian flow through periodically constricted tubes with piecewise continous wall profile. *A.I.Ch.E.J.*, 24(1):43.

Nora, O. . J. B. (2000). A priori subgrid analysis of temporal mixing layers with evaporating droplets. *Physics of Fluids*, 12(6):1573–1591.

Okong'o, N. a. and Bellan, J. (2004). Consistent large-eddy simulation of a temporal mixing layer laden with evaporating drops. Part 1. Direct numerical simulation, formulation and a priori analysis. *Journal of Fluid Mechanics*, 499:1–47.

O'Melia, Charles R., A. M. (1985). Particles, Pretreatment, and Performance in Water Filtraton. *Journal of Environmental Engineering*, 111(6):874–890.

Oran, E. S., Oh, C. K., and Cybyk, B. Z. (1998). Direct simulation Monte Carlo: Recent advances and applications. *Annu. Rev. Fluid Mech.*, 30:403–441.

O'Rourke, P. J. (1981). *Collective Drop Effects on Vaporizing Liquid Sprays*. PhD thesis, Princeton University.

O'Rourke, P. J., Zhao, P. P., and Snider, D. (2009). A model for collisional exchange in gas/liquid/solid fluidized beds. *Chemical Engineering Science*, 64(8):1784–1797.

Pai, M. G. and Subramaniam, S. (2006). Modeling interphase turbulent kinetic energy transfer in lagrangian-eulerian spray computations. *Atomization and Sprays*, 16(7):807–826.

Pai, M. G. and Subramaniam, S. (2007). Modeling droplet dispersion and interphase turbulent kinetic energy transfer using a new dual-timescale langevin model. *International Journal of Multiphase Flow*, 33(3):252–281.

Pai, M. G. and Subramaniam, S. (2009). A comprehensive probability density function formalism for multiphase flows. *J. Fluid Mech.*, 628:181–228.

Pai, M. G. and Subramaniam, S. (2012). Two-way coupled stochastic model for dispersion of inertial particles in turbulence. *J. Fluid Mech.*, 700:29–62.

Panchev, S. (1971). *Random functions and turbulence.* Pergamon Press, New York.

Passalacqua, A., Fox, R., Garg, R., and Subramaniam, S. (2010). A fully coupled quadrature-based moment method for dilute to moderately dilute fluid-particle flows. *Chemical Engineering Science*, 65(7):2267–2283.

Passalacqua, A., Galvin, J., Vedula, P., Hrenya, C. M., and Fox, R. O. (2011). A quadrature-based kinetic model for dilute non-isothermal granular flows. *Communications in Computational Physics*, 10:216–252.

Payatakes, A. C., Tien, C., and Turian, R. M. (1973). A new model for granular porous media. *A.I.Ch.E.J.*, 19(1):58.

Pendse, H. and Tien, C. (1982). General Correlation of the Initial Collection Efficiency of Granular Filter Beds. *AIChE Journal*, 28(4):677–686.

Petersen, E. E. (1958). Diffusuion in a pore of varying cross-section. *A.I.Ch.E.J.*, 4(3):343.

Pope, S. B. (1985). PDF Methods for Turbulent Reactive Flows. *Prog. Energy Combust. Science*, 11:119–192.

Pope, S. B. (2000). *Turbulent Flows*. Cambridge University Press, Port Chester, NY.

Quan, S., Schmidt, D. P., Hua, J., and Lou, J. (2009). A numerical study of the relaxation and breakup of an elongated drop in a viscous liquid. *Journal of Fluid Mechanics*, 640:235.

Rayapati, N. P., Panchagnula, M. V., Peddieson, J., Short, J., and Smith, S. (2011). Eulerian multiphase population balance model of atomizing, swirling flows. 3:19–44.

Reveillon, J. and Vervisch, L. (2005). Analysis of weakly turbulent dilute-spray flames and spray combustion regimes. *J. Fluid Mech.*, 537:317–347.

Ritzert, J. A., Brown, R. C., and Smeenk, J. (2004). Filtration Efficiency of a Moving Bed Granular Filter. *Proceedings of the Science in Thermal and Chemical Biomass.*

Schiller, L. and Naumann, A. Z. (1933). A Drag Coefficient Correlation. *Z. Ver. Deutsch Ing.*, pages 318–320.

Schlichting, H. (1968). *Boundary Layer Theory*. McGraw-Hill.

Schmidt, D. P., Dai, M., Wang, H., and Perot, J. B. (2002). Direct interface tracking of droplet deformation. *Atomization and Sprays*, 12(5–6):721–735.

Schmidt, D. P. and Rutland, C. J. (2000). A new droplet collision algorithm. *Journal of Computational Physics*, 164(1):62–80.

Song, C. and Park, H. (2006). Analytic Solutions for Filtration of Polydisperse Aerosols in Fibrous Filter. *Powder Technology*, 170(2):64–70.

Squires, K. D. and Eaton, J. K. (1991a). Lagrangian and Eulerian statistics obtained from direct numerical simulations of homogeneous turbulence. *Phys. Fluids*, 3(1):130–143.

Squires, K. D. and Eaton, J. K. (1991b). Measurements of particle dispersion obtained from direct numerical simulations of isotropic turbulence. *J. Fluid Mech.*, 226:1–35.

Squires, K. D. and Eaton, J. K. (1991c). Preferential concentration of particles by turbulence. *Phys. Fluids A*, 3:1169–1178.

Subramaniam, S. (2000a). Statistical Representation of a Spray as a Point Process. *Phys. Fluids*, 12(10):2413–2431.

Subramaniam, S. (2000b). Statistical representation of a spray as a point process. *Phys. Fluids*, 12(10):2413–2431.

Subramaniam, S. (2001a). Statistical Modeling of Sprays Using the Droplet Distribution Function. *Phys. Fluids*, 13(3):624–642.

Subramaniam, S. (2001b). Statistical modeling of sprays using the droplet distribution function. *Phys. Fluids*, 13(3):624–642.

Subramaniam, S. (2013). Lagrangian-Eulerian methods for multiphase flows. *Prog. Energy Combust. Science*, 39(2–3):215–245.

Sun, J., Battaglia, F., and Subramaniam, S. (2007). Hybrid Two-Fluid DEM Simulation of Gas-Solid Fluidized Beds. *Journal of Fluids Engineering*, 129(11):1394.

Sundaram, S. and Collins, L. R. (1997). Collision statistics in an isotropic particle–laden turbulent suspension. part i. direct numerical simulations. *J. Fluid Mech.*, 379:75–109.

Syamlal, M., Rogers, W., and O'Brien, T. J. (1993). Mfix documentation: Theory guide. Technical report, Technical Note, DOE/METC-94/1004, NTIS/DE94000087, National Technical Information Service, Springfield, VA.

Tenneti, S. (2013). *Momentum, energy and scalar transport in polydisperse gas-solid flows using particle–resolved direct numerical simulations.* PhD thesis, Iowa state university.

Tenneti, S., Garg, R., Hrenya, C. M., Fox, R. O., and Subramaniam, S. (2010). Direct Numerical Simulation of Gas-Solid Suspensions at Moderate Reynolds Number: Quantifying the Coupling between Hydrodynamic Forces and Particle Velocity Fluctuations. *Powder Technology*, 203:57–69.

Tenneti, S., Garg, R., and Subramaniam, S. (2011). Drag Law for Monodisperse Gas-Solid Systems using Particle-Resolved Direct Numerical Simulation of Flow Past Fixed Assemblies of Spheres. *Intl. J. Multiphase Flow*, 37(9):1072–1092.

Tenneti, S., Garg, R., and Subramaniam, S. (2013a). Quantification of gas–phase velocity fluctuations in statistically homogeneous gas–solid flow using particle–resolved direct numerical simulation. *A.I.Ch.E.J.* (In review).

Tenneti, S. and Subramaniam, S. (2013). Particle-resolved direct numerical simulation for gas-solid flow model development (in preparation). *Annu. Rev. Fluid Mech.*

Tenneti, S., Sun, B., Garg, R., and Subramaniam, S. (2013b). Role of heating in dense gas-solid flow as revealed by particle-resolved direct numerical simulation. *Intl. J. Heat Mass Transfer*, 58(1–2):471–479.

Thambimuthu, K. V. (1980). *Gas Filtration in Fixed and Fluidized Beds.* PhD thesis, University of Cambridge, Cambridge.

Tien, C. and Ramarao, B. (2007). *Granular Filtration of Aerosols and Hydrosols*. Butterworths Series in Chemical Engineering. Elsevier.

Uhlmann, M. (2005). An immersed boundary method with direct forcing for the simulation of particulate flows. *Journal of Computational Physics*, 209(2):448–476.

Van der Hoef, M. A., Beetstra, R., and Kuipers, J. A. M. (2005). Lattice-Boltzmann simulations of low-Reynolds-number flow past mono- and bidisperse arrays of sphere: results for the permeability and drag force. *J. Fluid Mech.*, 528:233–254.

Wall, S., John, W., Wang, H.-C., and Goren, S. L. (1990). Measurements of Kinetic Energy Loss for Particles Impacting Surfaces. *Aerosol Science and Technology*, 12(4):926–946.

Wang, H. C. and John, W. (1988). *In Particles on Surface 1: Detection, Adhesion and Removal*. Plenum Press, New York, edited by k. l. mittal edition.

Wang, H. G., Yang, W. Q., Senior, P., Raghavan, R. S., and Duncan, S. R. (2008). Investigation of batch fluidized-bed drying by mathematical modeling, cfd simulation and ect measurement. *A.I.Ch.E.J.*, 54:427–444.

Wang, L.-P., Rosa, B., Gao, H., He, G., and Jin, G. (2009). Turbulent collision of inertial particles: Point-particle based, hybrid simulations and beyond. *International Journal of Multiphase Flow*, 35(9):854–867.

Ward, A. S. (1981). Techniques for the removal of particulates from hot gas products of fluidized bed coal combustion. *Filtration Separation*, pages 542–550.

Williams, F. A. (1958). Spray Combustion and Atomization. *Phys. Fluids*, 1(6):541–545.

Wu, X. and Tien, C. (1995). Polydispersed Aerosol Filtration in Granular Media. *Separations Technology*, 5(2):63–75.

Xu, Y. and Subramaniam, S. (2006). A multiscale model for dilute turbulent gas–particle flows based on the equilibration of energy concept. *Phys. Fluids*, 18:033301(1–17).

Xu, Y. and Subramaniam, S. (2010). Effect of Particle Clusters on Carrier Flow Turbulence: A Direct Numerical Simulation Study. *Flow, Turbulence and Combustion*, 85(3-4):735–761.

Yoshida, H. and Tien, C. (1985). A New Correlation of the Initial Collection Efficiency of Granular Aerosol Filtration. *AIChE Journal*, 31(10):1752–1754.

Zhang, Z. and Prosperetti, A. (2005). A second-order method for three-dimensional particle simulation. *Journal of Computational Physics*, 210(1):292–324.